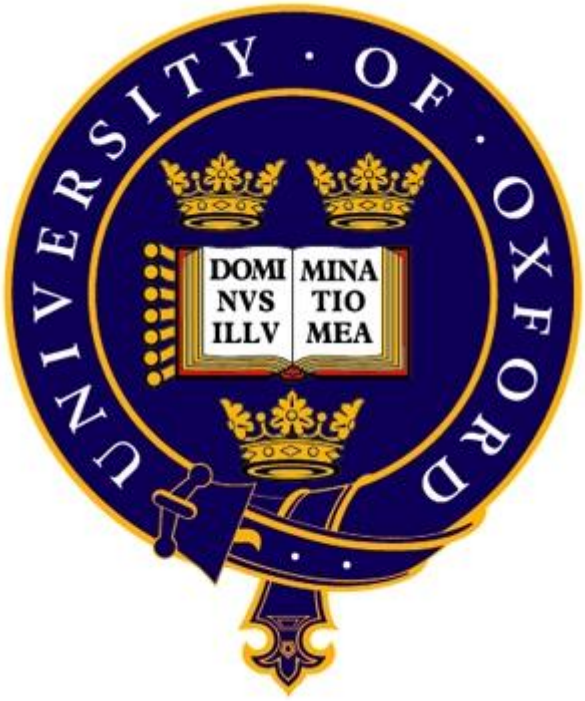
# Solvodynamic Printed Silver Nanowire Composite Films for Pressure Sensing Applications




**Wing Chung Liu**

**Oriel College**

**Trinity 2019**

A thesis submitted in fulfillment of requirement for the degree of
DPhil in Materials at the University of Oxford

## Abstract

This thesis examines some of the current issues with the use of non-contact printing techniques for fabricating conductive structures for applications in flexible pressure sensors.

Firstly, the concept of solvodynamic printing was introduced as a method to improve printing resolution using solvent-solvent interactions. By including an additional carrier solvent into the ink delivery system, both the footprint of the ejected ink and the degree of ink spreading on the substrate could be reduced. The proof-of-concept of this technique was demonstrated by printing lines of silver nanoparticles on polyethylene naphthalate substrates. Silver nanoparticle tracks with widths of 35.2 ± 7.0 μm were achieved using a 300 μm nozzle. This is equivalent to 11.7 ± 2.3 % of the nozzle diameter. The result shows great potential in solvodynamic printing as not many modern printing techniques can achieve such nozzle to feature size ratios.

Next, the use of ligand exchange on silver nanowires to formulate a post-treatment free ink which can produce highly conductive printed silver nanowire structures was explored. The use of rigid bidentate linking ligands was studied. Among the ligands used, fumaric acid was shown to be the most effective in improving the film conductivity, reducing the sheet resistance by 70 % of a control sample from 26.5 Ω/□ to 7.66 Ω/□. The decrease in sheet resistance was attributed to the decrease in junction resistance of the nanowire film.

Lastly, a simple fabrication method was used to make piezoresistive composite films consisting of silver nanowires embedded in an ethylene-co-vinyl acetate matrix. The performances of the pressure sensor using compressive and tensile strains were compared. The properties of the pressure sensor were highly tunable based on the composition and design of the film. Overall, the films showed a low detection limit (1.47 ± 0.13 Pa), fast response time (11-22 ± 2.9 ms) and high sensitivity (67.3 ± 5.9 $kPa^{-1}$). We further showed the successful application of the film as a pulse monitoring device.

## Acknowledgements

I would like to thank Prof. Andrew Watt for his supervision and guidance throughout my DPhil and the freedom he has given me to pursue interesting research topics. I also appreciate the opportunity he has given me to become involved in the commercial side of things, dealing with patents and meeting with potential commercial partners. Through these experiences, I have learnt a lot outside of academic research and they will indubitably be useful for my future career. I would also like to thank Professor Hazel Assender for her feedback on my research during group meetings as well as helping during my transfer of status.

Next, I would like to thank my colleagues in the group. To the senior members, thank you for being welcoming and helpful when I first joint the group and maintaining a conducive environment for research and laboratory work. I would like to thank Assia, Nanlin and Zhanet for their encouragement and advice along the way. Also, special mentions to Yujiro for being my occasional chemistry consultant and also a great friend and housemate. To the newer students, I would like to thank Daniel for always making a fun environment in the group.

I would also like to acknowledge my friends outside of research for being good company along the DPhil journey. Special thanks to people of OW! And OUMSSA plays frisbee for the fun and de-stressing ultimate frisbee sessions week after week. I am also very grateful to friends of BS brothers for hanging out and being awesome company.

Lastly, I would like to acknowledge my loved ones. To my parents, thank you for giving me the freedom and support to pursue a PhD. To my girlfriend Vanessa, thank you for encouraging me to make the decision to do a PhD in the first place and for your support during these four years.

## Statement of Originality and Research Ethics

This thesis is an account of work carried out by the author in the Department of Materials, the University of Oxford under the supervision of Professor Andrew Watt. Any work of others that has been utilized, directly or indirectly, is duly acknowledged in the text, and a list of references is presented at the end of each chapter. No part of this thesis has been submitted towards the completion of another degree at the University of Oxford or elsewhere. Parts of the thesis have been submitted to or published in the following scientific journals or conference presentations:

Journal articles:

Liu, W.C. & Watt, A.A.R. Solvodynamic Printing as A High Resolution Printing Method. *Sci. Rep.* 9 (2019).

Conference Presentations:

Liu, W.C. & Watt, A.A.R., Solvodynamic Printed Silver Tracks. MRS Spring Meeting 2018, Phoenix, Arizona, United States. (Oral presentation)

Part of the research work presented in this thesis involved human participants. The research work was done in accordance to the guidelines set out by the Central University Research Ethics Committee. The proposed research study received human research ethics approval from the Medical Sciences Interdivisional Research Ethics Committee, Ethics Approval Reference: R70886/RE001.

## Table of Contents

**Abstract** ---------- **i**
**Acknowledgements** ---------- **ii**
**Statement of Originality and Research Ethics**---------- **iii**
**Table of Contents** ---------- **iv**
**List of Tables** ---------- **viii**
**List of Figures** ---------- **x**
**List of Abbreviations** ---------- **xvi**
**List of Symbols** ---------- **xvii**

**Chapter 1 – Introduction** ----------**1**
1.1 Printed and Flexible Electronics ----------1
1.2 Printing Conductive Structures ---------- 3
1.3 Stretchable Electronics ----------4
1.4 Aim of thesis ---------- 5
1.5 Structure of thesis ---------- 6
1.6 References ---------- 7

**Chapter 2 - Literature Review** ---------- **9**
2.1 Achieving High Resolution in Non-Contact Printing Technologies -----9
2.1.1 Controlling Ink Footprint ----------10
2.1.1.1 Electrohydrodynamic Printing ---------- 10
2.1.1.2 Aerosol Jet Printing ----------12
2.1.2 Ink Wettability on Substrate ---------- 14
2.1.2.1 Controlling Contact Angle ----------15
2.1.2.2 Pre-patterning Substrates ----------15
2.2 Electrical Properties of Printed Silver Nanowire Films ---------- 17
2.2.1 Percolation Theory ---------- 17
2.2.2 Role of Junction Resistance in Silver Nanowire Films -------- 20
2.2.3 Methods of Reducing Junction Resistance ----------21
2.2.3.1 Post-Treatments ---------- 21
2.2.3.2 Chemical Treatments ---------- 23

2.2.3.3 Treatment Free Conductive Inks ---------- 24
2.3 3D Conduction Composite Films as Pressure Sensor Materials --------- 26
2.3.1 Transduction Mechanisms ---------- 27
2.3.2 Piezoresistive Sensors ---------- 29
2.3.3 Achieving High Sensitivity ---------- 29
2.3.3.1 Microstructured Surface ----------30
2.3.3.2 Conductive Sponges ---------- 32
2.3.4 Silver Nanowire Composite Films as Pressure Sensors --------33
2.4 Conclusion and Prospects ---------- 34
2.5 References ---------- 37

**Chapter 3 - Solvodynamic Printing as A High-Resolution Printing Method ---49**
3.1 Introduction ---------- 49
3.2 Solvodynamic Printing ----------50
3.2.1 Printing Principles ----------50
3.2.2 Controlling Flow Behaviour ---------- 51
3.2.3 Ink Wetting Behaviour ---------- 54
3.3 Materials and Methods ---------- 56
3.3.1 Materials ----------56
3.3.2 Solvodynamic Printer Set-up ---------- 57
3.3.3 Summary of Experimental Conditions and Parameters -------- 59
3.3.4 Characterization Methods---------- 62
3.4 Results and Discussion ---------- 67
3.4.1 Mathematical Model---------- 68
3.4.2 Ink Stream Wdith---------- 69
3.4.2.1 Control of Ink Flow Rates using Carrier Solvent ----71
3.4.2.2 Effect of Carrier Solvent on Ink Contact Angle ----- 75
3.4.2.3 Effect of Carrier Solvent on Printed Line Widths --- 77
3.4.3 Ink Surface Tension ---------- 81
3.4.4 Substrate Surface Energy ----------86
3.4.5 Overall Ink Loading ----------88
3.5 Conclusion ----------90
3.6 References ---------- 92

**Chapter 4 - Ligand Exchanged Silver Nanowire for Conductivity Improvement** ---------- **95**
4.1 Introduction ---------- 95
4.1.1 Choice of Ligands ---------- 97
4.1.2 Ligand Exchange Reaction ---------- 98
4.2 Materials and Methods ---------- 99
4.2.1 Materials ---------- 99
4.2.2 Ligand Exchange of Silver Nanowire ---------- 100
4.2.3 Fabrication of Silver Nanowire Film ---------- 101
4.2.4 Characterization ---------- 103
4.2.4.1 Structure of Ligand Shell on Silver Nanowires ------ 103
4.2.4.2 Macroscopic Properties of Silver Nanowire Films--- 105
4.3 Results and Discussion ---------- 106
4.3.1 Fourier Transform Infrared Spectroscopy ---------- 106
4.3.2 Thermogravimetric Analysis ---------- 110
4.3.3 Zeta Potential Measurements ---------- 113
4.3.4 Electrical Properties of Ligand Exchanged Nanowire Films -- 116
4.3.5 Film Morphology ---------- 120
4.3.6 Sintering Temperature ---------- 123
4.4 Conclusion ---------- 125
4.5 References ---------- 126

**Chapter 5 - Solvodynamic Printed Silver Nanowire-Ethylene-co-Vinyl Acetate Composite Films as Highly Sensitive Piezoresistive Pressure Sensors** ---------- **129**
5.1 Introduction ---------- 129
5.1.1 Pressure Sensor Schematics ---------- 131
5.2 Materials and Methods ---------- 132
5.2.1 Materials ---------- 132
5.2.2 Fabrication of Composite Film ---------- 133
5.2.3 Characterization of Film Properties ---------- 135
5.2.4 Electromechanical Measurements of Pressure Sensor --------- 135
5.3 Results and Discussion ---------- 140
5.3.1 General AgNW-EVA Film Properties ---------- 140

5.3.2 Electrical Properties of Composite Films ---------- 141
5.3.3 Electromechanical Response to Pressure ---------- 144
5.3.3.1 Compression Mode Pressure Sensor ---------- 144
5.3.3.2 Tensile Mode Pressure Sensor ---------- 148
5.3.3.3 Patterned Pressure Sensors ---------- 152
5.3.4 Application in Pulse Sensing ---------- 155
5.4 Conclusion ---------- 156
5.5 References ---------- 158

**Chapter 6 – Conclusion and Future Work** ---------- **161**
6.1 Conclusion of Thesis Findings ---------- 161
6.2 Future Work ---------- 164
6.3 References ---------- 167

# List of Tables


| Table | Caption | Page |
|---|---|---|
| 2-1 | List of recently reported high performance flexible pressure sensors | 28 |
| 3-1 | Summary of properties of inks used | 56 |
| 3-2 | Summary of experimental parameters used | 62 |
| 3-3 | Observed ink stream at different nominal relative flow rates used | 70 |
| 3-4 | Measured ink flow rates at various nominal $\tilde{Q}$ with different inks | 72 |
| 3-5 | Measured hexane flow rates at various nominal $\tilde{Q}$ with different inks | 72 |
| 3-6 | Actual relative flow rates at various nominal $\tilde{Q}$ with different inks | 72 |
| 3-7 | Estimated hexane flow velocities at various nominal $\tilde{Q}$ with different inks | 74 |
| 3-8 | Estimated ink flow velocities at various nominal $\tilde{Q}$ with different inks | 74 |
| 3-9 | Contact angle of different ink droplets deposited under different flow rate conditions onto a PEN substrate ozone treated for 3.5 mins | 76 |
| 3-10 | Contact angle of ink droplets with different EG content deposited on a PEN substrate ozone treated for 3.5 mins while submerged in a large volume of hexane | 76 |
| 3-11 | Measured contact angle and calculated surface tension of several inks deposited on a PEN substrate ozone treated for 2 mins | 82 |
| 3-12 | Comparison of measured contact angles of several inks deposited on a PEN substrate ozone treated for 3.5 mins while being immersed in hexane and the corresponding observed printing parameter *k* | 84 |
| 3-13 | Measured contact angle of water droplets on substrates with varying ozone treatment time and their calculated surface energy | 87 |
| 4-1 | Amount of ligands added per ml of AgNWs suspension diluted to 1 mg/ml for ligand exchange | 101 |
| 4-2 | Properties of aqueous silver nanowire ink used to fabricate films | 102 |
| 4-3 | pKas of the various acids and amine ligands used in the ligand exchange | 105 |

| | | |
|---|---|---|
| 4-4 | Peak positions of defining functional groups in acid ligands and their corresponding LE-AgNWs | 109 |
| 4-5 | Peak positions of defining functional groups in amine ligands and their corresponding LE-AgNWs | 109 |
| 4-6 | Decomposition temperatures, molar ratios of new ligands and PVP to silver in the different LE-AgNWs | 111 |
| 4-7 | Parameters used in the estimation of tunneling current density in each sample | 119 |
| 4-8 | Comparison of ligand decomposition and critical sintering temperatures for different LE-AgNW samples | 124 |
| 5-1 | Volume of EVA solution required for making films with different EVA thicknesses | 134 |
| 5-2 | Pressure applied on AgNW composite film by stacking one-pound coins on a glass slide for compressive mode pressure sensing | 137 |
| 5-3 | Pressure applied on AgNW composite film by attaching different number of neodynium magnets on plastic ruler at various distance from the fulcrum for tensile mode pressure sensing | 138 |

# List of Figures


| Figure | Caption | Page |
|---|---|---|
| 1-1 | Schematic of (a) photolithography and (b) non-contact printing as patterning techniques. | 2 |
| 2-1 | Schematics of (a) inkjet printing, (b) electrohydrodynamic printing and (c) aerosol jet printing. | 10 |
| 2-2 | Schematic diagram showing the determination of contact angle, $\theta$. $\sigma_{si}$, $\sigma_{ia}$, $\sigma_{sa}$ are the interfacial tensions between substrate-ink, ink-air and substrate-air respectively. | 14 |
| 2-3 | Some ligands used to improve charge transport between metallic nanoparticle films. | 24 |
| 2-4 | Schematic diagrams of 3 different types of pressure transduction mechanisms: (a) piezoresistivity, (b) capacitance and (c) piezoelectricity. Image taken from reference. | 27 |
| 2-5 | Schematic of different microstructures and their behaviour under applied pressure. | 30 |
| 3-1 | Schematic of solvodynamic printing with relevant parameters. The carrier solvent is a solvent immiscible with the printing ink that is meant to improve printing resolution by reducing the size of the ink ejected from the printer and alter the wetting behaviour of the ink on the substrate. *d* denotes the width of the ink stream within the microfluidic channel and *w* denotes the final width of the dried printed line. | 50 |
| 3-2 | Different flow regimes for two immiscible fluids: (a) Droplet formation and (b) Parallel flow. The arrows indicate the direction of the fluid flow. | 52 |
| 3-3 | Micrograph of fluid carrier solvent (clear) and ink (coloured) flow within the microfluidic chip at different nominal relative flow rates. Flows for nominal relative flow rates of (a) 1, (b) 3, (c) 5 and (d) 8. The scale bar represents 200 μm. The arrows indicate the direction of fluid flow. | 53 |
| 3-4 | (**a**) Schematics of how changing wetting medium leads to improvements in resolution. The cross section geometry of the ink will be used to set up a model in the later section. $\theta_i$ and $\theta^*$ represent the equilibrium contact angle of the ink droplet in air and in carrier solvent respectively. $\sigma_{ia}$, $\sigma_{si}$, $\sigma_{sa}$, $\sigma_{ic}$ | 55 |

| | | |
|---|---|---|
| | and $\sigma_{sc}$ are the interfacial tensions between ink-air, substrate-ink, substrate-air, ink-carrier solvent and substrate-carrier solvent respectively. (**b**) Demonstrating the actual change in wetting behaviour of an aqueous silver nanoparticle ink droplet in air and (**c**) in hexane carrier solvent. Scale bar represent 0.1 mm. | |
| 3-5 | (**a**) The solvodynamic printing set up used in this study. (**b**) Schematics of the solvodynamic printier, consisting of two syringe pumps, microfluidic chip and translational stage. (**c**) A close up image of the microfluidic chip used. The junction on the furthest right is the Y-shaped junction used. The inlets are at the top and the outlet is at the bottom of the chip. (d) Schematics and dimensions of the Y-junction microfluidic channel within the chip. (e) Close up image of the nozzle and translational stage. (f) Schematics of the nozzle and translational stage position and stage movement during printing. | 58 |
| 3-6 | Schematic of contact angle measurement set-up consisting of a USB microscope clamped on a stand with the substrate placed on a goniometer stage | 63 |
| 3-7 | Micrographs of ink flow in microfluidic channels using (a) high surface tension ink with 0 wt% EG and (b) low surface tension ink with 20 wt% EG (right) at a nominal relative flow rate of 3 with nominal ink flow rate of 50 µl/hr. Inset diagram are the schematics of the cross-sectional shape of ink stream for the respective micrographs. | 71 |
| 3-8 | A micrograph of the side view of an ink droplet surrounded by hexane as carrier solvent. The ink had 20% EG and was deposited with $\tilde{Q} = 3$ on a PEN substrate which was ozone treated for 3.5 mins. | 76 |
| 3-9 | Micrographs of solvodynamic printed lines with widths denoted by *w*. They were printed while varying the nominal relative ink flow rate, $\tilde{Q}$. Lines were printed with $\tilde{Q}$ = (**a**) 0, (**b**) 1, (**c**) 2, (**d**) 5 and (**e**) 8. The ink flow rate was fixed at 50 µl/hr. The ink used consisted of silver nanoparticles with concentration of 6 mg/ml dispersed in water with 15 wt% of ethylene glycol. The substrate used was polyethylene naphthalate which was ozone-treated for 3.5 min. Substrate velocity was set at 20 $mms^{-1}$. Scale bars represent 200 µm. (**f**) and (**g**) are cross sectional profile of a solvodynamically printed line and a line printed without carrier solvent respectively. | 78 |

| | | |
|---|---|---|
| 3-10 | Experimental and modelled variation in printed line width (*w*) and ink stream width (*d*) with the change in ink flow rate for 0%EG and 15%EG inks. | 80 |
| 3-11 | Micrographs of solvodynamic printed lines using inks with different surface tension by varying the amount of ethylene glycol mixed into the ink: (a) 0 wt%, (b) 5 wt%, (c) 10 wt%, (d) 15 wt%, (e) 20 wt%. The ink and carrier solvent flow rates were fixed at 50 µl/hr and 100 µl/hr respectively, inks consisted of silver nanoparticles with concentration of 6 mg/ml. The substrate used was polyethylene naphthalate which was ozone-treated for 3 min. Substrate velocity was set at 20 mms-1. Scale bars represent 200 µm. (f) Variation in polyethylene naphthtalate substrate surface energy with the change in duration under ozone plasma treatment. (g) Experimental and modelled variation in printed line width (w) with the change in ink surface tension. | 83 |
| 3-12 | Low Magnification micrographs of printed lines using (**a**) 0 wt% EG ink and (**b**) 20 wt% EG ink. The scale bar represents 500 µm. | 84 |
| 3-13 | Micrographs of solvodynamic printed lines using polyethylene naphthalate substrates treated by ozone plasma for different times: (**a**) 2 min, (**b**) 2.5 min, (**c**) 3.5 min and (**d**) 4.5 min. The ink and carrier solvent flow rates were fixed at 50 µl/hr and 100 µl/hr respectively, ink consisted of silver nanoparticles with concentration of 6 mg/ml dispersed in water with 15 wt% of ethylene glycol. Substrate velocity was set at 20 $mms^{-1}$. Scale bars represent 200 µm. (**e**) Variation in substrate surface energy with the change in ozone plasma treatment time. (**f**) Variation in printed line width (*w*) of 2 sets of printed lines with change in substrate surface energy. | 88 |
| 3-14 | (a) Variation in printed line widths with substrate surface energy for 3 sets of lines printed with different nominal ink flow rate ($\tilde{q}_i$) to substrate velocity ($v_s$) ratios. Values of $\tilde{q}_i$ and $v_s$ are measured in µl/hr and $mms^{-1}$ respectively. The nominal carrier solvent to ink flow rate was fixed at 2 and the ink used with 15 wt% EG and 6 mg/ml silver nanoparticles. (b) Optical images of 10 printed lines at the optimized parameters. Scale bar represents 100 µm. (c) A SEM image of one of the printed lines. (d) The distribution of the line widths taken at points every 40 µm along the lengths of the 10 printed lines for 50 points per line. | 90 |

| | | |
|---|---|---|
| 4-1 | Schematics of different ways bidentate ligands can bind onto a nanowire surface: (i) both binding groups on ligand are bound to the same nanowire due to bond rotation in single bonds. (ii) unsaturated bonds in molecule allow ligand to remain rigid. | 97 |
| 4-2 | The different acid and amine ligands used in this study. A mixture of saturated (flexible), unsaturated (rigid), monodentate and bidentate ligands are used. | 98 |
| 4-3 | Schematic diagram showing the potential mechanism for improvement in nanowire contact after ligand exchange. | 99 |
| 4-4 | (a) Schematic of the programmed stage movement for printing AgNW film on a glass substrate. The arrow represents the movement of the printer nozzle relative to the substrate achieved by the movement of the X-Y translational stage. (b) Comparison between a drop casted (left) and solvodynamic printed (right) silver nanowire film. | 102 |
| 4-5 | FTIR spectra of: (a) PVP and control AgNWs, (b) acid ligands and their corresponding LE-AgNWs. In each pair of spectra, the one below is the spectrum of the pure ligand and the one on top is the spectra of the LE-AgNWs. (c) Corresponding spectra of amine ligands and their LE-AgNWs. Dotted lines show regions containing characteristic peaks corresponding to certain bonds present in the sample. | 107 |
| 4-6 | Normalised TGA curves for (a) acid ligand-exchanged AgNWs and (b) amine ligand-exchanged AgNWs. | 110 |
| 4-7 | Variation of zeta potential of AgNWs when subjected to different degrees of ligand exchange using (a) acid ligands and (b) amine ligands. | 113 |
| 4-8 | Simplified schematics of arrangement of new ligands on nanowires without consideration of PVP for: (a) monodentate ligands, (b) bidentate flexible ligands and (c) bidentate rigid ligands. | 115 |
| 4-9 | Variation in sheet resistances of AgNW films with zeta potential using different types of ligands for (a) acid ligands and (b) amine ligands. (c) Plot of calculated log of tunneling current density, *J* at the metal-ligand-metal junction for the different ligands. | 117 |
| 4-10 | (a) and (b) High and low magnification SEM images of control AgNWs. (c) and (d) High and low magnification SEM images of PDA LE-AgNWs. (e) and (f) High and low magnification SEM images of fumaric acid LE- | 121 |

| | | |
|---|---|---|
| | AgNWs. Scale bars are equivalent to 200 nm on high magnification images and 10 μm on low magnification images. | |
| 4-11 | Variation in sheet resistance of AgNW films with (a) acid and (b) amine ligands when different sintering temperatures were used. Sintering times were fixed at 20 mins. | 123 |
| 5-1 | Schematics of: (a) compressive pressure sensing mode, (b) tensile pressure sensing mode. | 132 |
| 5-2 | Design of the patterned films. $t_{grid}$ represents the grid line width. Grids with $t_{grid}$ of 0.16 mm, 0.2 mm and 0.3 mm were printed. | 134 |
| 5-3 | Schematics of pressure sensor setup for (a) compressive mode and (b) tensile mode. | 136 |
| 5-4 | (a) SEM image of silver nanowires (AgNWs) used in this study. The scale bar represents 10 μm. (b) Photograph of an AgNW-EVA composite film. (c) SEM image of the surface morphology of the conductive side of the film. The scale bar represents 1 μm. (d) SEM image of the cross section of the composite film. The scale bar represents 100 μm. The inset is a high magnification image of the conductive layer. The scale bar represents 5 μm. | 141 |
| 5-5 | (a) Sheet resistance, (b) thickness of the conductive layer and (c) conductivity of the AgNW-EVA composite films with different AgNW loading. | 143 |
| 5-6 | (a) The electrical response of an AgNW-EVA film fabricated with AgNW concentration of 0.15 mg/mm$^2$ when a pressure of 33.8 Pa was applied repeatedly. (b) The variation of change in resistance of the films with applied pressure for several films made with different AgNW concentrations. (c) The variation of pressure sensing sensitivities of films with different AgNW loading at different applied pressures. (d) The response time of the composite film during loading (left) and unloading (right). (e) Electromechanical response of AgNW-EVA composite films with varying EVA thicknesses. | 145 |
| 5-7 | (a) The electrical response of an AgNW-EVA film fabricated with AgNW concentration of 0.2 mg/mm$^2$ when a pressure of 62.5 Pa was applied repeatedly. (b) The variation of change in resistance of the films with applied pressure for several films made with different AgNW concentrations. (c) The electrical response of the different AgNW-EVA composite films with different nanowire concentrations as strain gauges under tensile stress. The | 149 |

lines represent modelled results based on the power law and the circles are the experimentally observed results. (d) The response time of the composite film during loading (left) and unloading (right). (e) The electrical response of the AgNW-EVA film with varying EVA thicknesses with AgNW concentration fixed at 0.175 mg/cm$^2$. (f) The variation in pressure sensing sensitivity when the AgNW concentration and EVA film thickness is varied. Each sample is labelled by its AgNW loading followed by EVA thickness.

5-8 Photographs of grid-patterned AgNW-EVA composite films. The grid line widths are approximately: (a) 1.6 mm, (b) 2.0 mm and (c) 3.0 mm. The AgNW concentration of the films are fixed at 0.15 mg/cm$^2$ and the EVA thickness is 35 μm. Scale bar represents 5 mm. (d) The electromechanical response of patterned films with different grid line widths when a pressure of 33.1 Pa is applied on the films. (e) The variation of change in resistance of the films with applied pressure for several patterned films made with different grid line widths. (f) The variation of pressure sensing sensitivities of films with different AgNW loading at different applied pressures. 154

5-9 (a) Photograph of the setup of pulse monitoring using the AgNW-EVA film. (b) Measured response of carotid pulse. 156

## List of Abbreviations

| | |
|---|---|
| Ag | Silver |
| AgNP | Silver nanoparticle |
| AgNW | Silver nanowire |
| AJP | Aerosol jet printing |
| CNT | Carbon nanotube |
| DAH | 1,6-Diaminohexane |
| EG | Ethylene glycol |
| EHD | Electrohydrodynamic |
| EVA | Ethylene-vinyl acetate |
| FR | Focusing ratio |
| FTIR | Fourier transform infrared spectroscopy |
| ITO | Indium-doped tin oxide |
| LE-AgNW | Ligand exchanged-silver nanowire |
| LUMO | Lowest unoccupied molecular orbital |
| MOPAC | Molecular orbital package |
| PDA | p-Phenylenediamine |
| PDMS | Polydimethylsiloxane |
| PEDOT:PSS | Poly(3,4-ethylenedioxythiophene) polystyrene sulfonate |
| PEN | Polyethylene naphthalate |
| PTEBS | Poly[2-(3-thienyl)-ethyl- oxy-4-butylsulfonate] |
| PU | Polyurethane |
| PVP | Polyvinylpyrrolidone |
| TGA | Thermogravimetric analysis |
| VA | Vinyl acetate |

## List of Symbols

| | |
|---|---|
| $Ca$ | Capillary number |
| $C_d$ | Discharge coefficient |
| $d$ | Ink stream width |
| $E_b$ | Tunneling energy barrier |
| $E_f$ | Fermi energy |
| $f$ | Instability factor |
| $k$ | Model fitting parameter |
| $L$ | Ligand to silver molar ratio |
| $N$ | Filler density |
| $N_o$ | Critical filler density |
| $Q$ | Relative carrier solvent to ink flow rate |
| $\tilde{Q}$ | Nominal relative carrier solvent to ink flow rate |
| $q_i$ | Ink volumetric flow rate |
| $\tilde{q}_i$ | Nominal ink flow rate |
| $q_c$ | Carrier solvent volumetric flow rate |
| $\tilde{q}_c$ | Nominal carrier solvent volumetric flow rate |
| $Re$ | Reynold number |
| $t$ | Critical exponent |
| $t_{grid}$ | Grid width thickness for patterned AgNW-EVA composite films |
| $w$ | Printed line width |
| $We$ | Weber number |
| $v_s$ | Substrate velocity |
| $\beta_{max}$ | Maximum spreading ratio |
| $\zeta$ | Zeta potential |
| $\theta$ | Contact angle |
| $\theta_i$ | Equilibrium contact angle of liquid under air |
| $\theta^*$ | Equilibrium contact angle of liquid under carrier solvent |
| $\sigma$ | Conductivity |
| $\sigma_{eff}$ | Effective surface charge density |
| $\sigma_o$ | Pre-exponential factor |

| | |
|---|---|
| $\phi$ | Filler volume fraction |
| $\phi_c$ | Critical filler volume fraction |

# Chapter 1 – Introduction

## 1.1 Printed and Flexible Electronics

Electronics are a ubiquitous part of our modern society and have integrated strongly with many aspects of everyday life. In particular, the past decades have seen the rise in the field of printed and flexible electronics. The printed electronics market is projected to reach $73 billion by 2027.[1] Unlike traditional electronics which are based on integrated circuits built on rigid silicon wafers, printed and flexible electronics involve fabricating devices on a wide range of flexible substrates and can maintain functionality even under a wide range of deformations such as folding and twisting.[2] This gives rise to devices which are lightweight, portable and mechanically stable.[3]

From a commercial point of view, flexible electronics also have a substantial cost advantage. Traditional electronics are largely fabricated by nanolithography techniques as shown in Figure 1-1a. These processes are highly complex with a mixture of additive and subtractive steps, with some steps using high vacuum processes.[4] On the other hand, flexible electronic devices are typically made using printing processes. These processes are simple and can usually be done at low temperatures and atmospheric pressure. Therefore, flexible electronics are much cheaper to produce.[5] In addition, they are compatible with high throughput roll-to-roll processing which increases the throughput of the processes.[6] These printing processes can be categorized into contact and non-contact printing techniques. Contact printing are techniques like gravure and screen printing which use a template pressed onto the substrate to form the printed pattern.[7,8] Conversely, non-contact techniques such as inkjet and aerosol printing do not require a predefined mask and are based on ejecting ink through a nozzle at desired locations on a substrate to form a pattern as shown

in Figure 1-1b.[9,10] The focus of this thesis will be on non-contact printing as it has the advantages of performing on-demand patterning, printing on non-planar surfaces, minimizing substrate damage and forming multilayer devices.[11,12]

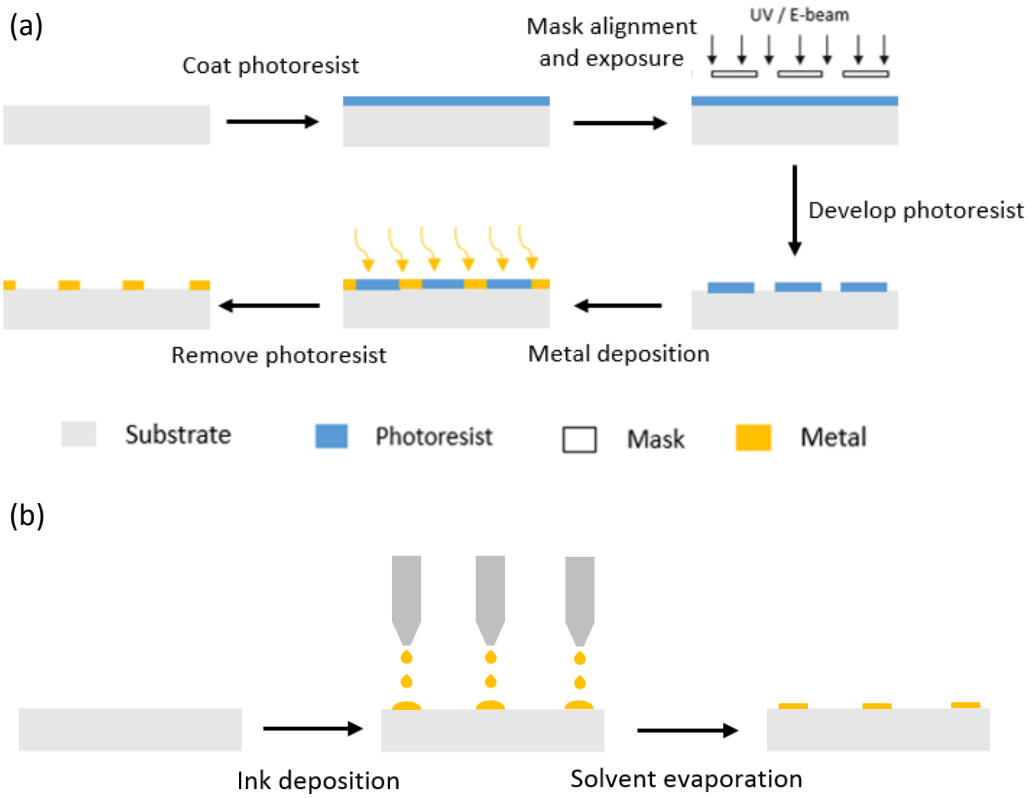



Figure 1-1: Schematic of (a) photolithography and (b) non-contact printing as patterning techniques.

Despite the advantages, there are some current issues with non-contact printing as a fabrication process for flexible electronics. Firstly, the achievable resolution of printing processes is inferior compared to nanolithography techniques, which limits the size and precision to which features can be printed.[13] This is detrimental to the overall areal density of printed devices and reduces the performance of some types of devices like transistors and transparent conducting grids.[14]

The material properties of printed material is another limitation as they are usually inferior to those used in traditional devices, leading to poorer devices performanes.[15] Printed materials are largely based on polymeric and nanomaterial inks. Polymers generally have slower charge transport properties than inorganic semiconductors while nanomaterial inks require surfactants to maintain colloidal stability prior to printing.[16,17] In addition, inks usually contain additives that tune their rheology.[18] These additional chemicals disrupt the structure of the printed materials, leading to poorer properties in the final printed parts. This is a particularly pertinent problem when printing conductive materials.

### 1.2 Printing Conductive Structures

Conductive materials are necessary components of any electronic device. Inks consisting of carbon nanotubes, graphene, conducting polymers and metallic nanomaterials have all been used to print conductive structures.[19–22] Among these materials, metallic nanomaterials can achieve the highest conductivities due to the inherent conductivity of the bulk metals. Silver is one of the most popular materials due to its high conductivity among metals and its oxidative stability. Silver nanoparticle (AgNP) inks are the most commonly used in printing due to their small sizes which makes them compatible with many high resolution printing techniques.[1] Conversely, silver nanowires (AgNWs) are not as frequently used due to their large sizes, making them prone to nozzle clogging.[23] However, AgNW inks can form more conductive structures due to high conduction along the length of the nanowire.[24]

The main challenge in using AgNW inks is the inherent trade-off between conductivity and ink stability. AgNWs, like all nanomaterials, tend to aggregate when dispersed in solution due to their high surface area to volume ratio. As a result, stabilizing ligands are usually attached to the surface of the nanowires to provide steric or electrostatic stabilization.[25]

These ligands exert repulsive forces when neighbouring nanowires move too close together and therefore allow the nanowires to be well dispersed in the ink. However, after the nanowire ink is printed, the stabilizing ligands become barriers for charge transfer between neighbouring nanowires.[17] This increases the junction resistance between nanowires and contributes to the overall resistivity of the nanowire film. Usually, this issue is circumvented by post-treatment processes on the printed structures that remove the ligands and fuse the nanowire junctions to decrease the junction resistance.[26] However, in certain scenarios, this is undesirable as the treatment may affect underlying materials or cause parts of the structure to rupture due to volume shrinkages when the ligands are removed.[27] Therefore, it would be good to devise a strategy to achieve high conductivity AgNW structures without the need for post-treatment.

### 1.3 Stretchable Electronics

Another advantage of 1D AgNWs is their high aspect ratios. This allows for higher tensile strain tolerance in the printed structures as they can still maintain contact when the overall network is stretched.[28] As a result, stretchable conductors and devices can be made which add another dimension to potential applications such as wearable electronics.[15] An interesting property which results from the stretching of AgNW networks is piezoresistivity. This means that the resistivity of the material changes with applied pressure. Piezoresistivity arises from the percolative nature of the AgNW network. Any changes to the geometry of the network alters the connectivity of the network and thus the overall resistivity.[29] This property allows AgNWs to be used as pressure sensors.

The development of wearable and flexible electronics has created a demand for high performance pressure sensors for new applications in health monitoring and artificial skin

for robotics.[30] As these applications function in the low-pressure regime of < 100 Pa, there is a clear need for pressure sensors with higher sensitivity.[31] The piezoresistive nature of AgNW films makes them prime candidate for this application. Compared to other transduction mechanisms like capacitive and piezoelectric, piezoresistive pressure sensors have the advantages of having high sensitivity and simple device structures.[32]

### 1.4 Aim of Thesis

The aim of this thesis is to address some of the challenges faced in the field of printed electronics pertaining to the printing of conductive materials for the fabrication of stretchable conductive composite films based on AgNWs. Solutions to improve printing resolution and material property of the printed structures will be explored. These techniques will then be applied in fabricating highly sensitive flexible pressure sensors. The following concepts will be explored in this thesis:

(i) The resolution of non-contact printing can be improved with the aid of additional forces like electric fields or air flows. Is the use of solvent-solvent interactions another possible solution to improve printing resolution of non-contact printing techniques? The use of an additional carrier solvent which is immiscible with the ink to reduce the size of the ink footprint ejected from the printer nozzle and impedes ink spreading on the substrate will be explored. This technique will be called solvodynamic printing.

(ii) Can the conductivity of printed AgNW structures be improved without the need for post-treatments by changing the types of ligand on the as-synthesized AgNWs? The use of linker ligands to improve the conductivity of AgNW films will be studied.

(iii) Can highly sensitive flexible piezoresistive pressure sensors be fabricated using non-contact printed AgNWs? The use of pressure-induced tensile strains in AgNW composite films will be used to make high sensitivity pressure sensors. The sensitivity can be further boosted by patterning the AgNW using solvodynamic printing.

### 1.5 Structure of Thesis

Chapter 2 provides a literature review relating to the research challenges presented earlier in this chapter. Some fundamental concepts will be discussed along with current solutions in literature. Chapter 3 introduces the concept of solvodynamic printing and shows its proof-of-concept in improving printing resolution. The underlying working principle is also explored. Chapter 4 studies the use of linker ligands on AgNWs to improve their conductivity when being printed. The ligand exchange between PVP and some di-acid and di-amine based ligands will be studied. Chapter 5 explores the pressure sensing abilities of a solvodynamic printed AgNW embedded in ethylene-co-vinyl acetate composite film. Pressure sensing using both compressive and tensile strains are compared. The tuning of sensing ability is also explored. Chapter 6 concludes the findings of the thesis and outlines possible future work that can be done.

## 1.6 References


1. Kamyshny, A. & Magdassi, S. Conductive nanomaterials for 2D and 3D printed flexible electronics. *Chem. Soc. Rev.* **48**, 1712–1740 (2019).

2. Ling, H., Liu, S., Zheng, Z. & Yan, F. Organic Flexible Electronics. *Small Methods* **2**, 1800070 (2018).

3. Chortos, A. *et al.* Mechanically Durable and Highly Stretchable Transistors Employing Carbon Nanotube Semiconductor and Electrodes. *Adv. Mater.* **28**, 4441–4448 (2016).

4. Gangnaik, A. S., Georgiev, Y. M. & Holmes, J. D. New Generation Electron Beam Resists: A Review. *Chem. Mater.* **29**, 1898–1917 (2017).

5. Wu, W. Inorganic nanomaterials for printed electronics: A review. *Nanoscale* **9**, 7342–7372 (2017).

6. Dou, B. *et al.* Roll-to-Roll Printing of Perovskite Solar Cells. *ACS Energy Lett.* **3**, 2558–2565 (2018).

7. Choi, H. *et al.* UV-Curable Silver Electrode for Screen-Printed Thermoelectric Generator. *Adv. Funct. Mater.* **29**, 1–6 (2019).

8. Huang, Q. & Zhu, Y. Gravure Printing of Water-based Silver Nanowire ink on Plastic Substrate for Flexible Electronics. *Sci. Rep.* **8**, 1–10 (2018).

9. Secor, E. B. Principles of aerosol jet printing. *Flex. Print. Electron.* **3**, (2018).

10. Grubb, P. M., Subbaraman, H., Park, S., Akinwande, D. & Chen, R. T. Inkjet printing of high performance transistors with micron order chemically set gaps. *Sci. Rep.* **7**, 1–8 (2017).

11. Khan, S., Lorenzelli, L. & Dahiya, R. S. Technologies for printing sensors and electronics over large flexible substrates: A review. *IEEE Sens. J.* **15**, 3164–3185 (2015).

12. Raut, N. C. & Al-Shamery, K. Inkjet printing metals on flexible materials for plastic and paper electronics. *J. Mater. Chem. C* **6**, 1618–1641 (2018).

13. Fukuda, K. & Someya, T. Recent Progress in the Development of Printed Thin-Film Transistors and Circuits with High-Resolution Printing Technology. *Adv. Mater.* **29**, (2017).

14. Kim, S. *et al.* Ultrathin high-resolution flexographic printing using nanoporous stamps. *Sci. Adv.* **2**, (2016).

15. Zou, M. *et al.* Flexible devices: From materials, architectures to applications. *J. Semicond.* **39**, 0–18 (2018).

16. Kokil, A., Yang, K. & Kumar, J. Techniques for characterization of charge carrier mobility in organic semiconductors. *J. Polym. Sci. Part B Polym. Phys.* **50**, 1130–1144 (2012).

17. Kim, J. Y. & Kotov, N. A. Charge transport dilemma of solution-processed nanomaterials. *Chem. Mater.* **26**, 134–152 (2014).

18. Derby, B. Inkjet Printing of Functional and Structural Materials: Fluid Property

Requirements, Feature Stability, and Resolution. *Annu. Rev. Mater. Res.* **40**, 395–414 (2010).

19. Menon, H., Aiswarya, R. & Surendran, K. P. Screen printable MWCNT inks for printed electronics. *RSC Adv.* **7**, 44076–44081 (2017).

20. Pan, K. *et al.* Sustainable production of highly conductive multilayer graphene ink for wireless connectivity and IoT applications. *Nat. Commun.* **9**, (2018).

21. Aziz, A. *et al.* 1D copper nanowires for flexible printable electronics and high ampacity wires. *Nanoscale* **9**, 13104–13111 (2017).

22. Bihar, E. *et al.* Inkjet-Printed PEDOT:PSS Electrodes on Paper for Electrocardiography. *Adv. Healthc. Mater.* **6**, (2017).

23. Cui, Z., Han, Y., Huang, Q., Dong, J. & Zhu, Y. Electrohydrodynamic printing of silver nanowires for flexible and stretchable electronics. *Nanoscale* **10**, 6806–6811 (2018).

24. Stewart, I. E., Jun Kim, M. & Wiley, B. J. Effect of morphology on the electrical resistivity of silver nanostructure films. *ACS Appl. Mater. Interfaces* **9**, 1870–1879 (2017).

25. Kanelidis, I. & Kraus, T. The role of ligands in coinage-metal nanoparticles for electronics. *Beilstein J. Nanotechnol.* **8**, 2625–2639 (2017).

26. Langley, D. P. *et al.* Metallic nanowire networks: Effects of thermal annealing on electrical resistance. *Nanoscale* **6**, 13535–13543 (2014).

27. Reiser, B., González-García, L., Kanelidis, I., Maurer, J. H. M. & Kraus, T. Gold nanorods with conjugated polymer ligands: Sintering-free conductive inks for printed electronics. *Chem. Sci.* **7**, 4190–4196 (2016).

28. Lee, H., Kim, I., Kim, M. & Lee, H. Moving beyond flexible to stretchable conductive electrodes using metal nanowires and graphenes. *Nanoscale* **8**, 1789–1822 (2016).

29. Amjadi, M., Pichitpajongkit, A., Lee, S., Ryu, S. & Park, I. Highly stretchable and sensitive strain sensor based on silver nanowire-elastomer nanocomposite. *ACS Nano* **8**, 5154–5163 (2014).

30. Huang, S., Liu, Y., Zhao, Y., Ren, Z. & Guo, C. F. Flexible Electronics: Stretchable Electrodes and Their Future. *Adv. Funct. Mater.* **29**, 1–15 (2019).

31. Zang, Y., Zhang, F., Di, C. A. & Zhu, D. Advances of flexible pressure sensors toward artificial intelligence and health care applications. *Mater. Horizons* **2**, 140–156 (2015).

32. Li, J., Bao, R., Tao, J., Peng, Y. & Pan, C. Recent progress in flexible pressure sensor arrays: From design to applications. *J. Mater. Chem. C* **6**, 11878–11892 (2018).

# Chapter 2 - Literature Review

## 2.1 Achieving High Resolution in Non-Contact Printing Technologies

The resolution of a printing technique describes how closely two neighbouring printed features can be positioned. The value of resolution is usually described by either the number of possible printed lines per unit length or by the smallest line width possible.[1] Inkjet printing, one of the most commonly used non-contact printing technique can achieve resolutions between 20 to 50 μm.[2] This is still insufficient for applications such as transistors. Ideally, resolutions down to micron scale (1-10 μm) is desirable for good performance for flexible electronics. In this review, inkjet printing will be used as the starting point as it is one of the main non-contact printing technique and has helped to create other printing techniques that will be discussed later. The factors limiting printing resolution will be identified and current methods to overcome these factors will be reviewed.

In inkjet printing, a printhead holds a reservoir of ink. During printing, thermal or piezoelectric actuators are used to eject droplets from the print head nozzle as shown in Figure 2-1a. The printhead is moved relative to the substrate to print the desired pattern.[3] The resolution of inkjet printing, *d* can be described by the following equation[4]:

$$d = d_0 \sqrt{\frac{8}{\tan\frac{\theta}{2} + (3 + tan^2\frac{\theta}{2})}} \tag{2-1}$$

where $d_0$ is the diameter of the ink droplet ejected from the nozzle and $\theta$ is the equilibrium contact angle of the ink on the substrate. From this equation, it can be inferred that in general terms for non-contact printing, resolution is determined by the footprint of the ink ejected from the nozzle and the ink wettability on the substrate.[5]

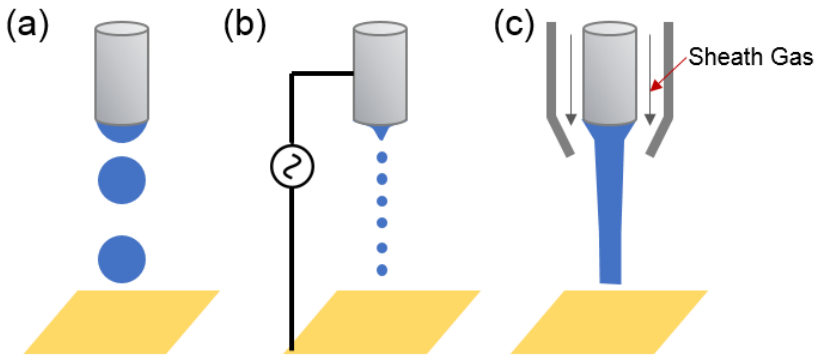



Figure 2-1: Schematics of (a) inkjet printing, (b) electrohydrodynamic printing and (c) aerosol jet printing.

### 2.1.1 Controlling Ink Footprint

#### 2.1.1.1 Electrohydrodynamic Printing

For inkjet printing, the volume of ink dispensed in each droplet is largely controlled by the printhead and nozzle. A smaller nozzle can generally create smaller droplets which leads to higher resolution. However, there is a limit to how small the nozzle can be as smaller nozzles make it more difficult for ink droplets to be ejected due to capillary and surface tension effects.[6] The current technology of inkjet printing uses nozzles with dimensions between 20 – 70 μm and can produce ink droplets with volumes on the scale of 1 – 100 pl.[7] This corresponds to a resolution in the range of several tens of microns.

To generate ink droplets with smaller volumes, electrohydrodynamic (EHD) printing was developed. It was found that the use of an electric field can help to pull out smaller ink droplets from small nozzles. In EHD printing, a high voltage is applied between the printer nozzle and the substrate which usually have a separation in the range of 100 μm. The strong resultant electric field pulls ions in the ink towards the meniscus at the nozzle tip. As the ions are attracted towards the substrate, they get pulled downwards and form a fine conical structure called a Taylor's cone. If the Columbic forces exceed the surface tension of the ink, small droplets can be pulled out of the Taylor's cone towards the substrate as shown in

Figure 2-1b. EHD printing can generate droplets with volumes in the femtolitre range.[8] By adjusting printing parameters such as ink pump rate, applied voltage magnitude and waveform, different printing modes like jetting, dripping and cone-jetting can be achieved for different printing performances.[9]

EHD printing has been successfully used to fabricate high resolution structures with a variety of materials. Lee et al. managed to print 15 μm wide silver grids from a 100 μm diameter nozzle with an applied voltage of 1.5 kV.[10] This shows how EHD printing can form features smaller than the nozzle diameter. With the use of EHD printing, smaller nozzle sizes are also usable as the electric fields can help to pull out ink droplets. Kim et al. used a 2 μm nozzle to print lines of indium (III) oxide with widths of 2 μm as channels in a MOSFET transistor.[11] This is a large improvement compared to inkjet printing. Lee et al. and Min et al. showed further possible improvement in resolution into sub-micron range by increasing the nozzle-to-substrate distance to 7 mm. The larger nozzle-to-substrate distance allows for the ejected ink jet to partially dry mid-flight to further reduce the feature size. Using a 100 μm nozzle, Lee et al. managed to print poly(4-vinylpyridine) filaments with widths of 375 nm and Min et al. printed silver wires with widths of 695 nm.[12,13] At the time of writing this thesis, one of the highest resolution achieved was demonstrated by Galliker et al..[14] They downscaled the EHD printing dripping mode to a "Nanodrip mode" using small nozzles with diameters down to 600 nm and short nozzle-to-substrate distances below 5 μm. The Nanodrip printing mode could extract attolitre range droplets from the nozzle meniscus to produce printed features down to 50 nm. The ink composition and rheology were also adjusted to allow the droplets to dry before reaching the substrate. Therefore, droplets can be repeatedly deposited without drastically affecting the feature size.

The focusing effect of EHD printing also allows for nanomaterials with larger dimensions to be used in printing. To reduce nozzle clogging, it is usually recommended for nanomaterials to have dimensions of about 1 % of the nozzle diameter.[15] This means that larger 1D and 2D nanomaterials are typically not suited for traditional non-contact printing techniques. However, EHD printing can use large nozzles while still achieving high resolution. Lee et al. performed EHD printing of AgNW-poly(ethylene oxide) composite ink from a 200 μm nozzle to print ribbons of aligned AgNWs with widths of 15 μm.[16] Unfortunately, the silver nanowires were not connected sufficiently for the ribbons to be conductive. More recently, Cui et al. printed highly conductive AgNW tracks of 45 μm from a 150 μm nozzle.[17]

EHD is definitely the current state-of-the-art high-resolution non-contact printing technique for flexible electronics, achieving sub-100 nm resolution using the Nanodrip mode and high tunability based on the printing parameters. The downside of EHD is that a large voltage source is required in its setup. Typically, the required voltage for printing at high resolution is greater than 1000 V. There is also a trade-off between resolution and throughput as methods like Nanodrip which fabricate structures drop by drop using such tiny droplets takes a long time to print complete circuits or devices. Printing with continuous jets can increase printing speed at the cost of resolution.[18] However, depending on the conductivity of the ink and substrate used, shorting may occur between the nozzle and the substrate and terminate printing.[19]

#### 2.1.1.2 Aerosol Jet Printing

Another method developed for high resolution printing is aerosol jet printing (AJP). In AJP, the liquid ink is first atomized into micron-sized droplets by ultrasonication. A carrier gas

brings the ink droplets to the deposition head, where a sheath gas is applied around the carrier gas stream. The sheath gas flows alongside the carrier gas stream and focuses it into a smaller collimated beam. The gases then exit the deposition nozzle and are directed towards the substrate for printing as shown in Figure 2-1c. Enhancement in resolution arises from two sources. As the atomization process forms very fine droplets, solvent evaporation occurs quickly and the ink droplets shrinks further. This reduces the droplet size and minimizes spreading on the substrate. The sheath gas also directly improves the printing resolution as it can focus the carrier gas stream into a smaller diameter. The ratio between the volumetric pump rate of sheath gas to carrier gas is called the focusing ratio (FR).

Mahajan et al. studied how different printing parameters affected the final resolution of AJP of silver lines. They showed that increasing the FR used can compensate for the use of a larger nozzle. Silver lines of 20 μm width could be produced using either a nozzle of 200 μm diameter with a FR of 10 using or a nozzle of 150 μm with a FR of 5. It was found that the AJP process was limited by the pressure within the deposition head, which should not become too large. Therefore, the FR could not be increased indefinitely to achieve better resolution.[20] More recently, Jahn et al. and Oakley et al. reported improved results from their AJP experiments. They managed to print silver lines with line widths down to 10 μm using 100 μm nozzles.[21,22]

AJP has a simpler working mechanism than EHD with easier control and has successfully improved printing resolution over inkjet printing to approximately 10 μm. The key issue in AJP is the overspray of material at the edges of the printed lines. This makes the printed lines have less uniform edges and deteriorates the true resolution achievable.[23] The use of high sheath gas flow may also be undesirable for printing on some types of underlying

materials, especially if the adhesion or mechanical properties of those materials are not sufficiently strong.[24]

The development of AJP and EHD printing present different ways to improve printing resolution effectively. However, both methods have their respective drawbacks. Therefore, the development of new techniques which can improve resolution using different mechanisms could be beneficial to the field of non-contact printing.

### 2.1.2 Ink Wettability on Substrate

Aside from controlling the ink footprint from the printer nozzle, the wettability of the printing ink on the substrate is another factor which affects the final achievable resolution of the printing technique as it affects how much the ink spreads outwards on the substrate.[25] This is characterized by the contact angle as shown in Figure 2-2. A larger contact angle corresponds to less ink spreading on the substrate and leads to higher resolution. The equilibrium contact angle is determined by the balance between three pairs of interfacial tensions between the ink, substrate and air and is mathematically described by the Young's equation[26]:

$$cos\theta = \frac{\sigma_{sa} - \sigma_{si}}{\sigma_{ia}} \tag{2-2}$$

where $\sigma_{sa}$, $\sigma_{si}$ and $\sigma_{ia}$ are the substrate-air, substrate-ink and ink-air interfacial energies and $\theta$ is the resultant contact angle of the ink.

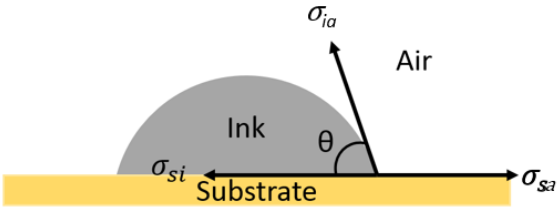



Figure 2-2: Schematic diagram showing the determination of contact angle, $\theta$. $\sigma_{si}$, $\sigma_{ia}$, $\sigma_{sa}$ are the interfacial tensions between substrate-ink, ink-air and substrate-air respectively.

#### 2.1.2.1 Controlling Contact Angle

From the Young's equation, it can be seen that the contact angle can be increased either by using an ink with high surface tension or substrate with lower surface energy. There is typically less room for tuning the surface tension of the ink as higher surface tension makes the ink more difficult to be ejected from the nozzle.[7] Lessing et al. adopted the strategy of tuning the substrate surface energy by applying a chemical treatment of fluorinated organosilanes on a paper substrate. This reduced the wettability of the ink on the paper substrate. Using this technique, they managed to decrease line widths by a factor of 5 compared to an untreated substrate from 585 μm to 90 μm. By controlling the droplet size generated by their inkjet printer, the maximum resolution achieved was 28 ± 5 μm.[27] Kim et al. performed inkjet printing on a fluorine treated porous polyimide substrate. Fluorine treatment decreased the surface energy of the substrate. The contact angle of the ink further increased due to the surface roughness of the porous substrate. Using their modified substrate improved the resolution from 140 μm to 30 μm.[28] The modification of substrate surface yielded a decent improvement. However, it is likely that this technique only works well for porous substrates as it can probably avoid ink dewetting due to capillary forces in the paper fibres. For other commonly used plastic substrates, the resultant large contact angles may cause the printed lines to be destabilized and break up into a line of round droplets due to Rayleigh instability.[29]

#### 2.1.2.2 Pre-patterning Substrates

Another strategy used to alter the wettability of the substrate while avoiding the Rayleigh instability is to prepattern the substrate. The prepatterning done can be chemical or physical in nature. Suzuki et al. used a photomask to perform a UV treatment on a hydrophobic polyimide substrate. The areas exposed to the UV resulted in an increase in surface energy

compared to the unexposed areas. When a hydrophilic silver ink was printed on the substrate, the ink preferentially moved onto the high surface energy regions and away from the untreated regions. Thin silver electrodes with line widths of 15 μm were eventually achieved.[30] Nguyen et al. used a similar strategy using ozone plasma treatment to treat a hydrophobic surface with the aid of a magnetic nickel stencil. PEDOT:PSS features with line widths of 35 μm were fabricated from ink droplets approximately 55 μm in diameter.[31] Wu et al. used photolithography to pattern hydrophilic spots on a hydrophobic substrate to achieve very small features < 10 μm in size. The ink droplets were much larger than the patterned spots but they receded towards the centre of the spots after deposition, forming dome-like structures. They also used different spot patterns to produce printed structures with different geometry.[32]

Similar strategies using physical patterning have also been presented in literature. Mahajan et al. made use of imprint lithography to prepattern their substrate prior to inkjet printing. A polydimethylsiloxane (PDMS) stamp was pressed against an epoxy resin which is then cured to produce small 2 μm wide groove structures that were connected to a larger reservoir structure in the epoxy substrate. Silver ink was then inkjet printed onto the reservoir area. The ink was drawn into the grooves via capillary forces. The silver filled channels were then used as a seed layer for electroless plating of copper.[33] Song et al. also performed similar procedure to form 5 μm wide silver coated channels for fabricating thin film transistors.[34]

Such prepatterning techniques are certainly capable of drastically improving printing resolution beyond the current limit of non-contact printing without modifying the printing mechanism. However, the prepatterning step typically involves the use of masks along with a high-resolution lithographic patterning technique which drives up the complexity and

costs of the process. Furthermore, the prepatterning step is a batch process which brings down the throughput of the overall procedure. Nevertheless, these strategies exist as middle ground between pure nanolithography methods and non-contact printing techniques with a compromise between cost and performance.

So far, this chapter has covered key developments in high resolution non-contact printing techniques. The reduction of ink footprint from the nozzle is a key concept that should be explored. Aside from simply improving resolution, larger nozzles can also be used to print inks containing larger nanomaterials. This is particularly useful for printing conductive materials such as AgNWs for conductive tracks which can achieve high conductivity with a lower overall metal loading than other forms of nanomaterials such as AgNPs. In the next section, the properties of printed AgNWs as a printable conductive material will be explored.

## 2.2 Electrical Properties of Printed Silver Nanowire Films

AgNWs are high aspect ratio 1D nanostructures with diameters less than 100 nm and typical lengths in the range of tens of microns. They are typically synthesized via the polyol process which is very well-studied and repeatable.[35,36] Random networks of AgNWs can form highly conductive networks even at low nanowire densities as conduction occurs quickly through the length of the nanowires. The electrical properties of AgNW networks can be described using percolation theory.[37]

### 2.2.1 Percolation Theory

Percolation theory describes the connectivity of randomly dispersed objects in a network.[38] According to percolation theory, the conductivity of a random network of AgNWs is highly dependent on the density of nanowires in the film. At low densities, the conductivity of the

network is zero as there are insufficient nanowires to form any connection through the film. As the nanowire density increases, the nanowires in the film starts to become closer to each other. At the percolation threshold density, sufficient nanowires are present such that conductive pathways begin to form and the conductivity increases rapidly. The conductivity of the network continues to increase with nanowire density as more pathways are formed. Mathematically, percolation theory predicts that the conductivity of a percolation network close to the percolation threshold can be described empirically by the power law[38]:

$$\sigma = \sigma_0 (N - N_c)^t \tag{2-3}$$

where $\sigma$ is the conductivity of the network, $\sigma_o$ is a system dependent pre-exponential factor, $N$ is the nanowire density, $N_c$ is the percolation threshold and $t$ is the critical exponent. The pre-exponential factor is a parameter that depends on the resistivity of the nanowire, their junction resistance and film morphology.[39] The power law is valid for both 2D AgNW films deposited on a flat substrate and 3D AgNW networks which are usually formed within a matrix material. In the case of 3D networks, $N$ and $N_c$ should be replaced with the volume fraction, $\phi$ and threshold volume fraction, $\phi_c$ of nanowires respectively.

The percolation threshold of an AgNW network is highly dependent on the geometry of the nanowires. Li and Zhang have modelled percolation of nanowires as 1D width-less sticks using Monte Carlo simulations that the percolation threshold of a 2D nanowire network is inversely proportional to the length of the nanowires, $l$:[40]

$$N_c = \frac{5.63726}{l^2} \tag{2-4}$$

This makes sense as it is easier for longer nanowires to intersect with each other. Therefore, conduction can occur at a lower nanowire density. It also follows from equation 2-3 that

longer nanowires can form higher conductivity networks given a fixed nanowire density. In the 3D case, Garbozi et al. showed that the percolation threshold is inversely related to the aspect ratio of nanowires according to[41]:

$$\phi_c = 0.6\frac{D}{L} \tag{2-5}$$

Once again, longer nanowires contribute to lower percolation threshold. In this case, the diameters of the nanowires were considered in the simulation. Since increasing the diameter does little to improve the percolation but increases the volume fraction of the nanowire at a fixed length, it varies positively with the threshold volume fraction.

The critical exponent, *t* describes the scaling of conductivity with increasing nanowire density. Theoretically, it has been well-established that the critical exponent takes a value of 1.33 for a 2D network and a value of 2 for a 3D network. Although this has been verified by many experimental reports, some studies have also shown deviation of the critical exponent form these theoretical values. The deviation is usually reported in 3D networks of conductive composites. This observation is usually explained by the occurrence of tunneling conduction in real-life composite materials when the conductive fillers are sufficiently close but not in direct contact.[42–44]

Although the power law is theoretically only valid for nanowire densities around the percolation threshold, many experiments have found empirically that the variation in conductivity may continue to follow the rule over large range of nanowire densities. Keblinski and Žeželj performed independent studies on this phenomenon on 3D and 2D percolative networks respectively. In the 3D case, Keblinski found that the critical exponent remained as $t = 2$ even when $\phi >> \phi_c$ if the junction resistance between neighbouring nanowire is much larger than resistance of a single nanowire. Otherwise, the critical

exponent starts to deviate to $t = 1$ when $\phi > 2\phi_c$.[45] For 2D networks, a similar divide in critical exponent was found. In junction resistance dominant networks, the critical exponent varies gradually from $t = 1.33$ at $N = N_c$ to $t = 2$ when $N = 1$. Conversely, in nanowire resistance dominant network, the critical exponent varies to $t = 1$ when $N = 1$.[46] Given the results, the analysis of nanowire networks needs to be done with care. For untreated AgNW networks, the resistance should be largely junction resistance dominant due to the presence of insulating ligands on their surfaces.[47]

### 2.2.2 Role of Junction Resistance in Silver Nanowire Films

The junction resistance in nanowire films is a commonly studied topic as it is the main factor limiting the overall conductivity of AgNW films. AgNWs are usually capped with large bulky stabilizing surfactants, typically polyvinylpyrrolidone (PVP). The surfactants are also essential in the synthesis of the nanowires to ensure anisotropic growth occurs. The charge transport at nanowire junctions can be characterized as two main ways.[48] Transport at a metal-insulator-metal junction is dominated by tunneling, which generally leads to high junction resistance.[49] Charge transport is determined by the barrier energy and thickness. Another possible junction formed is a metal-molecule-metal junction. Transport at these junctions are characterized as electron hopping.[50] In this case, the charge transport across the junction is dependent mainly on the properties of the linking molecule such as length, conformation and molecular orbital levels relative to the metal's.[51]

Many studies have tried to quantify the junction resistance between two AgNWs using direct measurements or semi-empirical methods. Most of the reports showed that the junction resistance of untreated AgNWs is in the range of 30 kΩ to > 1 GΩ.[52–54] In contrast, the resistivity of a single AgNW has been measured to be close to the resistivity of bulk

silver.[47,55] The much higher junction resistance limits the overall conductivity and sheet resistance of the AgNW films. Untreated films often achieve sheet resistances in excess of several kilo-ohms per square depending on the AgNW loading.[52–54]

More recently, two junction resistance measurement studies done by Bellew et al. and Selzer et al. showed contrasting results from the previous studies and found that junction resistance of untreated nanowire junctions were only approximately 500 Ω.[56,57] This seems to contradict prior reports but upon closer look, this may be due to the different nanowires used in the studies. The latter studies used commercial nanowire inks which were characterized to have a thin 1-2 nm PVP layer on the surface. On the other hand, as-synthesized nanowires which typically has a much thicker PVP layer ranging from 3 – 30 nm.[49,58] This could explain the discrepancy in reported junction resistances and also highlight the importance of the surface ligand structure on the nanowires in relation to the resultant junction resistance in the AgNW films.

### 2.2.3 Methods of Reducing Junction Resistance

#### 2.2.3.1 Post-Treatments

As mentioned in the previous section, untreated AgNW films often have high sheet resistances. Post-treatments on AgNW films after deposition are the most common way to improve the network conductivity to improve their functionality in devices. Post-treatments used in other solution processed metallic nanomaterial films will also be reviewed as they encounter the same issue as AgNWs. Traditionally, post-treatments are done by thermal annealing at temperatures above 180 °C for annealing times of 30 mins or more.[59,60] The glass transition temperature of PVP is at around 150 °C. Therefore, the PVP around the junctions starts to flow away and creates better contact between the nanowires. The high

temperature then induces sintering of the nanowire junctions. Studies have shown that the fused junctions have much lower resistances of about 11-20 Ω.[57,61] However, this method is typically not compatible with plastic substrates commonly used in printed electronics. Other forms of non-thermal post-treatments have subsequently been developed to tackle this problem.

One main group of alternative post-treatment involves methods which remove PVP from nanowire junctions by creating a localized area of heating within the nanowire film without affecting the substrate. This can be done using microwave radiation[62–64], electrical currents[52,65–67] and photonics[68–72]. Microwaves can generate rapid heating rates in the nanowires for sintering to occur. The process is fast and can usually be completed within several minutes.[73] Although microwaves have a short penetration depth in metals, it can still be used in metallic nanomaterials as the surface area is large and high thermal conductivity helps to create even heating within the film. Electrical currents can create a similar effect by inducing Joule heating when a current is forced to pass through the highly resistive junctions. Electromigration of silver atoms can also occur to facilitate the sintering process.[52] Photonics sintering can be done with lasers or intense pulsed lights. The strong light exposures heat up the nanowire surface rapidly for sintering to occur. Short flashes of high-powered light with exposure times in the range of milliseconds are sufficient for sintering to occur.

Another alternative post-treatment involves removal of the PVP using plasmas. Reactive hydrogen or ozone plasmas, as well as inert argon plasmas can be applied to AgNW films to decompose or physically remove the PVP.[74–76] The energy from the plasma was also thought to induce some degree of sintering at the junctions. The process is also slightly

slower, with treatment times in the range of 10 mins. Other post-treatments involve increasing the area of contact between nanowires at the junction. This can be done by welding the junctions by depositing an overcoat of conductive material around the junction. This is commonly done by an electroplating step or reduction of metal ions after deposition of the AgNW network.[77–80]

#### 2.2.3.2 Chemical Treatments

In general, the post-treatments can be used to fabricate highly conductive nanowire films. However, most of them involve the use of specialized equipment or involve high power sources. Sintering using chemical methods are much simpler to perform. As highlighted previously, the junction resistance in AgNW films are highly dependent on the structure of the surface ligands on the nanowire surfaces. There are several classes of chemical sintering methods which targets these surface ligands. One method involves exposing the silver films to chemically reactive species which can perform sintering in different ways depending on the type of chemical species used. Coutts et al. found that applying nitrogen dioxide to thiol-stabilized gold nanoparticles can improve the film conductivity. The oxidizing nitrogen dioxide reacts with the thiol groups on the ligands and reduces their ability to bind to the gold surfaces. This resulted in the removal of the thiol ligands on the gold nanoparticles.[81] More recently, Yoon and Khang reported the use of hydrogen peroxide vapours to perform chemical welding of AgNW junctions. They suggested that the hydrogen peroxide preferentially condensed at the junctions due to capillary effect. The junction welding then occurred due to the partially dissolution and drying of silver at the junctions when being exposed strongly oxidizing hydrogen peroxide.[82]

The most common type of chemical sintering involves performing ligand exchange on the nanowires. Small chemical species which bind preferentially to the nanowires can be applied to the film. Ligand exchange on the nanowires occurs between the stabilizing ligands and this new chemical species. Once the new ligand attaches onto the nanowires, it induces agglomeration as it does not provide much steric or electrostatic stabilization. Halide compounds have been the main chemical species used in this way for nanowire films.[83–86] In contrast, a much more diverse range of ligands have been studied in nanoparticle films as shown in Figure 2-3.[87–93] The ligands can improve charge transport mainly by reducing the distance between nanoparticles or by creating a more ordered arrangement of nanoparticles.

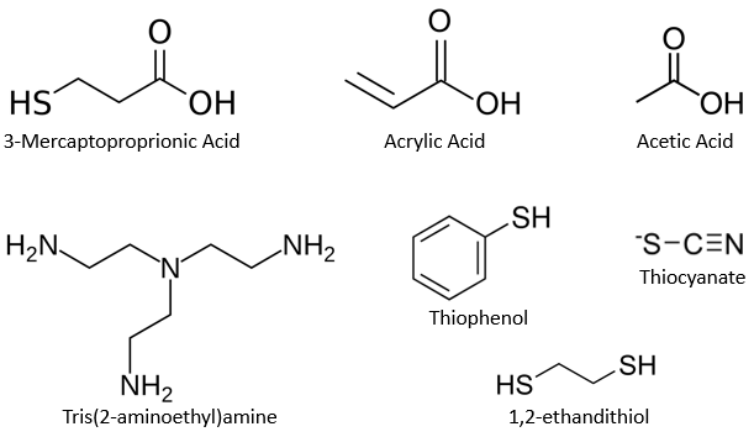



Figure 2-3: Some ligands used to improve charge transport between metallic nanoparticle films.

2.2.3.3 Treatment Free Conductive Films

A further possible improvement is to eliminate the need for post-treatment altogether. This brings improvements to processability and throughput as less steps are involved in the device fabrication process.

There have been a few reports of treatment free AgNW or nanoparticle ink formulations for fabricating conductive networks. One type of strategy targets reducing the thickness of PVP on the AgNWs to improve charge transport across nanowire junctions. Wang et al. performed multiple washing steps with different solvents and different conditions on AgNWs to maximize the removal of PVP on the nanowire surface. Through four wash cycles with ethanol and one additional wash cycle with water or dimethylformamide at elevated temperatures, the PVP thickness on the nanowire surface was reduced from about 13 nm to 1 nm. The AgNW ink was used to make transparent films with sheet resistance 15.6 Ω/□ with transmittance of 90%.[94]

Grouchko et al. combined the strategy of chemical sintering into the ink formulation by adding a small amount of destabilizer halide into the ink. Only a low concentration of the halide compound was added to the ink so that the ink could remain stable prior to printing. The chemical sintering was only induced after printing. During solvent evaporation, the concentration of the halide destabilizer will increase and start to remove the capping ligands from the nanoparticles, causing agglomeration and sintering of the silver nanoparticles. Using this sinter-free ink, conductive structures with resistivities of 0.16 μΩm which is 10 times that of bulk silver were formed.[95]

Another type of strategy for treatment free nanowire films involve the use of additional conductive materials to increase the conduction pathways between neighbouring nanowires. Reiser et al. used highly conjugated polymers as ligands for gold nanorods to achieve balance between colloidal stability and conductivity after printing. The polymer provides good steric stabilization before printing and is also conducting due to its conjugated π-bonds present in its structure. Gold nanorods with poly[2-(3-thienyl)-ethyl- oxy-4-butylsulfonate]

(PTEBS) and poly(3,4-ethylenedioxythiophene) polystyrene sulfonate (PEDOT:PSS) as ligands were fabricated and used to print lines. The PTEBS ligand sample achieved 7.0 μΩm while the PEDOT:PSS ligand sample achieved 0.99 μΩm, which corresponded to 280 times and 40 times the resistivity of bulk gold respectively.[96]

Nanoparticles have also been used in similar ways in nanowire inks. Su et al. added a small amount of gold nanoparticles to their AgNW ink. The nanoparticles self-assembled at the nanowire junctions during drying and thus increased the contact area to improve the junction resistance of the nanowire network. Films with the gold nanoparticles achieved a sheet resistance of 13.9 Ω/□ with transmittance of 86% while the film without nanoparticles achieved 13.4 Ω/□ at only 39% transmittance.[97] Menamparambath et al. used the addition of AgNPs to reduce the sheet resistance of the AgNW film by 29.5%.[98]

The strategies developed in chemical sintering and treatment free techniques highlight the importance of the surface properties of the AgNWs in the final film electrical property. With careful manipulation of the ligand shell thickness or the type of ligands present on the surface, the contact resistance at nanowire junctions can be effectively lowered. In addition, it appears that there is a diverse range of usable ligands that can be applied to AgNW films. The use of the correct ligands can create highly conductive 2D or 3D conductive structures for application in devices.

### 2.3 3D Conduction Composite Films as Pressure Sensor Materials

The combination of a conductive percolating 3D network within an elastic matrix gives rise to interesting piezoresistive behaviour. Such properties can be used to make elastic conducting films in pressure sensing applications.

### 2.3.1 Transduction Mechanisms

Pressure sensors can be broadly categorized based on several common transduction mechanisms: piezoelectric, capacitive and piezoresistive. Figure 2-4 briefly illustrates the differences among the three different mechanisms.

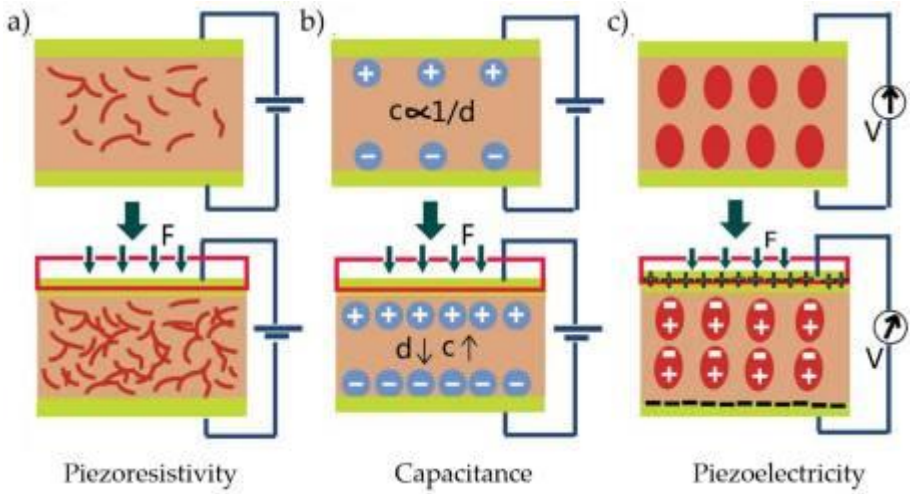



Figure 2-4: Schematic diagrams of 3 different types of pressure transduction mechanisms: (a) piezoresistivity, (b) capacitance and (c) piezoelectricity. Image taken from reference [99].

In piezoelectric sensors, an applied pressure on the sensor material induces a potential difference which can be detected. These sensors are sensitive, have fast response times and can potentially be self-powered.[100,101] However, the main disadvantage of piezoelectric sensors is that it can only detect dynamic changes in pressure as the generated potential difference decays after a while. The electronics involved in a sensor is also quite complex.[102] The capacitive sensors work based on parallel plate capacitors with two conducting electrodes separated by an elastic dielectric material. Pressure applied on the sensor decreases the distance between the electrodes and changes the capacitance of the sensor. These sensors have low energy consumption, fast response time and stable output but lack sensitivity due to the relatively small change in capacitance.[103] Organic thin film transistors are another form of capacitive sensor. The pressure applied on the transistor changes the

capacitance of the gate dielectric which alters the drain current. Such sensors can attain high sensitivities but the device structure is more complex and high power consumption is required.[104,105] Piezoresistive sensors work by changing the conductive pathways within a material when a pressure is applied onto it. These sensors can achieve high sensitivities and have simple device structures, but may suffer from hysteresis effects.[106] Table 2-1 compares the performances of reported pressure sensors with different transduction mechanisms. The units for sensitivity for piezoelectric sensors differ from that of capacitive and piezoresistive sensors as a voltage is output with pressure instead of relative changes in capacitance or resistance. Overall, piezoresistive sensors can easily achieve high sensitivities, making them suited for detecting small pressures.

Table 2-1: List of recently reported high performance flexible pressure sensors

| Materials | Transduction Mechanism | Maximum Sensitivity | Response Time (ms) | Measuring Range (Pa) | Ref |
|---|---|---|---|---|---|
| Perfluoro(alkoxy alkane) | Piezoelectric | 15 V $kPa^{-1}$ | - | < 2500 | [107] |
| Poly(vinylidenefluoride-co-trifluoroethylene) nanofibre | Piezoelectric | 1.1 V $kPa^{-1}$ | - | 100 – 2000 | [108] |
| PVDF nanofibre | Piezoelectric | 6.5 V $kPa^{-1}$ | 10 | 1000 – 8300 | [101] |
| Microstructured PDMS on organic thin film transistor | Capacitive | 8.4 $kPa^{-1}$ | < 10 | < 60000 | [104] |
| Poly(vinylidenefluoride-co-trifluoroethylene) nanofiber | Capacitive | 2.81 $kPa^{-1}$ | 42 | < 800 | [109] |
| Silver nanowire on PDMS with PVDF dielectric | Capacitive | 2.94 $kPa^{-1}$ | < 50 | < 7500 | [110] |
| Microstructured CNT/Graphene/PDMS | Piezoresistive | 19.8 $kPa^{-1}$ | < 16.7 | 0.6 – 300 | [111] |
| Graphene paper | Piezoresistive | 17.2 $kPa^{-1}$ | 60 | < 20000 | [112] |
| Microstructured PDMS + SnSe2 Nanoplates | Piezoresistive | 433.2 $kPa^{-1}$ | 0.09 | 0.82 - 38000 | [113] |
| Microstructured CNT/PDMS | Piezoresistive | 47000 $kPa^{-1}$ | 12 | < 26000 | [114] |

### 2.3.2 Piezoresistive Sensors

Traditional piezoresistive pressure sensors are based on silicon-based MEMS devices. Pressure is applied onto a silicon diaphragm and induces a change in resistivity which can be detected.[115] Despite the high sensitivities of these devices, they are not compatible with newer applications which require flexibility in the sensors.

The new generation of flexible piezoresistive sensors generally employ conductive composites as their active material. In a device, the composite film is either pressed against an electrode material or pressed against another composite film. Transduction can occur in two ways. The bulk resistivity of the film can change with applied pressure as it deforms the material and changes the percolative properties of the conductive network.[116] Alternatively, the contact resistance within the film can change too as it is known that contact resistance varies with square root of applied force. [117–119] Depending on the design of the pressure sensor material and setup, high sensitivity can be attained.

### 2.3.3 Achieving High Sensitivity

The sensitivity of a pressure sensor quantifies the ability of a sensor to transform applied pressure into measurable signals and can generally be expressed by[120]:

$$S = \frac{\Delta x / x_0}{\Delta P} \tag{2-6}$$

where $\Delta P$ is the applied pressure, $\Delta x$ is the change in the measured signal and $x_0$ is the original value of the signal in the absence of the applied pressure. For piezoresistive sensors, resistance or current can be used as $x$ as both resistance and current will change and can be measured when a pressure is applied.[114,121] In general, for sensors which experience decrease in resistance when pressure is applied, sensitivities measured using current will be larger

and vice versa. For the purpose of this thesis, the sensitivity derived from the change in resistance will be used since technically the resistance is the fundamental property that changes in piezoresistivity. The current strategies used to achieve high sensitivities in flexible piezoresistive pressure sensors will now be reviewed.

#### 2.3.3.1 Microstructured Surface

One prime strategy used to improve the sensitivity of pressure sensors by boosting the change in contact resistance is to create a patterned microstructure on the film's surface. Different types of microstructures such as microdomes[114,122], pyramids[123], pillars[124] and microgrooves[125] have been fabricated and successfully used to produce highly sensitive pressure sensing films. The microstructured side of the film is pressed against a flat electrode like indium-doped tin oxide (ITO). When a pressure is applied onto the sensor, the microstructures on the film become deformed. As a result, the surface area of contact between the film and the electrode increases with pressure as shown in Figure 2-5. This creates an additional decrease in resistance on top of the decrease in contact resistance purely due to the applied pressure.

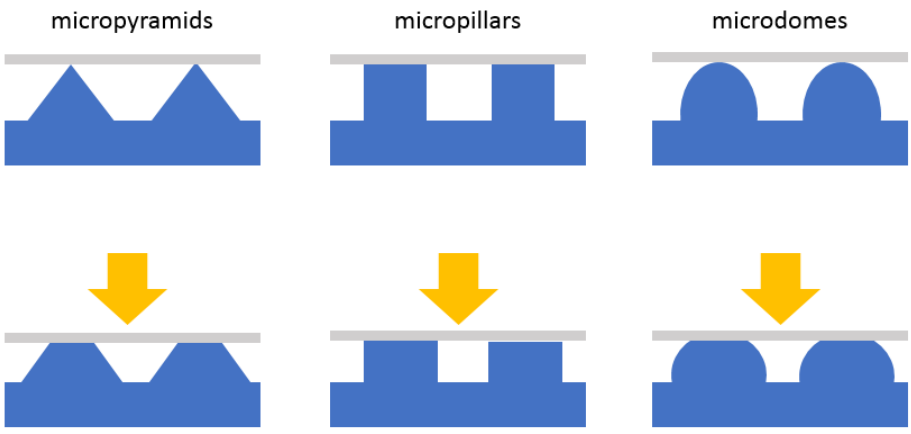



Figure 2-5: Schematic of different microstructures and their behaviour under applied pressure.

As an extension to this strategy, two pieces of microstructured films can be placed face to face to form an interlocking structure.[118,126] This further increases the changes in contact area between the two films when a pressure is applied. Park et al. investigated the differences in sensitivity in their carbon nanotube (CNT)/PDMS film when using a single microdome film and using an interlocked structure. They reported that the interlock structure achieved the highest sensitivity of 15.1 $kPa^{-1}$, compared to 5.4 $kPa^{-1}$ when only using a single microdome film. In comparison, a planar film only managed a sensitivity of 0.6 $kPa^{-1}$.[122] In a more recent publication, Park et al. reported an updated study of their interlocked microdome CNT/PDMS along with interlocked micropyramids and micropillar pressure sensors. All of the interlocked microstructures achieved very high sensitivities with the interlocked microdomes achieving the highest sensitivity of 47000 $kPa^{-1}$. This sensitivity is more than 1000 times higher than most reported pressure sensors. The extreme sensitivity allowed a low detection limit of 0.09 Pa.[114] Chen et al. used a similar concept which they call "rough-rough" interface to achieve high sensitivity.[127] A rough-rough interface was formed by the contact between 2 irregularly patterned films. Using the interface between a film of flower-shaped $SnSe_2$ nanoplates and a microstructured PDMS film, they achieved a high sensitivity of 433 $kPa^{-1}$.[113]

The microstructure in these films are typically made by molds which are fabricated via photolithography. To decrease the cost of making these patterned microstructures, simpler patterning techniques have been explored. Several studies have used more easily assessible objects as molds instead of having to fabricate them as an additional step. Examples of molds that have been used include leaves, silk and sandpaper.[111,128–130] Some notable results were reported by Su et al. using mimosa leaves and Wang et al. who used sandpaper to achieve excellent device sensitivities of 50.1 $kPa^{-1}$ and 851 $kPa^{-1}$. Other solutions involve

using lithographic free patterning techniques to create the microstructured patterns. Wang et al. used breath figure method to make a honeycomb polystyrene template for fabricating gold coated microdome films which when interlocked achieved high sensitivities of 197 $kPa^{-1}$.[131] One more notable strategy which is gaining popularity is to use wrinkled conductive films in the active material. This can be done by coating the conductive nanomaterial onto a pre-stretched substrate.[132,133] Residual stress in the nanomaterial film when the pre-stretch was released caused the film to buckle and become wrinkled. Another way is to add randomly aligned fibres as spacers to create an uneven surface in the conductive film.[134]

2.3.3.2 Conductive Sponges

The fabrication of conductive sponge-like materials is another key strategy for increasing the sensitivity of elastic conductive materials. This can be done by inducing bubbles or cavities into the conductive composite to form foams, gels or sponges. When the conductive sponge is compressed, the pores in the material collapse and create new conductive pathways within the sponge. This high surface area in the porous sponge ensures that there can be a large variation in contact area that would lead to an increased sensitivity.[102,135–137] Some notable results based on conductive sponge were reported by Lv et al. and Liu et al.[138,139] Lv et al. who used an egg beater to create bubbles in an aqueous graphene oxide dispersion which was then freeze-dried to preserve the porous structure and then annealed to obtain the final material. This graphene oxide sponge had high flexibility and achieved a sensitivity of 229.8 $kPa^{-1}$ and a low detection limit corresponding to approximately 13 mPa.[138] Liu et al. made an elastic carbon foam using a commercially available melamine foam and carbonizing it at high temperatures of 700-900 °C for 2 hours. The resultant foam achieved a sensitivity of 100.29 $kPa^{-1}$ with a low detection limit of 3 Pa.[139]

Overall, these methods of fabricating highly sensitive piezoresistive pressure sensors are effective but involve additional processing steps. The use of natural molds instead of photolithography methods alleviates the problem but still has relatively low throughput as molding is generally a batch process. In addition, some natural molds like leaves are small in size which further limits the rate of processing and the dimensions of the sensor films. As for the use of conductive sponges, similar throughput issues exist. Furthermore, to create the porous structure, freeze-drying and subsequent annealing at high temperatures are usually required. Such processing steps require high amounts of energy. The final sponge structure is also quite thick compared to most piezoresistive films. It would be beneficial to use simpler processing methods such as non-contact printing to produce high sensitivity pressure sensing films.

### 2.3.4 Silver Nanowire Composite Films as Pressure Sensors

As reviewed in the previous sections, most piezoresistive pressure sensors make use of carbon-based conductors as the conductive fillers in the composite films. In addition, many of the highest performing sensors are CNT or graphene-based devices. However, there is an inherent trade-off between high sensitivity and device complexity. The high sensitivity from carbon nanomaterials is due to their overall poor film conductivities ($< 10^{-5}$ S/m) arising from high contact resistance between the fillers.[140] Therefore, either high voltage sources or sophisticated measuring devices have to be used with these types of sensors. For example, the ultrahigh sensitivity interlocking microdome sensor developed by Park et al. is realistically an insulator with resistances in the giga-ohm range when no pressure is applied. For the sensor to function within the high sensitivity regime, either the measurement devices must have sufficient resolution to measure currents in the nano- to micro-ampere range accurately or the sensor should be used with input voltages in the range of kilovolts. This is

impractical for applications in health monitoring and wearable devices. In this aspect, AgNWs have the advantage of being able to form more conductive composite films so that pressure sensing can be done more easily.

Currently, metallic nanowires have found limited use in piezoresistive pressure sensing applications. Only several studies by Wei et al., Zhong et al. and Ko et al. have reported high sensitivities of 16.1, 19.4 and 69.7 $kPa^{-1}$ respectively.[141–143] Majority of nanowire pressure sensors only managed sensitivities below 5 $kPa^{-1}$.[144–149] However, they are widely use in high performance strain gauges.[140,150–153] Strain gauges are devices which measure strain rather than pressure and can also work using piezoresistive materials. Unlike pressure sensors, strain gauges work based on tension instead of compression. Applied tensile strain stretches the composite film which reduces its bulk resistivity due to the disruption to the percolation in the composite. Through tailoring film composition, high strain sensing sensitivity can be achieved by AgNW composite films. If the same mechanism can be applied in pressure sensing, AgNWs can potentially be made into highly sensitive pressure sensors while having high conductivities.

## 2.4 Conclusion and Prospects

In conclusion, this chapter reviewed the developments and strategies involved in high resolution printing techniques. In particular, I am interested in printing of AgNWs for fabricating composite films which can be used to make highly sensitive piezoresistive pressure sensors.

For printing high resolution features, it is important to control the ink footprint from the printer and degree of spreading on the substrate. Currently, EHD and aerosol printing

present strategies to control ink footprint with the aid of electrostatic forces and air pressure. Although these two methods have been successful in their application, it would be beneficial to explore the use of alternative forces to achieve the same goal.

The wettability of ink on the substrate is controlled by the interaction between the ink substrate and surrounding medium. Strategies to tune the ink surface tension and substrate surface energy have been attempted with some degree of success. In this aspect, the change in the surrounding medium is one factor which has yet to be explored and can be potentially useful. Pre-patterning of the substrate to constrain areas for preferential ink wetting to occur is by far the most effective strategy to increase resolution of regular inkjet printing. However, this often adds complexity to the printing process and is not desirable.

For printing AgNWs with high conductivity, the main obstacle is to overcome the high contact resistance at nanowire junctions due to the presence of insulating ligands on their surface. The removal of the ligands is often done effectively by various post-treatments. The use of chemical treatments is a method which is both effective and easy to perform. However, it would be ideal if conductive features can be printed without the need for post-treatments. Current treatment-free inks largely involve modifying the surface ligands on the nanowires. This highlights the importance of surface ligand structure on the conductivity of the final printed features.

Lastly, the strategies for producing highly sensitive piezoresistive pressure sensors were reviewed. The strategy largely involves creating microstructures in the composite films to increase the possible variations in resistance. However, these microstructures require the use of molds or additional steps to fabricate. By adapting the sensing mechanism in strain

gauges for pressure sensors, there is potential for the fabrication of printed and highly sensitive AgNW pressure sensors.

## 2.5 References


1. Fukuda, K. & Someya, T. Recent Progress in the Development of Printed Thin-Film Transistors and Circuits with High-Resolution Printing Technology. *Adv. Mater.* **29**, (2017).
2. Waasdorp, R., Van Den Heuvel, O., Versluis, F., Hajee, B. & Ghatkesar, M. K. Accessing individual 75-micron diameter nozzles of a desktop inkjet printer to dispense picoliter droplets on demand. *RSC Adv.* **8**, 14765–14774 (2018).
3. Ru, C., Luo, J., Xie, S. & Sun, Y. A review of non-contact micro- and nano-printing technologies. *J. Micromechanics Microengineering* **24**, (2014).
4. Derby, B. Inkjet Printing of Functional and Structural Materials: Fluid Property Requirements, Feature Stability, and Resolution. *Annu. Rev. Mater. Res.* **40**, 395–414 (2010).
5. Gao, M., Li, L. & Song, Y. Inkjet printing wearable electronic devices. *J. Mater. Chem. C* **5**, 2971–2993 (2017).
6. Raut, N. C. & Al-Shamery, K. Inkjet printing metals on flexible materials for plastic and paper electronics. *J. Mater. Chem. C* **6**, 1618–1641 (2018).
7. Liu, Y. & Derby, B. Experimental study of the parameters for stable drop-on-demand inkjet performance. *Phys. Fluids* **31**, (2019).
8. Wang, F. *et al.* Exploring pulse-voltage-triggered optically induced electrohydrodynamic instability for femtolitre droplet generation. *Appl. Phys. Lett.* **104**, (2014).
9. Onses, M. S., Sutanto, E., Ferreira, P. M., Alleyne, A. G. & Rogers, J. A. Mechanisms, Capabilities, and Applications of High-Resolution Electrohydrodynamic Jet Printing. *Small* **11**, 4237–4266 (2015).
10. Lee, J. *et al.* Improved electrochromic device performance from silver grid on flexible transparent conducting electrode prepared by electrohydrodynamic jet printing. *J. Mater. Chem. C* **5**, 12800–12806 (2017).
11. Kim, S. Y. *et al.* High-resolution electrohydrodynamic inkjet printing of stretchable metal oxide semiconductor transistors with high performance. *Nanoscale* **8**, 17113–17121 (2016).
12. Min, S. Y., Lee, Y., Kim, S. H., Park, C. & Lee, T. W. Room-Temperature-Processable Wire-Templated Nanoelectrodes for Flexible and Transparent All-Wire Electronics. *ACS Nano* **11**, 3681–3689 (2017).
13. Lee, Y. *et al.* Versatile Metal Nanowiring Platform for Large-Scale Nano- and

Opto-Electronic Devices. *Adv. Mater.* **28**, 9109–9116 (2016).

14. Galliker, P. *et al.* Direct printing of nanostructures by electrostatic autofocussing of ink nanodroplets. *Nat. Commun.* **3**, 890–899 (2012).
15. Kamyshny, A. & Magdassi, S. Conductive nanomaterials for 2D and 3D printed flexible electronics. *Chem. Soc. Rev.* **48**, 1712–1740 (2019).
16. Lee, H., Seong, B., Kim, J., Jang, Y. & Byun, D. Direct alignment and patterning of silver nanowires by electrohydrodynamic jet printing. *Small* **10**, 3918–3922 (2014).
17. Cui, Z., Han, Y., Huang, Q., Dong, J. & Zhu, Y. Electrohydrodynamic printing of silver nanowires for flexible and stretchable electronics. *Nanoscale* **10**, 6806–6811 (2018).
18. Park, S. H. *et al.* Optimization of electrohydrodynamic-printed organic electrodes for bottom-contact organic thin film transistors. *Org. Electron. physics, Mater. Appl.* **38**, 48–54 (2016).
19. Chang, J., He, J., Lei, Q. & Li, D. Electrohydrodynamic Printing of Microscale PEDOT:PSS-PEO Features with Tunable Conductive/Thermal Properties. *ACS Appl. Mater. Interfaces* **10**, 19116–19122 (2018).
20. Mahajan, A., Frisbie, C. D. & Francis, L. F. Optimization of aerosol jet printing for high-resolution, high-aspect ratio silver lines. *ACS Appl. Mater. Interfaces* **5**, 4856–4864 (2013).
21. Oakley, C. & Chahal, P. Aerosol Jet Printed Quasi-Optical Terahertz Components. *IEEE Trans. Terahertz Sci. Technol.* **8**, 765–772 (2018).
22. Jahn, D. *et al.* Digital Aerosol Jet Printing for the Fabrication of Terahertz Metamaterials. *Adv. Mater. Technol.* **3**, (2018).
23. Secor, E. B. Principles of aerosol jet printing. *Flex. Print. Electron.* **3**, (2018).
24. Wilkinson, N. J., Smith, M. A. A., Kay, R. W. & Harris, R. A. A review of aerosol jet printing—a non-traditional hybrid process for micro-manufacturing. *Int. J. Adv. Manuf. Technol.* (2019). doi:10.1007/s00170-019-03438-2
25. Nguyen, H. A. D., Lee, J., Kim, C. H., Shin, K. H. & Lee, D. An approach for controlling printed line-width in high resolution roll-to-roll gravure printing. *J. Micromechanics Microengineering* **23**, (2013).
26. Young, T. An essay on the cohesion of fluids. *Philos. Trans. R. Soc. London* **95**, 65–87 (1805).
27. Lessing, J. *et al.* Inkjet printing of conductive inks with high lateral resolution on omniphobic ‘rF paper’ for paper-based electronics and MEMS. *Adv. Mater.* **26**,

4677–4682 (2014).

28. Kim, C., Nogi, M., Suganuma, K. & Yamato, Y. Inkjet-printed lines with well-defined morphologies and low electrical resistance on repellent pore-structured polyimide films. *ACS Appl. Mater. Interfaces* **4**, 2168–2173 (2012).
29. Duineveld, P. C. The stability of ink-jet printed lines of liquid with zero receding contact angle on a homogeneous substrate. *J. Fluid Mech.* **477**, 175–200 (2003).
30. Suzuki, K. *et al.* Fabrication of All-printed Organic TFT Array on Flexible Substrate. *J. Photopolym. Sci. Technol.* **24**, 565–570 (2011).
31. Nguyen, P. Q. M., Yeo, L. P., Lok, B. K. & Lam, Y. C. Patterned surface with controllable wettability for inkjet printing of flexible printed electronics. *ACS Appl. Mater. Interfaces* **6**, 4011–4016 (2014).
32. Wu, L. *et al.* Printing patterned fine 3D structures by manipulating the three phase contact line. *Adv. Funct. Mater.* **25**, 2237–2242 (2015).
33. Mahajan, A. *et al.* High-resolution, high-aspect ratio conductive wires embedded in plastic substrates. *ACS Appl. Mater. Interfaces* **7**, 1841–1847 (2015).
34. Song, D. *et al.* All-Printed, Self-Aligned Carbon Nanotube Thin-Film Transistors on Imprinted Plastic Substrates. *ACS Appl. Mater. Interfaces* **10**, 15926–15932 (2018).
35. Sun, Y., Mayers, B., Herricks, T. & Xia, Y. Polyol synthesis of uniform silver nanowires: A plausible growth mechanism and the supporting evidence. *Nano Lett.* **3**, 955–960 (2003).
36. Coskun, S., Aksoy, B. & Unalan, H. E. Polyol Synthesis of Silver Nanowires: An Extensive Parametric Study. *Cryst. Growth Des.* **11**, 4963–4969 (2011).
37. Stauffer, D. & Aharony, A. *Introduction To Percolation Theory*. (Taylor & Francis, 1992). doi:10.1201/9781315274386
38. Mutiso, R. M. & Winey, K. I. Electrical properties of polymer nanocomposites containing rod-like nanofillers. *Prog. Polym. Sci.* **40**, 63–84 (2015).
39. Foygel, M., Morris, R. D., Anez, D., French, S. & Sobolev, V. L. Theoretical and computational studies of carbon nanotube composites and suspensions: Electrical and thermal conductivity. *Phys. Rev. B - Condens. Matter Mater. Phys.* **71**, 1–8 (2005).
40. Li, J. & Zhang, S. L. Finite-size scaling in stick percolation. *Phys. Rev. E - Stat. Nonlinear, Soft Matter Phys.* **80**, 1–4 (2009).
41. Garboczi, E. J., Snyder, K. A., Douglas, J. F. & Thorpe, M. F. Geometrical

percolation threshold of overlapping ellipsoids. *Phys. Rev. E* **52**, 819–828 (1995).

42. Johner, N., Grimaldi, C., Balberg, I. & Ryser, P. Transport exponent in a three-dimensional continuum tunneling-percolation model. *Phys. Rev. B - Condens. Matter Mater. Phys.* **77**, 1–11 (2008).
43. Grimaldi, C. & Balberg, I. Tunneling and nonuniversality in continuum percolation systems. *Phys. Rev. Lett.* **96**, 15–18 (2006).
44. Bauhofer, W. & Kovacs, J. Z. A review and analysis of electrical percolation in carbon nanotube polymer composites. *Compos. Sci. Technol.* **69**, 1486–1498 (2009).
45. Keblinski, P. & Cleri, F. Contact resistance in percolating networks. *Phys. Rev. B - Condens. Matter Mater. Phys.* **69**, 1–4 (2004).
46. Žeželj, M. & Stanković, I. From percolating to dense random stick networks: Conductivity model investigation. *Phys. Rev. B* **86**, 134202 (2012).
47. Mutiso, R. M., Sherrott, M. C., Rathmell, A. R., Wiley, B. J. & Winey, K. I. Integrating simulations and experiments to predict sheet resistance and optical transmittance in nanowire films for transparent conductors. *ACS Nano* **7**, 7654–7663 (2013).
48. Zabet-Khosousi, A. & Dhirani, A. A. Charge transport in nanoparticle assemblies. *Chem. Rev.* **108**, 4072–4124 (2008).
49. Hwang, J., Shim, Y., Yoon, S. M., Lee, S. H. & Park, S. H. Influence of polyvinylpyrrolidone (PVP) capping layer on silver nanowire networks: Theoretical and experimental studies. *RSC Adv.* **6**, 30972–30977 (2016).
50. Wuelfing, W. P. & Murray, R. W. Electron hopping through films of arenethiolate monolayer-protected gold clusters. *J. Phys. Chem. B* **106**, 3139–3145 (2002).
51. Hybertsen, M. S. *et al.* Amine-linked single-molecule circuits: Systematic trends across molecular families. *J. Phys. Condens. Matter* **20**, (2008).
52. Song, T. Bin *et al.* Nanoscale joule heating and electromigration enhanced ripening of silver nanowire contacts. *ACS Nano* **8**, 2804–2811 (2014).
53. Garnett, E. C. *et al.* Self-limited plasmonic welding of silver nanowire junctions. *Nat. Mater.* **11**, 241–249 (2012).
54. Nanowire, S. *et al.* Scalable Coating and Properties of. *ACS Nano* **4**, 2955–2963 (2010).
55. Huang, Q., Lilley, C. M. & Bode, M. Surface scattering effect on the electrical resistivity of single crystalline silver nanowires self-assembled on vicinal Si (001).

*Appl. Phys. Lett.* **95**, 10–13 (2009).

56. Chen, W. *et al.* Aromaticity decreases single-molecule junction conductance. *J. Am. Chem. Soc.* **136**, 918–920 (2014).
57. Selzer, F. *et al.* Electrical limit of silver nanowire electrodes: Direct measurement of the nanowire junction resistance. *Appl. Phys. Lett.* **108**, (2016).
58. Langley, D. P. *et al.* Metallic nanowire networks: Effects of thermal annealing on electrical resistance. *Nanoscale* **6**, 13535–13543 (2014).
59. Hwang, B., Shin, H. A. S., Kim, T., Joo, Y. C. & Han, S. M. Highly reliable Ag nanowire flexible transparent electrode with mechanically welded junctions. *Small* **10**, 3397–3404 (2014).
60. Coskun, S., Selen Ates, E. & Emrah Unalan, H. Optimization of silver nanowire networks for polymer light emitting diode electrodes. *Nanotechnology* **24**, (2013).
61. Bellew, A. T., Manning, H. G., Gomes da Rocha, C., Ferreira, M. S. & Boland, J. J. Resistance of Single Ag Nanowire Junctions and Their Role in the Conductivity of Nanowire Networks. *ACS Nano* **9**, 11422–11429 (2015).
62. Perelaer, J., Klokkenburg, M., Hendriks, C. E. & Schubert, U. S. Microwave flash sintering of inkjet-printed silver tracks on polymer substrates. *Adv. Mater.* **21**, 4830–4834 (2009).
63. Fujii, S. *et al.* Microwave sintering of Ag-nanoparticle thin films on a polyimide substrate. *AIP Adv.* **5**, (2015).
64. Jung, P. H., Kim, Y. D., Sung, Y. H. & Lee, H. Microwave welding of silver nanowires for highly transparent conductive electrodes. *Phys. Status Solidi Appl. Mater. Sci.* **214**, (2017).
65. Allen, M. L. *et al.* Electrical sintering of nanoparticle structures. *Nanotechnology* **19**, (2008).
66. Allen, M. *et al.* Contactless electrical sintering of silver nanoparticles on flexible substrates. *IEEE Trans. Microw. Theory Tech.* **59**, 1419–1429 (2011).
67. Werner, C., Godlinski, D., Zöllmer, V. & Busse, M. Morphological influences on the electrical sintering process of Aerosol Jet and Ink Jet printed silver microstructures. *J. Mater. Sci. Mater. Electron.* **24**, 4367–4377 (2013).
68. Albrecht, A., Rivadeneyra, A., Abdellah, A., Lugli, P. & Salmerón, J. F. Inkjet printing and photonic sintering of silver and copper oxide nanoparticles for ultra-low-cost conductive patterns. *J. Mater. Chem. C* **4**, 3546–3554 (2016).
69. Dexter, M. *et al.* Modeling nanoscale temperature gradients and conductivity

evolution in pulsed light sintering of silver nanowire networks. *Nanotechnology* **29**, (2018).

70. Balliu, E. *et al.* Selective laser sintering of inkjet-printed silver nanoparticle inks on paper substrates to achieve highly conductive patterns. *Sci. Rep.* **8**, 2–10 (2018).
71. Spechler, J. A., Nagamatsu, K. A., Sturm, J. C. & Arnold, C. B. Improved efficiency of hybrid organic photovoltaics by pulsed laser sintering of silver nanowire network transparent electrode. *ACS Appl. Mater. Interfaces* **7**, 10556–10562 (2015).
72. Lee, H. *et al.* Large-area compatible laser sintering schemes with a spatially extended focused beam. *Micromachines* **8**, 1–8 (2017).
73. Oghbaei, M. & Mirzaee, O. Microwave versus conventional sintering: A review of fundamentals, advantages and applications. *J. Alloys Compd.* **494**, 175–189 (2010).
74. Zhu, S. *et al.* Transferable self-welding silver nanowire network as high performance transparent flexible electrode. *Nanotechnology* **24**, (2013).
75. Wang, R. *et al.* Plasma-induced nanowelding of a copper nanowire network and its application in transparent electrodes and stretchable conductors. *Nano Res.* **9**, 2138–2148 (2016).
76. Li, J. *et al.* A flexible plasma-treated silver-nanowire electrode for organic light-emitting devices. *Sci. Rep.* **7**, 1–9 (2017).
77. Wang, S., Tian, Y., Hang, C. & Wang, C. Cohesively enhanced electrical conductivity and thermal stability of silver nanowire networks by nickel ion bridge joining. *Sci. Rep.* **8**, 1–9 (2018).
78. Kang, H. *et al.* Epitaxial-Growth-Induced Junction Welding of Silver Nanowire Network Electrodes. *ACS Nano* **12**, 4894–4902 (2018).
79. Zhang, L. *et al.* Highly thermal-stable and transparent silver nanowire conductive films via magnetic assisted electrodeposition of Ni. *J. Mater. Chem. C* **6**, 4887–4894 (2018).
80. Lu, H. *et al.* Locally Welded Silver Nano-Network Transparent Electrodes with High Operational Stability by a Simple Alcohol-Based Chemical Approach. *Adv. Funct. Mater.* **25**, 4211–4218 (2015).
81. Coutts, M. J., Cortie, M. B., Ford, M. J. & McDonagh, A. M. Rapid and controllable sintering of gold nanoparticle inks at room temperature using a chemical agent. *J. Phys. Chem. C* **113**, 1325–1328 (2009).
82. Yoon, S. S. & Khang, D. Y. Room-Temperature Chemical Welding and Sintering

of Metallic Nanostructures by Capillary Condensation. *Nano Lett.* **16**, 3550–3556 (2016).

83. Hui, Z. *et al.* Chemical sintering of direct-written silver nanowire flexible electrodes under room temperature. *Nanotechnology* **28**, (2017).
84. Kang, H., Kim, Y., Cheon, S., Yi, G. R. & Cho, J. H. Halide Welding for Silver Nanowire Network Electrode. *ACS Appl. Mater. Interfaces* **9**, 30779–30785 (2017).
85. Layani, M. & Magdassi, S. Flexible transparent conductive coatings by combining self-assembly with sintering of silver nanoparticles performed at room temperature. *J. Mater. Chem.* **21**, 15378–15382 (2011).
86. Layani, M., Grouchko, M., Shemesh, S. & Magdassi, S. Conductive patterns on plastic substrates by sequential inkjet printing of silver nanoparticles and electrolyte sintering solutions. *J. Mater. Chem.* **22**, 14349–14352 (2012).
87. Lee, S.-W. *et al.* Engineering surface ligands of nanocrystals to design high performance strain sensor arrays through solution processes. *J. Mater. Chem. C* **5**, 2442–2450 (2017).
88. Seong, M. *et al.* Designing highly conductive and stable silver nanocrystal thin films with tunable work functions through solution-based surface engineering with gold coating process. *J. Alloys Compd.* **698**, 400–409 (2017).
89. Song, Y. *et al.* Room-Temperature Metallic Fusion-Induced Layer-by-Layer Assembly for Highly Flexible Electrode Applications. *Adv. Funct. Mater.* **1806584**, 1–12 (2019).
90. Stansfield, G. L. & Thomas, P. J. Substituent effects on charge transport in films of Au nanocrystals. *J. Am. Chem. Soc.* **134**, 11888–11891 (2012).
91. Amoli, B. M., Gumfekar, S., Hu, A., Zhou, Y. N. & Zhao, B. Thiocarboxylate functionalization of silver nanoparticles: Effect of chain length on the electrical conductivity of nanoparticles and their polymer composites. *J. Mater. Chem.* **22**, 20048–20056 (2012).
92. Lee, Y. J., Kim, N. R., Lee, C. & Lee, H. M. Uniform thin film electrode made of low-temperature-sinterable silver nanoparticles: optimized extent of ligand exchange from oleylamine to acrylic acid. *J. Nanoparticle Res.* **19**, (2017).
93. Jung, I., Shin, K., Kim, N. R. & Lee, H. M. Synthesis of low-temperature-processable and highly conductive Ag ink by a simple ligand modification: The role of adsorption energy. *J. Mater. Chem. C* **1**, 1855–1862 (2013).
94. Wang, J. *et al.* Silver nanowire electrodes: Conductivity improvement without post-

treatment and application in capacitive pressure sensors. *Nano-Micro Lett.* **7**, 51–58 (2014).

95. Grouchko, M., Kamyshny, A., Mihailescu, C. F., Anghel, D. F. & Magdassi, S. Conductive inks with a 'built-in' mechanism that enables sintering at room temperature. *ACS Nano* **5**, 3354–3359 (2011).
96. Reiser, B., González-García, L., Kanelidis, I., Maurer, J. H. M. & Kraus, T. Gold nanorods with conjugated polymer ligands: Sintering-free conductive inks for printed electronics. *Chem. Sci.* **7**, 4190–4196 (2016).
97. Su, Q., Xue, T., Zhang, Y., Lan, K. & Zou, Q. Fabrication of enhanced silver nanowire films via self-assembled gold nanoparticles without post-treatment. *Mater. Lett.* **236**, 218–221 (2019).
98. Mol Menamparambath, M. *et al.* Silver nanowires decorated with silver nanoparticles for low-haze flexible transparent conductive films. *Sci. Rep.* **5**, 1–9 (2015).
99. Li, L. *et al.* Recent Developments for Flexible Pressure Sensors: A Review. *Micromachines* **9**, 580 (2018).
100. Chen, X. *et al.* High-Performance Piezoelectric Nanogenerators with Imprinted P(VDF-TrFE)/BaTiO3 Nanocomposite Micropillars for Self-Powered Flexible Sensors. *Small* **13**, 1–12 (2017).
101. Maity, K. & Mandal, D. All-Organic High-Performance Piezoelectric Nanogenerator with Multilayer Assembled Electrospun Nanofiber Mats for Self-Powered Multifunctional Sensors. *ACS Appl. Mater. Interfaces* **10**, 18257–18269 (2018).
102. Ding, Y., Xu, T., Onyilagha, O., Fong, H. & Zhu, Z. Recent advances in flexible and wearable pressure sensors based on piezoresistive 3D monolithic conductive sponges. *ACS Appl. Mater. Interfaces* **11**, 6685–6704 (2019).
103. Zang, Y., Zhang, F., Di, C. A. & Zhu, D. Advances of flexible pressure sensors toward artificial intelligence and health care applications. *Mater. Horizons* **2**, 140–156 (2015).
104. Schwartz, G. *et al.* Flexible polymer transistors with high pressure sensitivity for application in electronic skin and health monitoring. *Nat. Commun.* **4**, 1858–1859 (2013).
105. Zang, Y. *et al.* Flexible suspended gate organic thin-film transistors for ultra-sensitive pressure detection. *Nat. Commun.* **6**, 1–9 (2015).

106. Li, J., Bao, R., Tao, J., Peng, Y. & Pan, C. Recent progress in flexible pressure sensor arrays: From design to applications. *J. Mater. Chem. C* **6**, 11878–11892 (2018).
107. Wu, N. *et al.* Theoretical study and structural optimization of a flexible piezoelectret-based pressure sensor. *J. Mater. Chem. A* **6**, 5065–5070 (2018).
108. Persano, L. *et al.* High performance piezoelectric devices based on aligned arrays of nanofibers of poly(vinylidenefluoride-co-trifluoroethylene). *Nat. Commun.* **4**, 1610–1633 (2013).
109. Kim, Y., Jang, S., Kang, B. J. & Oh, J. H. Fabrication of highly sensitive capacitive pressure sensors with electrospun polymer nanofibers. *Appl. Phys. Lett.* **111**, (2017).
110. Shuai, X. *et al.* Highly Sensitive Flexible Pressure Sensor Based on Silver Nanowires-Embedded Polydimethylsiloxane Electrode with Microarray Structure. *ACS Appl. Mater. Interfaces* **9**, 26314–26324 (2017).
111. Jian, M. *et al.* Flexible and Highly Sensitive Pressure Sensors Based on Bionic Hierarchical Structures. *Adv. Funct. Mater.* **27**, (2017).
112. Tao, L. Q. *et al.* Graphene-Paper Pressure Sensor for Detecting Human Motions. *ACS Nano* **11**, 8790–8795 (2017).
113. Li, W. *et al.* Flexible and High Performance Piezoresistive Pressure Sensors Based on Hierarchical Flower-Shaped SnSe 2 Nanoplates. *ACS Appl. Energy Mater.* **2**, 2803–2809 (2019).
114. Park, J. *et al.* Tailoring force sensitivity and selectivity by microstructure engineering of multidirectional electronic skins. *NPG Asia Mater.* **10**, 163–176 (2018).
115. Kumar, S. S. & Pant, B. D. Design principles and considerations for the 'ideal' silicon piezoresistive pressure sensor: A focused review. *Microsyst. Technol.* **20**, 1213–1247 (2014).
116. Lee, D. *et al.* Highly Sensitive, Transparent, and Durable Pressure Sensors Based on Sea-Urchin Shaped Metal Nanoparticles. *Adv. Mater.* **28**, 9364–9369 (2016).
117. Yang, C. *et al.* Highly Sensitive Wearable Pressure Sensors Based on Three-Scale Nested Wrinkling Microstructures of Polypyrrole Films. *ACS Appl. Mater. Interfaces* **10**, 25811–25818 (2018).
118. Yin, F., Yang, J., Peng, H. & Yuan, W. Flexible and highly sensitive artificial electronic skin based on graphene/polyamide interlocking fabric. *J. Mater. Chem. C*

**6**, 6840–6846 (2018).

119. Wang, X. *et al.* Recent Progress in Electronic Skin. *Adv. Sci.* **2**, 1–21 (2015).
120. Huang, Y., Fan, X., Chen, S. C. & Zhao, N. Emerging Technologies of Flexible Pressure Sensors: Materials, Modeling, Devices, and Manufacturing. *Adv. Funct. Mater.* **29**, 1–24 (2019).
121. Lou, C. *et al.* A graphene-based flexible pressure sensor with applications to plantar pressure measurement and gait analysis. *Materials (Basel).* **10**, (2017).
122. Park, J. *et al.* Giant tunneling piezoresistance of composite elastomers with interlocked microdome arrays for ultrasensitive and multimodal electronic skins. *ACS Nano* **8**, 4689–4697 (2014).
123. Choong, C. L. *et al.* Highly stretchable resistive pressure sensors using a conductive elastomeric composite on a micropyramid array. *Adv. Mater.* **26**, 3451–3458 (2014).
124. Zhong, W. *et al.* A nanofiber based artificial electronic skin with high pressure sensitivity and 3D conformability. *Nanoscale* **8**, 12105–12112 (2016).
125. Pan, L. *et al.* An ultra-sensitive resistive pressure sensor based on hollow-sphere microstructure induced elasticity in conducting polymer film. *Nat. Commun.* **5**, 1–8 (2014).
126. Khalili, N., Shen, X. & Naguib, H. E. An interlocked flexible piezoresistive sensor with 3D micropyramidal structures for electronic skin applications. *Soft Matter* **14**, 6912–6920 (2018).
127. Chen, M. *et al.* Touchpoint-Tailored Ultrasensitive Piezoresistive Pressure Sensors with a Broad Dynamic Response Range and Low Detection Limit. *ACS Appl. Mater. Interfaces* **11**, 2551–2558 (2019).
128. Su, B., Gong, S., Ma, Z., Yap, L. W. & Cheng, W. Mimosa-inspired design of a flexible pressure sensor with touch sensitivity. *Small* **11**, 1886–1891 (2015).
129. Wang, X., Gu, Y., Xiong, Z., Cui, Z. & Zhang, T. Silk-molded flexible, ultrasensitive, and highly stable electronic skin for monitoring human physiological signals. *Adv. Mater.* **26**, 1336–1342 (2014).
130. Wang, Z. *et al.* High Sensitivity, Wearable, Piezoresistive Pressure Sensors Based on Irregular Microhump Structures and Its Applications in Body Motion Sensing. *Small* **12**, 3827–3836 (2016).
131. Wang, Z., Zhang, L., Liu, J., Jiang, H. & Li, C. Flexible hemispheric microarrays of highly pressure-sensitive sensors based on breath figure method. *Nanoscale* **10**,

10691–10698 (2018).

132. Wei, Y., Chen, S., Yuan, X., Wang, P. & Liu, L. Multiscale Wrinkled Microstructures for Piezoresistive Fibers. *Adv. Funct. Mater.* **26**, 5078–5085 (2016).

133. Jia, J., Huang, G., Deng, J. & Pan, K. Skin-inspired flexible and high-sensitivity pressure sensors based on rGO films with continuous-gradient wrinkles. *Nanoscale* **11**, 4258–4266 (2019).

134. Luo, C. *et al.* A new approach for ultrahigh-performance piezoresistive sensor based on wrinkled PPy film with electrospun PVA nanowires as spacer. *Nano Energy* **41**, 527–534 (2017).

135. Chun, S., Hong, A., Choi, Y., Ha, C. & Park, W. A tactile sensor using a conductive graphene-sponge composite. *Nanoscale* **8**, 9185–9192 (2016).

136. Si, Y. *et al.* Ultralight Biomass-Derived Carbonaceous Nanofibrous Aerogels with Superelasticity and High Pressure-Sensitivity. *Adv. Mater.* **28**, 9512–9518 (2016).

137. Zang, X. *et al.* Unprecedented sensitivity towards pressure enabled by graphene foam. *Nanoscale* **9**, 19346–19352 (2017).

138. Lv, L., Zhang, P., Xu, T. & Qu, L. Ultrasensitive Pressure Sensor Based on an Ultralight Sparkling Graphene Block. *ACS Appl. Mater. Interfaces* **9**, 22885–22892 (2017).

139. Liu, W. *et al.* A flexible and highly sensitive pressure sensor based on elastic carbon foam. *J. Mater. Chem. C* **6**, 1451–1458 (2018).

140. Boland, C. S., Khan, U., Benameur, H. & Coleman, J. N. Surface coatings of silver nanowires lead to effective, high conductivity, high-strain, ultrathin sensors. *Nanoscale* **9**, 18507–18515 (2017).

141. Jeong, H., Noh, Y., Ko, S. H. & Lee, D. Flexible resistive pressure sensor with silver nanowire networks embedded in polymer using natural formation of air gap. *Compos. Sci. Technol.* **174**, 50–57 (2019).

142. Zhong, W. *et al.* Ultrasensitive Wearable Pressure Sensors Assembled by Surface-Patterned Polyolefin Elastomer Nanofiber Membrane Interpenetrated with Silver Nanowires. *ACS Appl. Mater. Interfaces* **10**, 42706–42714 (2018).

143. Ko, Y., Kim, D., Kwon, G. & You, J. High-Performance Resistive Pressure Sensor Based on Elastic Composite Hydrogel of Silver Nanowires and Poly(ethylene glycol). *Micromachines* **9**, 438 (2018).

144. Wei, Y., Chen, S., Lin, Y., Yuan, X. & Liu, L. Silver nanowires coated on cotton

for flexible pressure sensors. *J. Mater. Chem. C* **4**, 935–943 (2016).

145. Xu, X. *et al.* Copper Nanowire-Based Aerogel with Tunable Pore Structure and Its Application as Flexible Pressure Sensor. *ACS Appl. Mater. Interfaces* **9**, 14273–14280 (2017).
146. Cheng, W. *et al.* A wearable and highly sensitive pressure sensor with ultrathin gold nanowires. *Nat. Commun.* **5**, 1–8 (2014).
147. He, W. *et al.* Polypyrrole/silver coaxial nanowire aero-sponges for temperature-independent stress sensing and stress-triggered joule heating. *ACS Nano* **9**, 4244–4251 (2015).
148. Dong, X. *et al.* A linear and large-range pressure sensor based on a graphene/silver nanowires nanobiocomposites network and a hierarchical structural sponge. *Compos. Sci. Technol.* **155**, 108–116 (2018).
149. Cao, M. *et al.* Wearable rGO-Ag NW@cotton fiber piezoresistive sensor based on the fast charge transport channel provided by Ag nanowire. *Nano Energy* **50**, 528–535 (2018).
150. Amjadi, M., Pichitpajongkit, A., Lee, S., Ryu, S. & Park, I. Highly stretchable and sensitive strain sensor based on silver nanowire-elastomer nanocomposite. *ACS Nano* **8**, 5154–5163 (2014).
151. Martinez, V. *et al.* Stretchable Silver Nanowire-Elastomer Composite Microelectrodes with Tailored Electrical Properties. *ACS Appl. Mater. Interfaces* **7**, 13467–13475 (2015).
152. Heo, Y., Hwang, Y., Jung, H. S., Choa, S. H. & Ko, H. C. Secondary Sensitivity Control of Silver-Nanowire-Based Resistive-Type Strain Sensors by Geometric Modulation of the Elastomer Substrate. *Small* **13**, 1–8 (2017).
153. Cao, Z., Wang, R., He, T., Xu, F. & Sun, J. Interface-Controlled Conductive Fibers for Wearable Strain Sensors and Stretchable Conducting Wires. *ACS Appl. Mater. Interfaces* **10**, 14087–14096 (2018).

# Chapter 3 - Solvodynamic Printing as A High-Resolution Printing Method

## 3.1 Introduction

The patterning of functional materials is an important aspect of manufacturing technology as it is essential in the fabrication of devices like microelectronic integrated circuits, microelectromechanical systems, optoelectronic devices and DNA microassays.[1–4] As reviewed in the previous chapter, traditional patterning is done by complex and expensive lithographic techniques. Non-contact printing presents a low cost and simple alternative. However, the resolution of these techniques is currently limited by the ink footprint from the nozzle and the subsequent ink spreading on the substrate.

In this chapter, a simple and novel solution to improve the printing resolution by tackling the two factors using solvent-solvent forces will be presented. The inspiration of this method is drawn from microfluidic microreactors, which synthesize materials within tiny droplets carried by an immiscible carrier solvent through a micron-scale channel.[5] It is hypothesized that the incorporation of an immiscible carrier solvent into the ink delivery system can reduce the dimension of the ink ejected from printheads and alter the ink substrate interactions, leading to improvements in resolution. This technique is named "Solvodynamic printing" as the improvement in resolution arises from the molecular interactions between the ink and the immiscible carrier solvent. The proof-of-concept of solvodynamic printing will be demonstrated by applying the technique to printing silver nanoparticle inks and focus on improving print resolution from a 300-micron nozzle.

## 3.2 Solvodynamic Printing

### 3.2.1 Printing Principles

In order to achieve good control over the fluid behaviour between two immiscible fluids, microfluidic chips will be employed in the printer setup. Microfluidic chips are devices with narrow channels used to manipulate the flow of small amounts of fluids.[6] Microfluidic chips are currently already used for many applications like fluid mixing, material synthesis and other biomedical applications.[7–10]

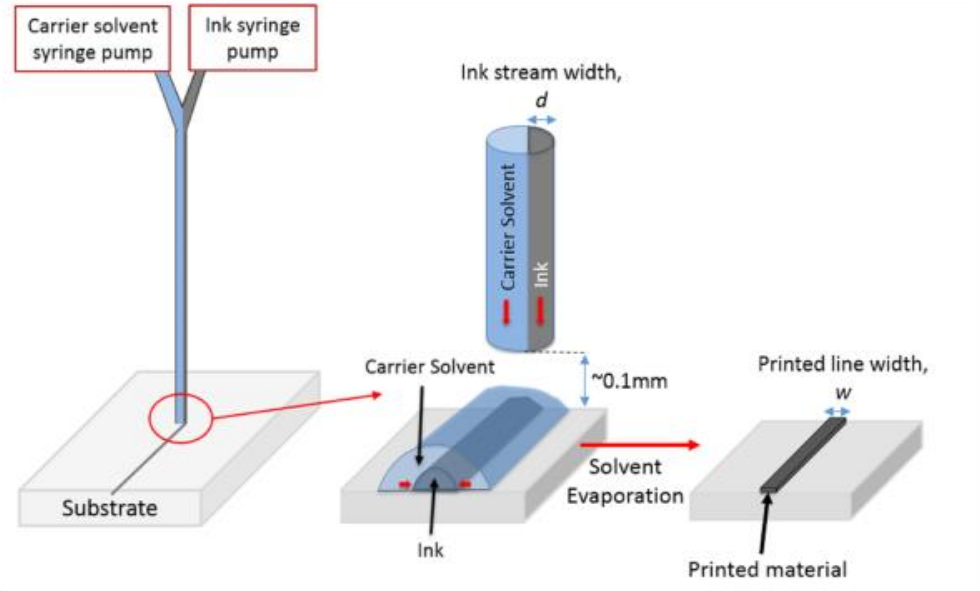



Figure 3-1: Schematic of solvodynamic printing with relevant parameters. The carrier solvent is a solvent immiscible with the printing ink that is meant to improve printing resolution by reducing the size of the ink ejected from the printer and alter the wetting behaviour of the ink on the substrate. *d* denotes the width of the ink stream within the microfluidic channel and *w* denotes the final width of the dried printed line.

Figure 3-1 shows the schematic of the solvodynamic printing setup. Under operation, the carrier solvent and ink are pumped into a Y-junction microfluidic channel through two inlets. Phase separation occurs when they meet due to their immiscible nature, causing the ink to flow alongside the carrier solvent through the channel. The fluids subsequently exit through the outlet nozzle of the chip and are deposited onto a substrate placed below the

nozzle. After all the solvent has evaporated, the printed material will be left on the substrate. To control the printed pattern, the substrate is placed on a X-Y stage and moves relative to the stationary nozzle.

### 3.2.2 Controlling Flow Behaviour

The flow characteristic of the fluids within the microfluidic chip is an important part of solvodynamic printing as it determines the configuration of the ink-carrier mixture as it leaves the printer nozzle. The flow behaviour between immisible fluids can typically be characterised using different dimensionless numbers like the Capillary (*Ca*), Weber (*We*) and Reynolds (*Re*) numbers as shown below.[11]

$$Ca = \frac{\mu V}{\sigma_{ic}} \tag{3-1}$$

$$We = \frac{\rho V^2 L}{\sigma} \tag{3-2}$$

$$Re = \frac{\rho V L}{\mu} \tag{3-3}$$

where $\mu$ is the fluid dynamic viscosity, $V$ is the fluid velocity, $\sigma_{ic}$ is the interfacial energy between the two fluids, $\rho$ is the fluid density, $L$ is the characteristic length of the flow and $\sigma$ is the surface tension of each individual fluid.

The flow of two immiscible fluids in a micro-sized channel can occur in two main ways: droplet and parallel flow as shown in Figure 3-2.[12] The type of flow which occurs is determined by the balance of the interfacial tension between the ink and carrier solvent and the viscosities of the fluids. This is typically characterized by the Capillary number in equation 3-1.[13] Low *Ca* indicates that the interfacial energy between the fluids dominates the viscous forces. This promotes the formation of ink droplets to reduce the overall interfacial area and minimize interfacial energy of the system. On the other hand, high *Ca*

indicates that viscous forces dominate, allowing the ink stream to remain intact through the channel and form a parallel flow. Some studies also found relationships between flow regime and the Weber numbers of the two fluids as higher flow rates tend to stabilize parallel flow.[14] The exact conditions which cause a transition between the droplet and parallel flow regime are not well-understood. However, it is established that the transition is strongly dependent on the junction shape, fluid flow rate ratio, viscosity ratios aside from *Ca* and We.[15,16]

Both flow regimes can be used to perform solvodynamic printing with the droplet formation regime behaving like a droplet-on-demand printing system while the parallel flow regime behaves more like a jetting mode.[15] In this study, the parallel flow regime will be used as it should be more suitable for printing linear features which are commonly used in printed electronics applications.

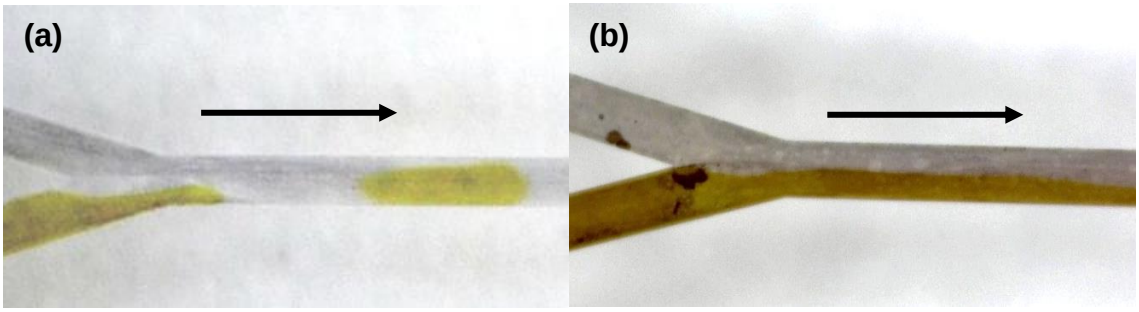



Figure 3-2: Different flow regimes for two immiscible fluids: (a) Droplet formation and (b) Parallel flow. The arrows indicate the direction of the fluid flow.

The presence of the carrier solvent confines the ink to flow through a smaller part of the microfluidic channel and therefore creates a flow focusing effect on the ink stream.[17] This effectively reduces its stream width below the physical limits of the channels and nozzles. It is hypothesized that this would have a beneficial effect on print resolution.

The flow focusing effect is easily controlled by the relative flow rates of the two fluids.[18] By increasing the carrier solvent flow rate ($q_c$) relative to the ink flow rate ($q_i$), the shear force exerted by the carrier solvent stream on the ink stream increases and deforms it to flow within a narrower region. In this study, the relative flow rate, $Q$ will be defined as $\frac{q_c}{q_i}$. Figure 3-3 demonstrates the effect of altering $Q$ on the resultant width of the ink stream. The arrow represents the direction of fluid flow. In all images, the carrier solvent and ink are pumped in from inlets on the left side. The carrier solvent is the colourless liquid flowing in from the top inlet and the coloured ink flows in from the bottom inlet. With increasing $Q$, the ink stream becomes narrower.

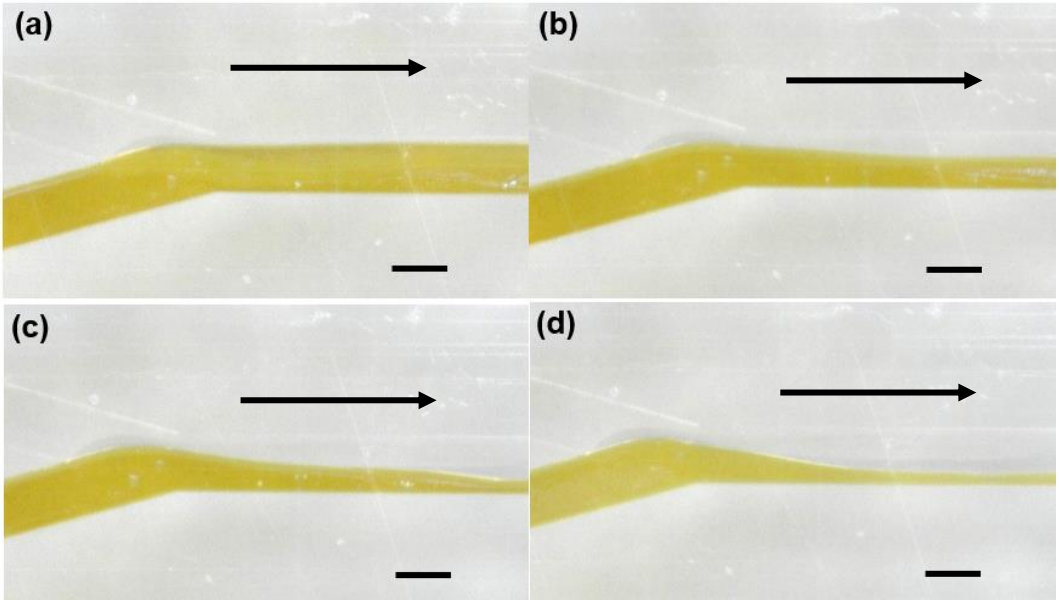



Figure 3-3: Micrograph of fluid carrier solvent (clear) and ink (coloured) flow within the microfluidic chip at different nominal relative flow rates. Flows for nominal relative flow rates of (a) 1, (b) 3, (c) 5 and (d) 8. The scale bar represents 200 μm. The arrows indicate the direction of fluid flow.

### 3.2.3 Ink Wetting Behaviour

The incorporation of the carrier solvent also alters the ink wetting behaviour on the substrate after deposition. Given that the ink is denser than the carrier solvent, the carrier solvent will be able to surround the ink droplet on the substrate as shown in Figure 3-1. The presence of the carrier solvent around the ink alters the interactions between the ink and substrate.[19]

The wetting behaviour of the ink, which is characterised by its contact angle, is important in printing as it is related to the area of contact between the ink and the substrate and therefore the dimensions of the resultant printed pattern.[20] The contact angle is determined by the interactions between three sets of interfacial energies as shown in Figure 3-4a and is mathematically described by the Young's equation:[21]

$$cos\theta_i = \frac{\sigma_{sa} - \sigma_{si}}{\sigma_{ia}} \tag{3-4}$$

where $\sigma_{sa}$, $\sigma_{si}$ and $\sigma_{ia}$ are the substrate-air, substrate-ink and ink-air interfacial energies and $\theta_i$ is the resultant contact angle of the ink in air.

In solvodynamic printing, the wetting medium is changed from air to the carrier solvent. This changes two of the interfacial energies in the system and therefore alters the equilibrium contact angle of the ink. The Young's equation can be modified to give:

$$cos\theta^* = \frac{\sigma_{sc} - \sigma_{si}}{\sigma_{ic}} \tag{3-5}$$

where $\theta^*$ is the new equilibrium contact angle of the ink when completely surrounded by the carrier solvent. $\sigma_{sc}$ and $\sigma_{ic}$ are the interfacial tensions between the carrier solvent with the substrate and with the ink respectively.

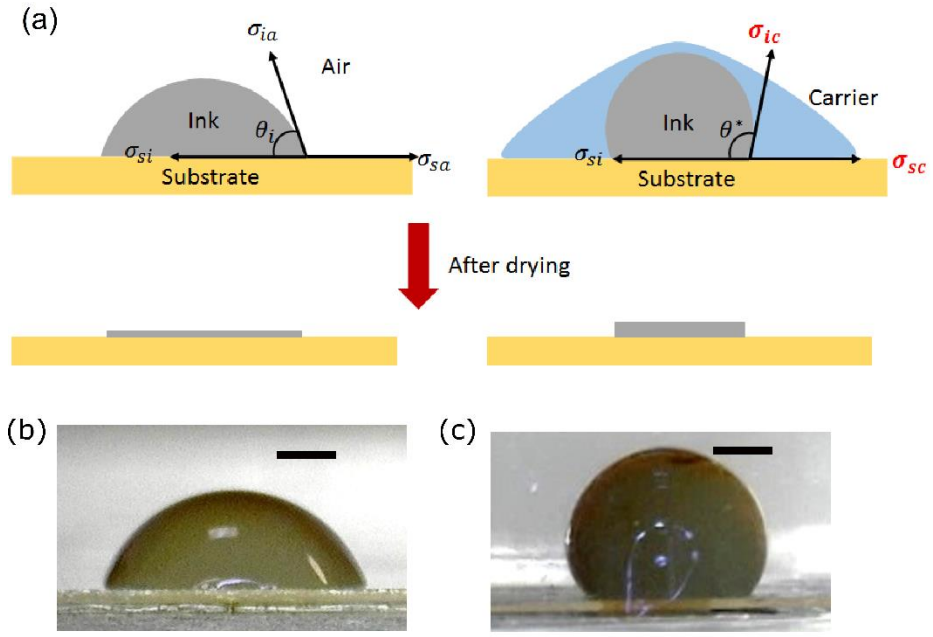



Figure 3-4: (a) Schematics of how changing wetting medium leads to improvements in resolution. The cross section geometry of the ink will be used to set up a model in the later section. $\theta_i$ and $\theta^*$ represent the equilibrium contact angle of the ink droplet in air and in carrier solvent respectively. $\sigma_{ia}$, $\sigma_{si}$, $\sigma_{sa}$, $\sigma_{ic}$ and $\sigma_{sc}$ are the interfacial tensions between ink-air, substrate-ink, substrate-air, ink-carrier solvent and substrate-carrier solvent respectively. (b) Demonstrating the actual change in wetting behaviour of an aqueous silver nanoparticle ink droplet in air and (c) in hexane carrier solvent. Scale bar represent 0.1 mm.

Therefore, with the appropriate choice of carrier solvent, the contact angle can be increased which reduces the degree of spreading leading to higher printing resolution. Intuitively, this means that by choosing an appropriate carrier solvent which has more favourable carrier-substrate interactions than ink-substrate interactions, the three-phase contact line will shift to reduce the ink-substrate interface area, leading to higher print resolution. An example of this is shown in Figure 3-4b and 3-4c. Figure 3-4b shows the profile of a droplet of aqueous ink on a substrate in air. When the medium is changed to a hexane carrier solvent, the contact angle increased drastically as shown in Figure 3-4c.

## 3.3 Materials and Methods

### 3.3.1 Materials

Silver nitrate, ethylene glycol (EG), sodium chloride and polyvinylpyrrolidone (PVP) with average molecular weight of 55000 were purchased from Sigma Aldrich.

Silver nanoparticles used in this study were synthesized via the polyol process.[22] In a typical synthesis, 0.0955 g of silver nitrate was dissolved in 0.75 ml of ethylene glycol. In a separate glass vial, 1.0 g of PVP was dissolved in 10 ml of ethylene glycol and heated to 135 °C with magnetic stirring. 20 µL of a 0.15 M aqueous sodium chloride solution was then added to the PVP solution. Once the solution was mixed homogenously, the silver nitrate solution was added and left for 1 hour. After the reaction, the nanoparticles were washed with methanol and centrifuged at 6000 rpm. This was repeated 3 times before finally re-dispersing the nanoparticles into a water-EG mixture to form the printing ink. 6 different inks with varying EG-water compositions were used during this study. Their properties are summarized in Table 3-1.

Table 3-1: Summary of properties of inks used

| Ink | EG content (wt%) | AgNP content (mg/ml) | Viscosity (mPa·s) | Surface Tension (mN/m) | Density ($g/cm^3$) |
|---|---|---|---|---|---|
| 1 | 0 | 6.0 | 0.905 | 85.2 | 1.01 |
| 2 | 5 | 6.0 | 0.926 | 79.9 | 1.01 |
| 3 | 10 | 6.0 | 0.945 | 74.3 | 1.02 |
| 4 | 15 | 6.0 | 0.966 | 70.9 | 1.02 |
| 5 | 17.5 | 6.0 | 0.981 | 68.8 | 1.02 |
| 6 | 20 | 6.0 | 1.02 | 66.5 | 1.03 |

### 3.3.2 Solvodynamic Printer Set-up

Figure 3-5a and b shows the printing set-up and its schematic diagram respectively. The entire printing system consisted of two syringe pumps (Harvard Apparatus Model '11' Plus 70-2208), a microfluidic chip (Cellix Ltd) and a set of computer-controlled translational stage (Thorlabs DDSM50). The set-up was built on an optical breadboard.

The syringe pumps were used to pump the silver nanoparticle ink and carrier solvent into the microfluidic chip at a controlled rate by inputting the syringe inner diameter and desired volumetric flow rate on the pump. The pump ran on a 0.9° step angle motor with a step size of 0.8 μm and has a flow accuracy of ±1%. The fluids were loaded into 1 ml syringes with inner diameters of 4.6 mm. For these syringes, the minimum and maximum possible flow rate according to the pump specifications were 2.9 μl/hr and 791.8 μl/min respectively. The maximum possible pressure applied by the pump was 6.89 bar. Each syringe was connected to the microfluidic chip using a 10 cm long Tygon connector tubing. One end of the tubing was connected to the syringe on the syringe pump through a luer lock syringe needle. At the other end of the tubing, a cylindrical hollow stainless steel pin was inserted partially into the tubing. The exposed end of this pin can be inserted into the inlet of the microfluidic chip to form a connection between the tubing and the microfluidic chip. The stainless steel pin had inner and outer diameters of 0.3 mm and 0.5144 mm respectively. Another pin was also inserted into the outlet of the microfluidic channel and functioned as the printing nozzle.

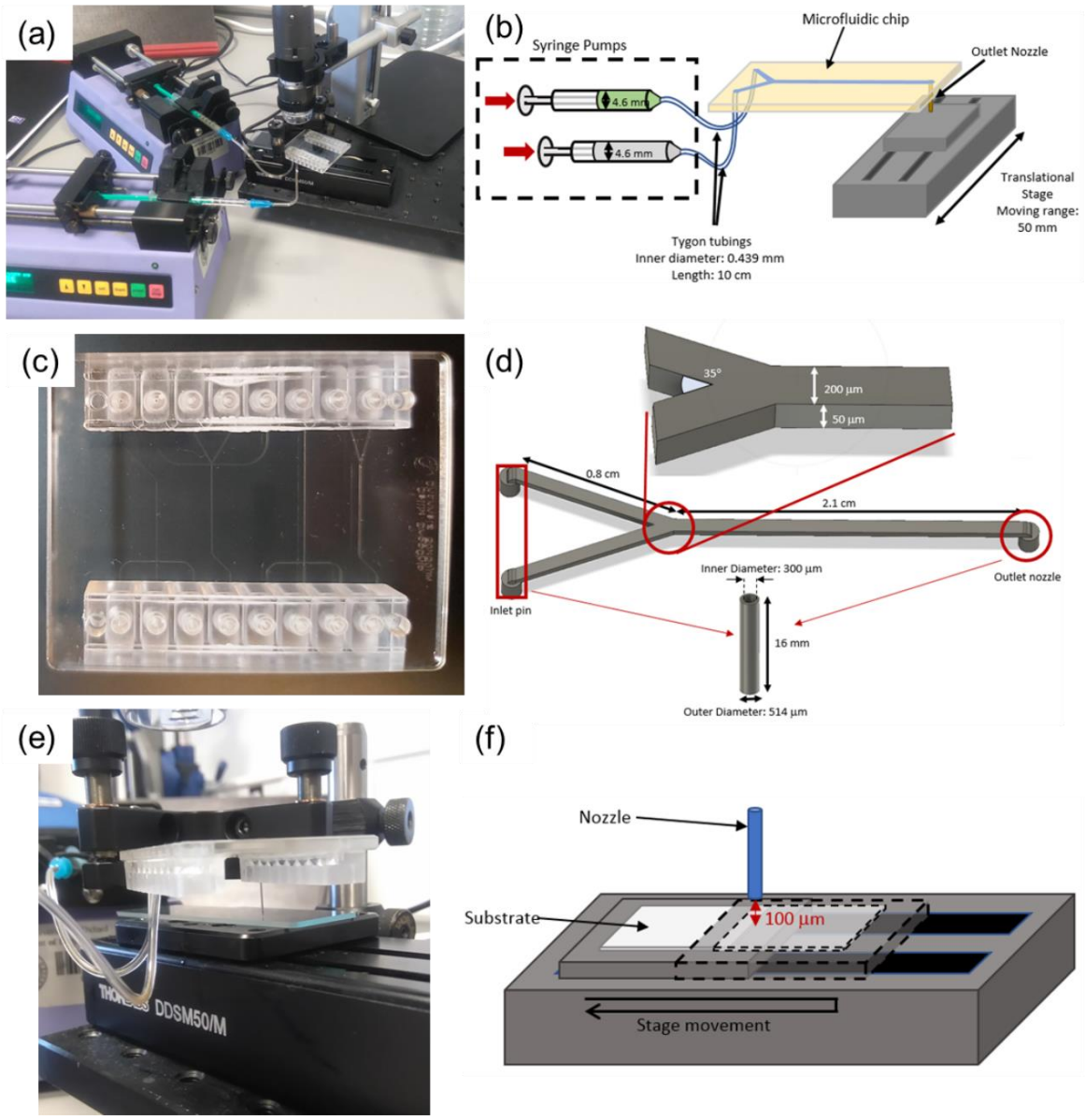



Figure 3-5: (a) The solvodynamic printing set up used in this study. (b) Schematics of the solvodynamic printier, consisting of two syringe pumps, microfluidic chip and translational stage. (c) A close up image of the microfluidic chip used. The junction on the furthest right is the Y-shaped junction used. The inlets are at the top and the outlet is at the bottom of the chip. (d) Schematics and dimensions of the Y-junction microfluidic channel within the chip. (e) Close up image of the nozle and translational stage. (f) Schematics of the nozzle and translational stage position and stage movement during printing.

Figure 3-5c shows an image of the microfluidic chip used. It was made from acrylic and had a series of different junctions on it. In this study, the Y-shaped junction located on the extreme right in Figure 3-5c was used. Figure 3-5d shows the schematic of the Y-junction

microfluidic channel with dimensions. The angle at the Y-junction is 35° and the channels have a rectangular cross section a width of 200 μm and depth of 50 μm. The channel walls were coated with a hydrophobic coating. During printing, the fluids from the syringe pumps entered the chip through two separate inlets and exited the chip through an outlet pin. The chip was clamped at two corners by a square mount (Thorlabs KM200S) attached to an optical post using a right-angle post clamp. The height of the microfluidic chip can be changed by adjusting the height of the right-angle clamp on the vertical optical post. The entire structure is secured on the optical breadboard such that the outlet pin from the chip is positioned directly above the translation stage as shown in Figure 3-5 e and f.

The translation stage used was a direct drive stage with a minimum travel distance of 500 nm and a travel range of 50 mm. It had a positional accuracy of ±5 μm and a bidirectional repeatability of ±1.5 μm. The straightness and flatness of the stage movement path were both ±5 μm across the full travel range. It was mounted on the breadboard and could be programmed by a Thorlabs software Kinesis®. The software allowed the programming of stage movements in terms of the move range, direction, move speed and pauses between moves. The software was also used to directly control the stage through an USB connection to run programmes or perform on-demand movements.

### 3.3.3 Summary of Experimental Conditions and Parameters

Lines of AgNPs were printed using the 6 different inks as listed in Table 3-1. The PEN substrates were first cut into 3.8 cm by 2.6 cm rectangles. They were then cleaned by ultrasonication in Decon soap, deionized water and ethanol for 5 mins each sequentially. They were then adhered to 3.75 cm by 2.6 cm microscope slides using double-sided tape to

keep the substrates flat during printing. The substrates were then treated using an UV-ozone cleaner (Ossila) for between 2 to 4.5 mins.

In the meantime, the AgNP ink and hexane were loaded into separate 1 ml syringes and attached onto the syringe pumps. The desired ink and carrier solvent flow rates were then input into the syringe pumps. As the flow rates input on the syringe pumps may not be the same as the actual flow rates, the flow rates settings on the syringe pumps will from here on be referred to as the nominal flow rates denoted by $\tilde{q}_c$ and $\tilde{q}_i$ for the carrier solvent and ink respectively. Similarly, the nominal relative flow rate set on the syringe pumps will be denoted by $\tilde{Q}$. $\tilde{q}_i$ values of between 20 μl/hr to 50 μl/hr were used for the prints. The corresponding $\tilde{q}_c$ values were set based on the desired $\tilde{Q}$, which ranged from 0 to 8. This translated to a nominal carrier solvent flow rate ranging from 0 to 400 μl/hr. For experiments involving $\tilde{Q}$ = 0, no carrier solvent was used. Instead, both syringes were filled with AgNP ink and the nominal ink flow rate was divided equally between the two syringe pumps.

Once the substrates were treated by the ozone cleaner, they were placed on the translational stage. The stage was homed to its 0 position, which is at one extreme end of the stage. The position of the microfluidic chip was adjusted as shown in Fig. 3-5f such that the outlet nozzle was positioned above the edge of the substrate which was closer to the centre of the translational stage. The height also needed to be adjusted such that the nozzle was 100 μm above the substrate. This was done by using another piece of PEN as a spacer between the substrate and the nozzle as the thickness of the PEN was approximately 100 μm. When the setup was ready, the syringe pumps are switched on. Initially, higher values of $\tilde{q}_i$ and $\tilde{q}_c$ can be set to speed up the flow of the two fluids through the connector tubing between the syringe and the microfluidic chip as it can take a long time when the flow rates are low. The

fluid flow towards the microfluidic chip were visually monitored as the Tygon tubings are transparent. When both fluids are close to the inlet of the chip, the two nominal flow rates were set back to the values as required by the printing experiment.

When the ink began to flow out of the nozzle onto the substrate, the preprogrammed stage movement was initiated through the software. For this part of the study, the stage was programmed to move from position at 0 mm to 35 mm, pause for 1 second and move back from 35 mm back to 0 mm with another pause for 1 second. This movement is represented by the "stage movement" arrow in Figure 3-5f. The movement sequence was set to loop repeatedly until it is manually stopped on the software interface. The stage and substrate velocity, $v_s$ was varied between 20 to 40 $mms^{-1}$. A line of ink was deposited during each move step from one end of the substrate to the other. Each time a line was completed, the substrate was shifted sideways using a pair of tweezers during the 1 second pause to move the nozzle to a new position above the substrate for the next line to be printed during the subsequent move step. Typically, at least 5 lines were printed on each piece of substrate. After printing, the substrate was then moved onto a hotplate to be dried at 110°C for 10 mins. For each set of printing parameter, at least 10 lines were printed for characterization. Table 3-2 summarizes the overall range of each printing parameters tested.

Table 3-2: Summary of experimental parameters used

| Parameter | Definition | Range tested |
|---|---|---|
| Nominal ink flow rate, $\tilde{q}_i$ (μl/hr) | Flow rate set on the syringe pump which pumps the AgNP ink | 20-50 |
| Nominal carrier solvent flow rate, $\tilde{q}_c$ (μl/hr) | Flow rate set on the syringe pump which pumps the carrier solvent | 0-400 |
| Nominal relative flow rate, $\tilde{Q}$ | Ratio of nominal carrier solvent flow rate to nominal ink flow rate | 0-8 |
| Substrate velocity, $v_s$ (mm/s) | Velocity of substrate moving under the nozzle which is determined by the programmed stage velocity | 20-40 |
| Ink EG content (wt%) | Amount of ethylene glycol in ink solvent to tune ink surface tension | 0-20 |
| Substrate ozone treatment time (min) | Time substrates undergo ozone plasma treatment to tune substrate surface energy | 2-4.5 |

### 3.3.4 Characterization Methods

The ink viscosity was characterized by a Malvern Bohlin Gemini HR Nano Shear Rheometer using viscometry mode with a 40 mm parallel stainless steel plate and 100 μm gap. The shear rate applied on the ink was increased steadily from 0.2 $s^{-1}$ to 400 $s^{-1}$ during the measurement. 10 measurement points were taken during each run and 3 runs were done to obtain an average result. The ink density was calculated by measuring the mass of 2 ml of ink, which was measured using a weighing balance. The measurements were repeated 3 times to obtain an average value.

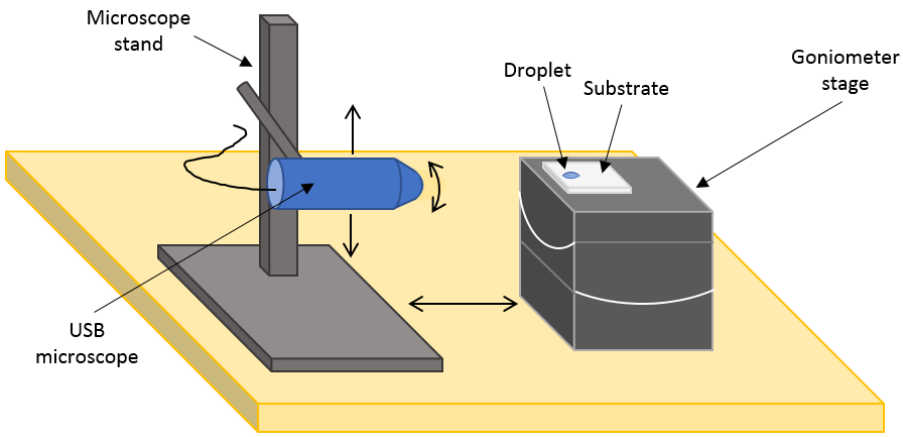



Figure 3-6: Schematic of contact angle measurement set-up consisting of a USB microscope clamped on a stand with the substrate placed on a goniometer stage

The ink surface tensions and substrate surface energies were determined by taking contact angle measurements and analyzing them using a modified Equation of States approach developed by Kwok and Neumann.[23] Their model estimates the interfacial energy between the solid substrate and the ink droplet using the following equation:

$$\sigma_{si} = \sigma_{ia} + \sigma_{sa} - 2\sqrt{\sigma_{ia}\sigma_{sa}}e^{-\beta(\sigma_{ia}-\sigma_{sa})^2} \quad (3\text{-}6)$$

The constant $\beta$ in equation 3-6 has been studied empirically using a wide range of liquids and substrates. It was found that $\beta$ was largely independent on the substrate-liquid system with an approximate value of 0.0001247 $m^2/mN^2$. The use of equation 3-6 reduces equation 3-4 to three variables, $\theta$, $\sigma_{ia}$ and $\sigma_{sa}$. Therefore $\sigma_{sa}$ of a substrate can be deduced by measuring the contact angle, $\theta$ of a liquid with known $\sigma_{ia}$ on the substrate. Conversely, the surface tension of an ink can be deduced from its contact angle on a solid with known surface energy.

The contact angle measurements were done using a custom-built set up as shown in Figure 3-6. The substrate was placed onto a manual goniometer stage. The stage was verified to be

horizontal using a spirit level. A USB microscope (Dino-Lite AM4815ZTL) was used to view the substrate from the side to observe the contact angle. The microscope is small and cylindrical in shape, making it easy to position. It also has a long working distance ranging from 30.5 mm to 234.5 mm depending on the magnification, which is set by rotating a knob located on the microscope. It has magnification of up to 140x and a resolution of approximately 2 μm. The microscope is connected to a computer using a USB port and the image detected by the microscope can be displayed and captured on a Dino-lite software. During the measurement, the microscope was mounted on a stand (Dino-Lite RK10) and directed at the substrate and goniometer stage side-on. The stand has a horizontal arm which the microscope can be clamped on. The height of the arm can be adjusted by turning a knob on the stand. Droplets of the sample liquid was then deposited manually on the substrate using a syringe with a 34G needle (TSK). The plunger of the syringe is gently pressed until a small droplet starts to form at the needle tip. The droplet was then placed directly onto the substrate for observation. The small diameter of the needle allowed small droplets to be produced.

To obtain a good image on the microscope, an appropriate magnification is set on the microscope depending on the droplet size and a focused image was obtained by adjusting the distance between the microscope and the substrate. The height and angle of the microscope had to be adjusted to ensure that it was taking an image side-on rather than at an angle from below or above the horizontal. To make this adjustment, the position of the microscope was initially positioned slightly higher than the substrate and angled downwards towards the substrate. At this position, the back of the substrate and a reflection of the droplet on the substrate can be seen on the image. From this position, the microscope's angle was slowly tilted upwards towards the horizontal while lowering its height on the stand to

keep the image of the droplet in view. The adjustment was done until the back of the substrate and reflection of the droplet on the substrate could no longer be seen in the image. Once the microscope was positioned properly, images of the droplets were taken and the contact angle were measured from the angle measurement tool on the Dinolite software. For each measurement, the average contact angles from 5 droplets were taken.

Some contact angle measurements were also taken for ink droplets which are surrounded by varying amounts of carrier solvent. The was done to characterize how the contact angle changed with $\tilde{Q}$. In these measurements, a substrate was placed on the stage below the printer nozzle. The two syringe pumps were run for an approximately 5 seconds to eject a small amount of ink and carrier solvent onto the substrate. The substrate was kept stationary. After the droplet has been deposited, the stage is controlled to move out from under the nozzle so that the contact angle can be measured by the USB microscope in the same way as described above.

The contact angle of the ink droplets when completely submerged in hexane was also characterized. In these measurements, the substrate was cut and placed at the bottom of a cuvette. The cuvette is then filled with the carrier solvent. The USB microscope was positioned and focused at the substrate at the bottom of the cuvette in a similar way as the standard contact angle measurements. Droplets of inks were then deposited onto the subtrate using a syringe and needle. Side views of the droplets will be captured using the microscope and the contact angle can be measured.

The actual ink flow rates at different preset nominal flow rates and actual $Q$ were characterized by running the syringe pumps with the desired $\tilde{q}_i$ and $\tilde{q}_c$ for 2 hours. A cuvette

was used to collect the fluids dispensed. The empty cuvette was first weighed on a weighing scale. A piece of parafilm was then used to cover the opening to minimize the loss of solvents through evaporation. It was then placed under the microfluidic chip outlet with the nozzle pin piercing through the parafilm to allow the fluids to be collected in the cuvette. After running the system for 2 hours, the cuvette was weighed with the fluids inside. From this measurement, the total mass of hexane and ink in the cuvette can be deduced. The cuvette was then gently heated on a hotplate to remove all solvents, leaving behind the AgNPs. The cuvette was then re-weighed again to obtain the mass of the AgNPs. Given the concentration of AgNPs in the ink was fixed at 6 mg/ml, the total volume of AgNP ink that was collected can be deduced. From this, the mass of the ink could be calculated using the ink density. As a final step, the mass and volume of the hexane could also be deduced using the total mass of both fluids obtained in the earlier weighing. All weighing steps are repeated at least 3 times to obtain an average mass for each measurement.

The ink stream width within the microfluidic channel during printing was characterized using the USB microscope. The microscope was clamped to the Dinolite stand and positioned to point directly at the microfluidic chip from above as shown in Fig. 3-5a. The desired magnification was set and the working distance is adjusted using a knob on the stand to obtain a focused image. The microfluidic chip is transparent so the inside of the channel can be observed from a top down perspective. To achieve a clear contrast in the image, a small slip of white paper was taped to the bottom side of the microfluidic chip so that the top view image taken by the microscope would have a white background to see the coloured ink stream more clearly. The microscope was calibrated using a calibration target provided by the supplier and the imaging software to ensure the lengths measured are accurate. During printing, the entire width of the channel would typically be divided into a colourless

hexane stream and a greenish AgNP ink stream. The width of the ink stream is taken as the perpendicular distance from the channel wall to the observed interface with the colourless hexane stream and can be directly measured from the micrographs. As the ink stream width only stabilized some distance away from the junction, all measurements were done at positions at least 5 mm away from the Y-junction. 10 measurements were taken along the downstream points to obtain an average ink stream width at each ink and carrier solvent flow rate.

The resultant width of the printed lines were also characterized using the USB microscope. Typically, at least 10 measurements were made for each printed line. The morphology of the printed lines was also characterized by scanning electron microscopy (JOEL-840F SEM). The cross-section profile of the printed lines was obtained by surface profilometry (Veeco DekTak 6M stylus profiler) which used a 12.5 μm radius diamond tip stylus. The measurement settings were 3 mg stylus force, scan length 0.5 mm with a resolution of 0.167 μm.

### 3.4 Results and Discussion

In this section, the effect of three printing parameters, ink stream width, ink surface tension and substrate surface energy on the resultant printed line widths will be studied. In order to better analyse the observed trends, a simple mathematical model is first setup to identify the fundamental determinants of the printed line widths. The relation between the printing parameters and these fundamental determinants will then be explored. The experimental results will also be fitted in the mathematical model to test its validity. The printed line widths will also be minimized by finding the optimal value of each printing parameter to obtain the highest resolution achievable by the solvodynamic printer.

### 3.4.1 Mathematical Model

Based on the concepts introduced in section 3.2, a simple mathematical equation was derived to relate the achievable resolution of solvodynamic printing to the printing parameters. In this model, the printed ink lines are assumed to be infinitely long and have uniform truncated circular cross sections as in Figure 3-4a. By considering the geometry of a circular segment, the width of the printed line, $w$ can be related to the contact angle, $\theta$ and the cross-sectional area of the segment, denoted by $A$ as follows:

$$w = 2sin\theta\sqrt{\frac{A}{\theta - sin\theta cos\theta}} \tag{3-7}$$

The cross-sectional area, $A$, can then be expressed in terms of ink loading per unit length along the printed line by considering the conservation of volume of ink:

$$A = \frac{q_i}{v_s} \tag{3-8}$$

where $v_s$ is the substrate's velocity beneath the nozzle. Combining (3-7) and (3-8), a combined expression (3-9) is obtained which relates the printing resolution to the printing parameters. An additional fitting parameter $k$ is added to take into account any systematic mismatch between the modelled results and experimental results.

$$w = 2ksin\theta\sqrt{\frac{q_i}{v_s(\theta - sin\theta cos\theta)}} \tag{3-9}$$

From this equation, we can identify three main parameters, $q_i$, $\theta$ and $v_s$, which directly affects the printed line widths. $q_i$ has a positive relation with $w$ since more ink deposited per unit time will lead to wider lines. The term $\frac{sin\theta}{\sqrt{(\theta - sin\theta cos\theta)}}$ is decreasing in $\theta$. This reflects the fact that higher contact angle leads to smaller line widths due to the reduce spreading on the substrate. $v_s$ is another factor in the equation which varies negatively with $w$. This makes

sense as a higher velocity leads to less ink per unit length in the printed lines, which leads to thinner lines. The validity of equation 3-9 will be verified in subsequent sections using experimental results.

### 3.4.2 Ink Stream width

The main hypothesis regarding the working mechanism of solvodynamic printing is the improvement in resolution by focusing the flow of ink into a narrower stream. Therefore, at first glance the width of the ink stream within the microfluidic channel during printing appears to be a parameter of interest. Experimentally, the ink stream width at a fixed nominal ink flow rate, $\tilde{q}_i$ can be controlled by varying the nominal carrier solvent flow rate, $\tilde{q}_c$ set on the syringe pumps. Essentially, this is equivalent to changing the nominal relative flow rate, $\tilde{Q}$. The ink stream width is optically characterized from a top down view of the microfluidic channel. Since the ink stream is confined between the channel wall on one side and the carrier solvent stream on the other, the ink stream width is defined as the distance from the channel wall in contact with the ink stream to the interface between the ink and carrier solvent stream. Table 3-3 shows the measured ink stream width at different $\tilde{Q}$ while $\tilde{q}_i$was fixed at 50 μl/hr. This nominal flow rate was used as is was the flow rate used in most of the printing experiments. It was noted that the ink stream width was largely independent of the type of ink used.

Table 3-3: Observed ink stream at different nominal relative flow rates used

| Nominal relative flow rate, $\tilde{Q}$ | Nominal ink flow rate, $\tilde{q}_i$ (μl/hr) | Nominal carrier solvent flow rate, $\tilde{q}_c$ (μl/hr) | Ink stream width (μm) | Carrier solvent stream width (μm) |
|---|---|---|---|---|
| 0 | 50 | 0 | 200 | 0 |
| 0.5 | 50 | 25 | 180 | 20 |
| 1 | 50 | 50 | 159 | 41 |
| 1.5 | 50 | 75 | 134 | 66 |
| 2 | 50 | 100 | 125 | 75 |
| 3 | 50 | 150 | 102 | 98 |
| 4 | 50 | 200 | 74 | 126 |
| 5 | 50 | 250 | 41 | 159 |
| 7 | 50 | 350 | 36 | 164 |
| 8 | 50 | 400 | 35 | 165 |

Although the ink stream width gives a measure of the confinement of the ink stream by the carrier solvent, it may not be an ideal parameter to use in this study due to the shape of the interface between the two streams in the microfluidic channel. Numerical studies on parallel flow in microfluidic channels have typically shown that the interface between the two fluids is generally not straight and is dependent on other factors like channel surface energy and interfacial tension between the two fluids.[24] As a result, the ink stream width obtained from a top view of the channel may not be representative of the actual ink stream. Figure 3-7 demonstrates this using a comparison between two sets of flows at the same nominal flow rate settings but with inks with different surface tensions. The two ink streams had similar stream widths but their colour contrast are quite different despite being taken at the same setting. This is likely due to a difference in the interface shape between the two fluids as represented by the inset in the figure. The interfacial tension between the 20% EG ink and hexane is lower which results to a more curved interface shape. Therefore, the ink stream width may be misleading as the bulk of the ink flow may be much closer to the channel wall instead of near the middle of the channel. Overall, the ink stream width can only be used as

an approximate estimate of the degree of confinement of the ink stream by the carrier solvent, especially when comparing between different inks.

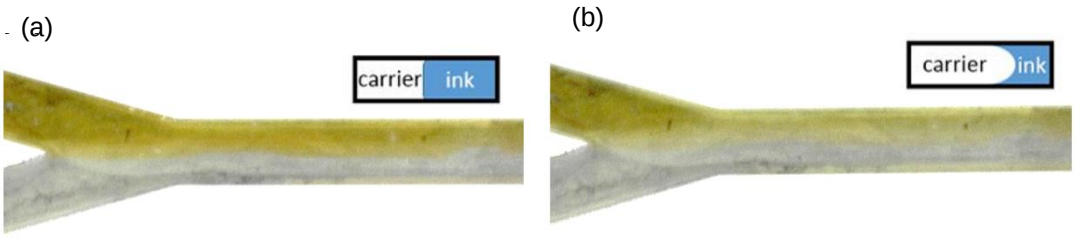



Figure 3-7: Micrographs of ink flow in microfluidic channels using (a) high surface tension ink with 0 wt% EG and (b) low surface tension ink with 20 wt% EG (right) at a nominal relative flow rate of 3 with nominal ink flow rate of 50 μl/hr. Inset diagram are the schematics of the cross-sectional shape of ink stream for the respective micrographs.

### 3.4.2.1 Control of Ink Flow Rates using Carrier Solvent

Since the ink stream width is not an ideal parameter of study, an alternative choice is either the relative flow rate $Q$ or the ink flow rate $q_i$. Both parameters are experimentally varied through the nominal settings on the syringe pumps. $Q$ is the parameter which describes the ratio of carrier solvent to ink flowing through the microfluidic channel which directly controls the ink stream width. In addition, it is also indicative of the ratio of carrier solvent to ink being deposited on the substrate which may have an effect on the ink contact angle. Therefore, $Q$ could generally be a more meaningful parameter which still captures the effect of ink stream width. The other option, $q_i$ is usually set as a constant value and so should theoretically be constant when the amount of carrier solvent is varied. However, from equation 3-9, $q_i$ is a parameter which directly affects the achievable resolution, so it is useful to test the validity of the mathematical model.

To gain a better understanding in the relationship between these flow rate parameters, the ink and hexane flow rates were characterized by running the syringe pumps printing

continuously and analyzing the total amount of hexane and ink which flows out of the nozzle. The results are tabulated in Table 3-4 to 3-6. The nominal ink flow rate was fixed at 50 μl/hr for these measurements.

Table 3-4: Measured ink flow rates at various nominal $\tilde{Q}$ with different inks

| | | | Measured $q_i$ for inks with varying EG content (μl/hr) | | | | |
|---|---|---|---|---|---|---|---|
| $\tilde{Q}$ | $\tilde{q}_i$ (μl/hr) | $\tilde{q}_c$ (μl/hr) | 0% | 5% | 10% | 15% | 20% |
| 1 | 50 | 50 | 7.02 | 7.72 | 9.90 | 11.4 | 13.1 |
| 2 | 50 | 100 | 10.3 | 13.1 | 13.4 | 14.8 | 19.3 |
| 3 | 50 | 150 | 15.0 | 17.2 | 19.7 | 20.5 | 28.7 |
| 5 | 50 | 250 | 18.1 | 20.9 | 22.4 | 25.4 | 29.6 |
| 8 | 50 | 400 | 26.4 | 29.4 | 31.9 | 35.6 | 37.9 |

Table 3-5: Measured hexane flow rates at various nominal $\tilde{Q}$ with different inks

| | | | Measured $q_c$ for inks with varying EG content (μl/hr) | | | | |
|---|---|---|---|---|---|---|---|
| $\tilde{Q}$ | $\tilde{q}_i$ (μl/hr) | $\tilde{q}_c$ (μl/hr) | 0% | 5% | 10% | 15% | 20% |
| 1 | 50 | 50 | 8.78 | 8.71 | 8.42 | 8.93 | 9.14 |
| 2 | 50 | 100 | 28.8 | 30.0 | 27.8 | 30.4 | 32.3 |
| 3 | 50 | 150 | 70.5 | 71.2 | 74.0 | 72.3 | 74.6 |
| 5 | 50 | 250 | 153 | 157 | 160 | 154 | 151 |
| 8 | 50 | 400 | 338 | 352 | 337 | 334 | 327 |

Table 3-6: Actual relative flow rates at various nominal $\tilde{Q}$ with different inks

| | | | $Q$ for inks with varying EG content | | | | |
|---|---|---|---|---|---|---|---|
| $\tilde{Q}$ | $\tilde{q}_i$ (μl/hr) | $\tilde{q}_c$ (μl/hr) | 0% | 5% | 10% | 15% | 20% |
| 1 | 50 | 50 | 1.25 | 1.13 | 0.85 | 0.79 | 0.70 |
| 2 | 50 | 100 | 2.79 | 2.29 | 2.07 | 2.05 | 1.67 |
| 3 | 50 | 150 | 4.73 | 4.14 | 3.76 | 3.52 | 2.60 |
| 5 | 50 | 250 | 8.49 | 7.51 | 7.13 | 6.07 | 5.11 |
| 8 | 50 | 400 | 12.78 | 11.98 | 10.54 | 9.36 | 8.63 |

From the results tabulated in Tables 3-4 and 3-5, several observations were made. Firstly, the actual flow rates of both ink and hexane were lower than the nominal flow rates set on

the syringe pumps. This is an unusual observation in syringe pump driven flows but it could be due to the effect of the large microfluidic resistance from the confined channels. The microfluidic resistance of a fluid flowing through a channel is proportional to the channel length and inversely related to the channel cross-sectional area.[25,26] The relatively long channel with a small cross-sectional area creates a large microfluidic resistance which opposes the pressure exerted by the pump and reduces the resultant ink flow rate. In addition, several parts of the microfluidic chip such as the connection between the channel and inlet and outlets creates additional constrictions, which creates additional resistance against the syringe pumps action. The variation in $q_c$ and $q_i$ also lead to a resultant $Q$ which differs from $\tilde{Q}$ as tabulated in Table 3-6. In general, a higher $\tilde{Q}$ still corresponded to a greater $Q$, although to different degrees depending on the ink used.

The second observation is that the actual ink flow rate $q_i$ increased with nominal relative flow rate $\tilde{Q}$ even though the nominal $\tilde{q}_i$ was fixed at 50 μl/hr for all measurements. This is an interesting behavior as we would have expected a constant ink flow rate. The results suggest that the increased flow in hexane caused by an increase in $\tilde{Q}$ somehow led to a higher ink flow rate. This observation may be due to a coupling effect between the two different fluid streams through interactions at the ink-carrier solvent interface. When the hexane flow rate is increased by increasing $\tilde{q}_c$, the hexane flow velocity increases as well. This can be verified by dividing the flow rate $q_c$ in Table 3-5 by the cross-sectional area of the stream estimated using the carrier solvent stream width in Table 3-3. The resultant hexane flow velocities are tabulated in Table 3-7. Indeed, we observe that as $\tilde{q}_c$ is increased, the carrier solvent stream velocity is increased. It is noted that these velocities are estimates assuming that the streams have perfectly rectangular cross sections with height and width equivalent to the microfluidic channel height and carrier solvent stream width respectively.

Although we have established that this assumption does not hold in most cases, it is sufficient to serve as a comparison between flows using the same type of ink since they would have similar interface shapes. Similarly, the ink flow velocities are also estimated and tabulated in Table 3-8.

Table 3-7: Estimated hexane flow velocities at various nominal $\tilde{Q}$ with different inks

| | | | Hexane flow velocities when using inks with varying EG content (mm/s) | | | | |
|---|---|---|---|---|---|---|---|
| $\tilde{Q}$ | $\tilde{q}_i$ (μl/hr) | $\tilde{q}_c$ (μl/hr) | 0% | 5% | 10% | 15% | 20% |
| 1 | 50 | 50 | 1.19 | 1.18 | 1.14 | 1.21 | 1.24 |
| 2 | 50 | 100 | 2.13 | 2.22 | 2.06 | 2.25 | 2.39 |
| 3 | 50 | 150 | 4.00 | 4.04 | 4.20 | 4.10 | 4.23 |
| 5 | 50 | 250 | 5.35 | 5.49 | 5.59 | 5.38 | 5.28 |
| 8 | 50 | 400 | 11.31 | 11.78 | 11.28 | 11.18 | 10.94 |

Table 3-8: Estimated ink flow velocities at various nominal $\tilde{Q}$ with different inks

| | | | Ink flow velocities of inks with varying EG content (mm/s) | | | | |
|---|---|---|---|---|---|---|---|
| $\tilde{Q}$ | $\tilde{q}_i$ (μl/hr) | $\tilde{q}_c$ (μl/hr) | 0% | 5% | 10% | 15% | 20% |
| 1 | 50 | 50 | 0.245 | 0.270 | 0.346 | 0.398 | 0.458 |
| 2 | 50 | 100 | 0.458 | 0.582 | 0.596 | 0.658 | 0.858 |
| 3 | 50 | 150 | 0.817 | 0.937 | 1.073 | 1.117 | 1.563 |
| 5 | 50 | 250 | 2.453 | 2.832 | 3.035 | 3.442 | 4.011 |
| 8 | 50 | 400 | 4.314 | 4.804 | 5.212 | 5.817 | 6.193 |

With the increase in velocity in the hexane stream, part of the increased momentum can be transferred to the ink stream through interactions along the interface which then increases the overall ink velocity and flow rate through the channel. Simulation studies in the literature on parallel flow between hexane and water shows that the flow velocity of the two fluids at the interface are always equalized regardless of the velocity profiles in each stream.[15] Any differences in flow velocity at the interface causes a net shear force at the interface which then causes the momentum transfer. Therefore, an increase in flow velocity of one fluid can

cause the velocities in the other fluid to increase as well. Similar phenomena have also been observed in immiscible fluids flows through porous media, whereby an increase in permeability of one fluid through the medium also increases the resultant flow rate of the other.[27] Such flows are quite similar to microfluidic flows as they are both characterized by low Reynolds number flows through small confined channels or spaces. This observation is quite important as the ink flow rate $q_i$ directly affects the printing resolution as seen in equation 3-9. Therefore, we may expect the resolution to deteriorate when printing at high $\tilde{Q}$.

The last observation is that an increase in the ink flow rate was also observed when ink with higher EG content was used. This will be discussed again in a later section when the effect of EG content in the ink is examined.

3.4.2.2 Effect of Carrier Solvent on Ink Contact Angle

The other important effect of the relative ink flow rate is the induced change in the ink's contact angle on the substrate. Theoretically, when the ink is surrounded by the carrier solvent, the system will attain a new equilibrium contact angle $\theta$*. To understand how the change in the equilibrium contact angle occurs, contact angle measurements were performed on the ink while varying $\tilde{Q}$ from 0 to 8 to mimic the printing conditions. A small volume of ink and hexane was deposited from the printer onto the PEN substrate by starting and stopping the syringe pumps for an approximate time interval of 5 seconds simultaneously at the preset $\tilde{Q}$. The stage was set to be stationary so that an ink droplet was deposited instead of a line so that the contact angle can be characterised. Figure 3-8 shows an example of the droplet profiles which are obtained this way. The hexane forms a faint darker outline which

surrounds the droplet. The contact angle of the resultant ink droplet deposited on the substrate is measured and the results are shown in Table 3-9.

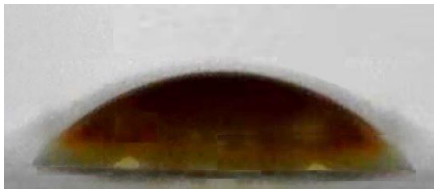


Figure 3-8: A micrograph of the side view of an ink droplet surrounded by hexane as carrier solvent. The ink had 20% EG and was deposited with $\tilde{Q} = 3$ on a PEN substrate which was ozone treated for 3.5 mins.

Table 3-9: Contact angle of different ink droplets deposited under different flow rate conditions onto a PEN substrate ozone treated for 3.5 mins

| | | | Measured $\theta$ for inks with varying EG content (°) | | | | |
|---|---|---|---|---|---|---|---|
| $\tilde{Q}$ | $\tilde{q}_i$ (μl/hr) | $\tilde{q}_c$ (μl/hr) | 0% | 5% | 10% | 15% | 20% |
| 0 | 50 | 0 | 54.6 | 45.6 | 40.4 | 28.8 | 26.0 |
| 1 | 50 | 50 | 70.5 | 61.5 | 57.2 | 48.9 | 44.7 |
| 2 | 50 | 100 | 86.8 | 77.1 | 71.9 | 68.2 | 64.2 |
| 3 | 50 | 150 | 85.2 | 74.5 | 70.8 | 67.2 | 63.0 |
| 5 | 50 | 250 | 85.8 | 76.6 | 71.4 | 67.8 | 63.4 |
| 8 | 50 | 400 | 87.5 | 76.7 | 72.9 | 69.1 | 64.8 |

Table 3-10: Contact angle of ink droplets with different EG content deposited on a PEN substrate ozone treated for 3.5 mins while submerged in a large volume of hexane

| Ink EG content (%) | 0 | 5 | 10 | 15 | 20 |
|---|---|---|---|---|---|
| Contact angle (°) | 87.1 | 77.6 | 70.4 | 68.8 | 64.4 |

The results showed that the contact angle increased gradually when $\tilde{Q}$ was increased from 0 until a maximum contact angle was attained by $\tilde{Q}$ = 2 for all the inks. The contact angle remained constant for further increase in $\tilde{Q}$ beyond this point. It is likely that this maximum $\theta$ corresponds to the new equilibrium $\theta^*$ of the AgNP inks under hexane. This was verified

by measuring the contact angle of droplets deposited in a large volume of hexane held in a cuvette as listed in Table 3-10. Indeed, there is good agreement between the contact angles, verifying that when $\tilde{Q}$ = 2, the contact angle reaches an equilibrium contact angle $\theta^*$ for a system of the AgNP ink in hexane. By referring to Table 3-6, this corresponds to an actual $Q$ value of between 1.67 and 2.79 depending on which type of ink was used. This initial gradual increase in contact angle is likely due to the incomplete coverage of hexane over the ink when $Q$ is too low, leading to an intermediate contact angle between $\tilde{Q}$ = 0 to $\tilde{Q}$ = 2. Consequently, it is expected that the printed line widths will decrease from $\tilde{Q}$ = 0 to $\tilde{Q}$ = 2 from this increase in contact angle.

#### 3.4.2.3 Effect of Carrier Solvent on Printed Line Widths

So far, it has been established that the increase in $\tilde{Q}$ during printing can affect the printing resolution through $q_i$ and $\theta$ with opposite effects. To see the overall effect when the amount of carrier solvent used is increased, lines of AgNPs were printed using different $\tilde{Q}$ as shown in Figure 3-9a-e. Figure 3-9a shows the control line which was printed without the use of carrier solvent, at $Q$ = 0. Without the use of carrier solvent, a printed line width of approximately 300 μm was achieved. As $Q$ was increased, it is observed that the printed lines became thinner. The reduction in line width with the use of carrier solvent shows the proof-of-concept of solvodynamic. The printed line width decreased to a minimum before increasing again at high values of $Q$.

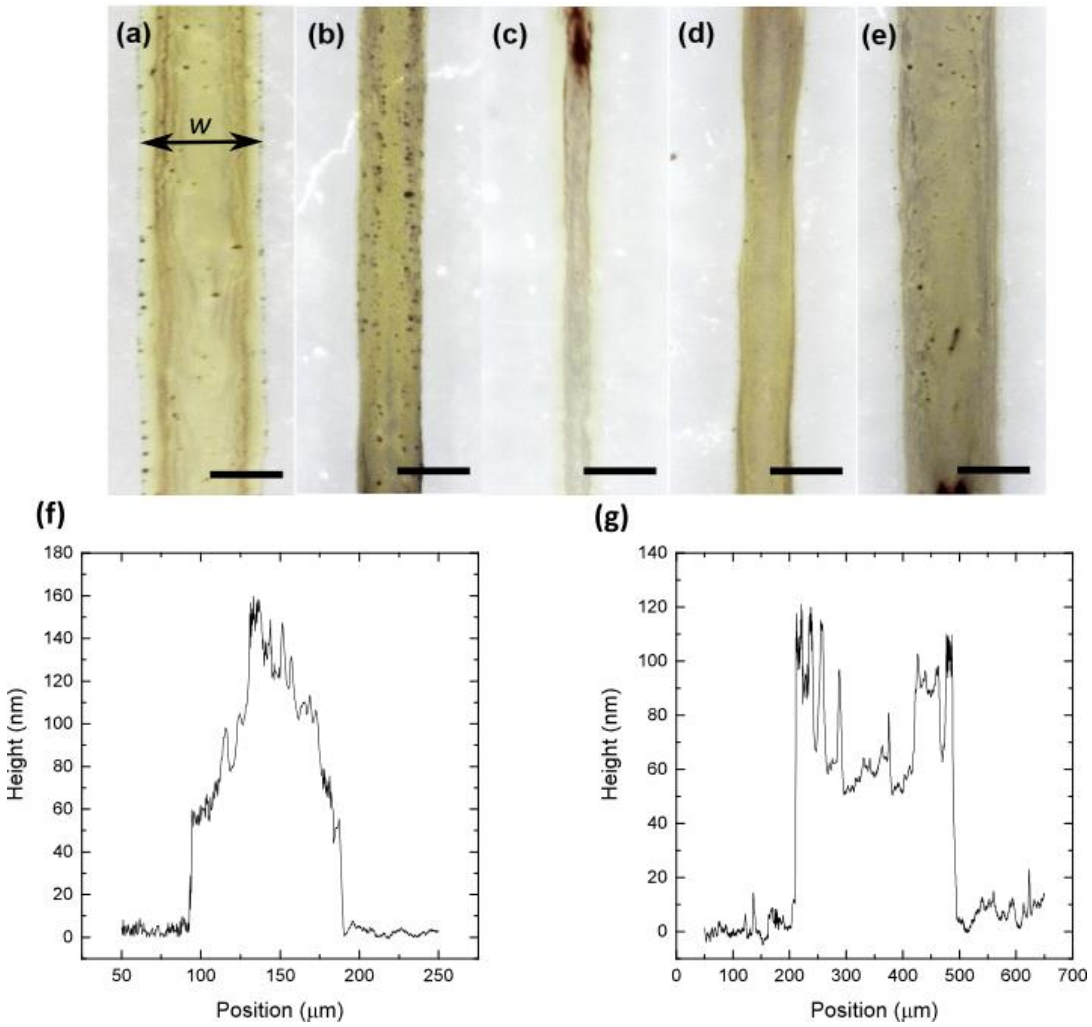



Figure 3-9: Micrographs of solvodynamic printed lines with widths denoted by *w*. They were printed while varying the nominal relative ink flow rate, $\tilde{Q}$. Lines were printed with $\tilde{Q}$ = (**a**) 0, (**b**) 1, (**c**) 2, (**d**) 5 and (**e**) 8. The ink flow rate was fixed at 50 µl/hr. The ink used consisted of silver nanoparticles with concentration of 6 mg/ml dispersed in water with 15 wt% of ethylene glycol. The substrate used was polyethylene naphthalate which was ozone-treated for 3.5 min. Substrate velocity was set at 20 $mms^{-1}$. Scale bars represent 200 µm. (**f**) and (**g**) are cross sectional profile of a solvodynamically printed line and a line printed without carrier solvent respectively.

Since hexane is much more volatile than water and therefore it would be expected that it would evaporate before the ink is fully dried. In addition, the ink should only start drying after the surrounding carrier solvent has evaporated. If this was the case, the carrier solvent should have had no effect on improving the printing resolution. Therefore, it is likely that the contact line has been pinned by the silver nanoparticles upon the initial

deposition. This is a common phenomenon in liquids with solutes or dispersed particles, which accumulate at the three-phase contact line due to inherent surface roughness or heterogeneity of the substrate.[28] As a result, the width of the printed lines remains fixed even after the carrier solvent has evaporated. The uneven cross section profile of a printed line as shown in Figure 3-9f supports the idea of contact line pinning. The profile shows that the middle of the line has accumulated more nanoparticles compared to the sides. This could be due to the drying characteristics of the printed lines. During the initial deposition, most of the hexane was accumulated near the bottom of the deposited ink due to gravity, leaving a thin layer of hexane around the top of the ink. Therefore, it is likely that the hexane at the top dried the quickest to expose the ink, causing the ink drying to begin from the middle of the printed lines towards the edges.[29] Conversely, the profile of the control line in Figure 3-9g shows more nanoparticles on the sides compared to the middle, which is a typical profile of a contact line pinned feature drying under normal conditions.

The experimental results of line widths printed using 0% and 15% EG inks using $0 < \tilde{Q} < 8$ is plotted on Figure 3-10. The line widths were plotted against the ink flow rates at each value of $\tilde{Q}$ while keeping $\tilde{q}_i$ constant at 50 μl/hr. As we recall from Table 3-4, $q_i$ increases with $\tilde{Q}$. Therefore, low $q_i$ in the graph corresponds to printing at lower $\tilde{Q}$ and vice versa. The ink stream width of the two inks are also plotted against a secondary axis in Figure 3-10. A smaller ink stream width corresponds to a higher flow rate. It can be observed that the two different inks followed different relations between ink flow rate and stream width. This shows why the ink stream width may not be a representative parameter to use since it does not necessarily correspond to any flow rates and differs when using different inks.

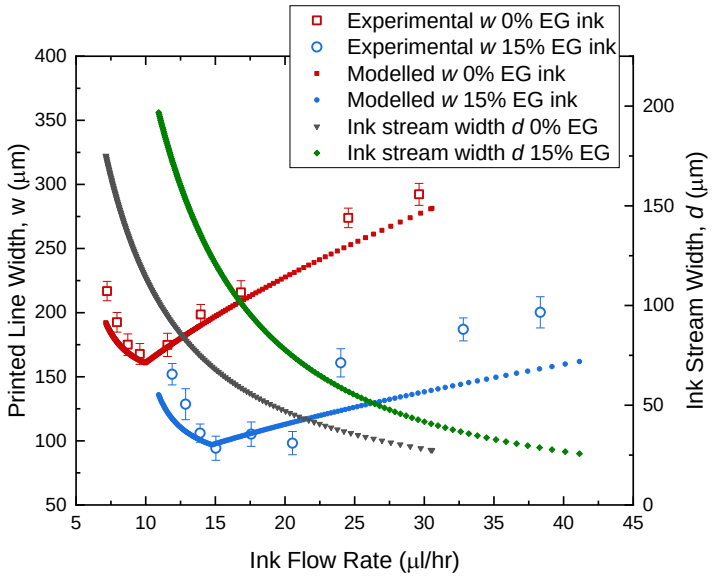



Figure 3-10: Experimental and modelled variation in printed line width (*w*) and ink stream width (*d*) with the change in ink flow rate for 0%EG and 15%EG inks.

The observed trend in the printed line widths is as expected based on the analysis on the effect of carrier solvent on $q_i$ and $\theta$ from the previous section. It was established that when $\tilde{Q} < 2$, an increase in $\tilde{Q}$ led to an increase in $\theta$, which would decrease the resultant line width. At the same time, an increase in $\tilde{Q}$ causes an increase in $q_i$, which leads to an increase in line width, *w*. Mathematically, the effect of this reduction in *w* was found to be larger than the increase in *w* caused by an increased $q_i$ in this range of $\tilde{Q}$ and therefore the overall *w* was observed to decrease. When $\tilde{Q} > 2$, the contact angle no longer changes while $q_i$ continues to increase with $\tilde{Q}$. Therefore, the overall printed line widths increase. The experimental results of $q_i$ and $\theta$ were used in the model equation 3-9 to perform data fitting to test the model. As shown in Figure 3-10, it can be seen that equation 3-9 is able to match the experimental data based on the empirical results well. Overall, the improvement in resolution is largely caused by the increasing contact angle of the ink in the presence of the carrier solvent. A further observation was that the lines printed with some EG content generally had thinner printed line widths than those printed with no EG. In addition, *k* had

to be varied when fitting the modelled data for inks with different compositions. These observations will be investigated in the next section.

### 3.4.3 Ink Surface tension

The second printing parameter of study is the ink surface tension. Inks with higher surface tension leads to larger contact angles and therefore less wetting and higher resolution can be achieved.[20] However, when the printed features are lines instead of droplets, the surface tension plays another role. Lines of ink deposited onto the substrate during printing are inherently unstable due to higher total interfacial energy between the ink and its surroundings. They tend to break up into more energetically stable droplets.[30,31] Therefore, there is an optimal surface tension for inks to achieve high resolution and good stability.

In this study, the ink surface tension was controlled by mixing EG as an ink co-solvent. EG was chosen as it is water soluble but immiscible with the hexane carrier solvent and has a lower surface tension than water. Several inks with different EG-water composition were made. A piece of PEN substrate which was ozone treated for 2 mins was used for the contact angle measurements. Its surface energy was first deduced by measuring the contact angle of a water droplet on its surface, which was approximately 49.9°. Since water has a surface tension of 72.8 mN/m, the surface energy of the substrate was estimated to be 54.27 mN/m using equations 3-4 and 3-6. The contact angles of the different AgNP inks were then measured and from the results the surface tension of the AgNP inks were calculated as shown in Table 3-11 and Figure 3-11f. As expected, the ink surface tension decreased with increasing amount of EG.

Table 3-11: Measured contact angle and calculated surface tension of several inks deposited on a PEN substrate ozone treated for 2 mins

| EG content (wt%) | Contact angle (°) | Surface tension (mN/m) |
|---|---|---|
| 0 | 66.9 | 86.48 |
| 5 | 57.4 | 78.85 |
| 10 | 37.4 | 74.25 |
| 15 | 46.4 | 70.92 |
| 17.5 | 43.1 | 68.75 |
| 20 | 39.4 | 66.52 |

The different inks were then used to print lines using $\tilde{Q}$ = 2 and 3, which achieved high resolutions from the previous experiments. Figure 3-11a-e shows the micrograph of the printed lines and the numerical data is tabulated in Figure 3-11g. It was first observed that some of the lines printed with the purely aqueous ink were unstable and broke up into droplets as shown in Figure 3-11a. This probably indicates that the surface tension of this ink was too high and formed unstable lines. As the surface tension decreased, more stable and longer lines could be formed. At the same time, the line widths decreased to a minimum before increasing again. This observation is quite interesting as lower surface tensions tend to increase wetting and *w* should increase. Therefore, it is likely that other parameters in the printing process were also contributing to changes in *w*.

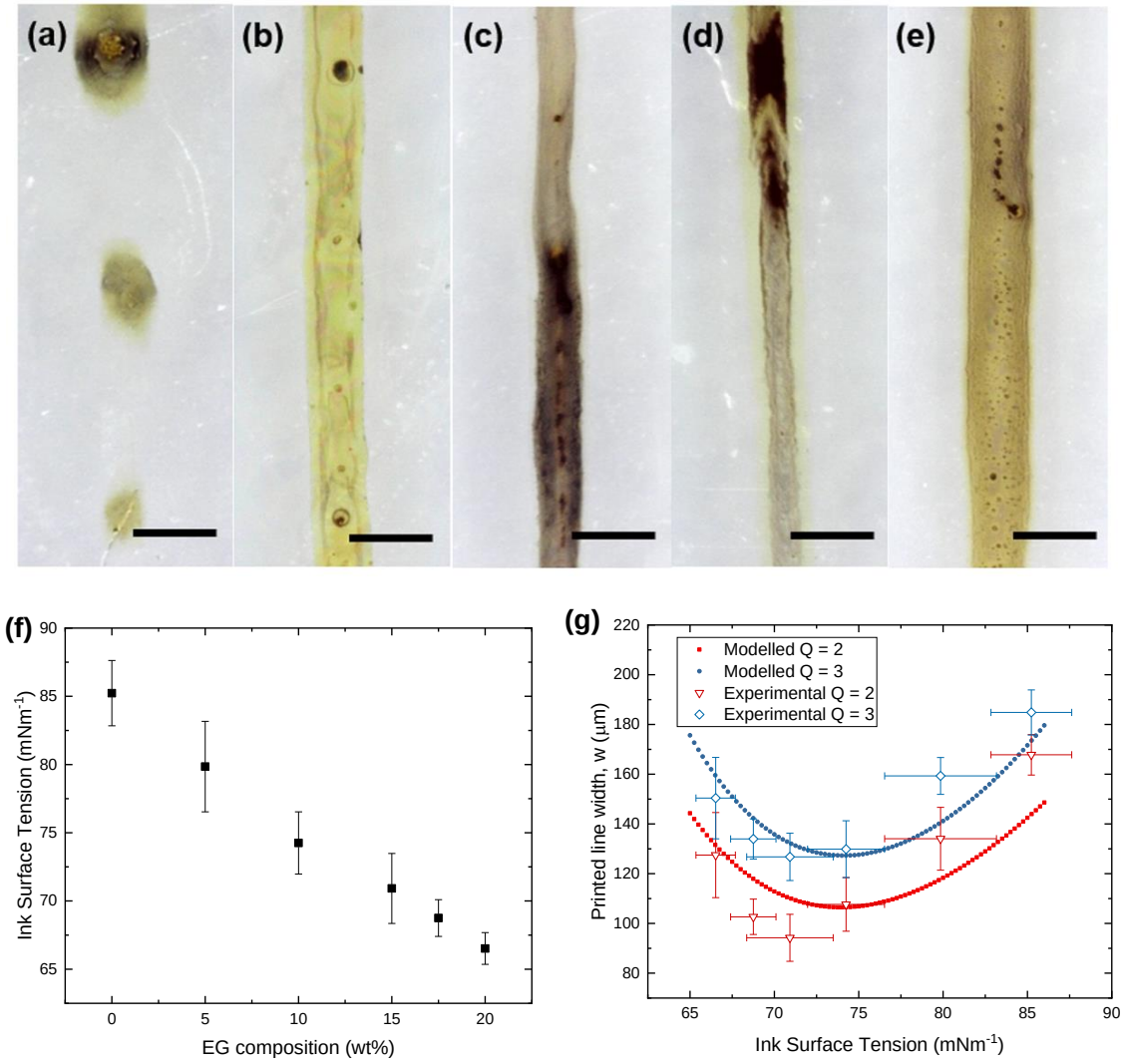



Figure 3-11: Micrographs of solvodynamic printed lines using inks with different surface tension by varying the amount of ethylene glycol mixed into the ink: (**a**) 0 wt%, (**b**) 5 wt%, (**c**) 10 wt%, (**d**) 15 wt%, (**e**) 20 wt%. The ink and carrier solvent flow rates were fixed at 50 µl/hr and 100 µl/hr respectively, inks consisted of silver nanoparticles with concentration of 6 mg/ml. The substrate used was polyethylene naphthalate which was ozone-treated for 3 min. Substrate velocity was set at 20 $mms^{-1}$. Scale bars represent 200 µm. (**f**) Variation in polyethylene naphthtalate substrate surface energy with the change in duration under ozone plasma treatment. (**g**) Experimental and modelled variation in printed line width ($w$) with the change in ink surface tension.

From Table 3-4 in the previous section, it was observed that the inks with lower surface tension had a higher resultant flow rate even when $\tilde{q}_i$ and $\tilde{q}_c$ are fixed. This is likely to be related to the coupling behaviour between the two ink streams. With a decrease in ink surface tension, the interfacial tension decreases and the interface between the two streams

become more curved which increases the area of contact between the two streams. This is analogous to the findings by Pasquier et. al. in their study of immiscible flow through porous media. They found that the interaction of the two immiscible fluids becomes more important when the interfacial area increases.[27] Applying the same concept to the microfluidic system, the flow between the carrier solvent and the ink may become more coupled as they help to pull each other through the channel. Consequently, the increase in ink flow rate in inks with lower surface tension would cause an increase in the resultant line width.

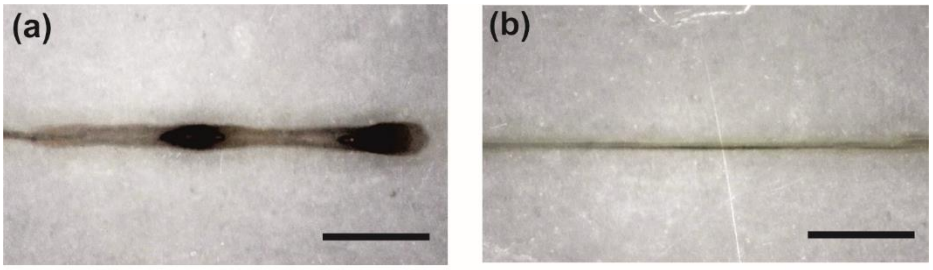



Figure 3-12: Low Magnification micrographs of printed lines using (**a**) 0 wt% EG ink and (**b**) 20 wt% EG ink. The scale bar represents 500 μm.

Table 3-12: Comparison of measured contact angles of several inks deposited on a PEN substrate ozone treated for 3.5 mins while being immersed in hexane and the corresponding observed printing parameter *k*

| EG content (%) | Surface tension (mN/m) | Contact angle (°) | Fitting parameter, *k* |
|---|---|---|---|
| 0 | 86.48 | 87.1 | 6.46 |
| 5 | 78.85 | 77.6 | 3.97 |
| 10 | 74.25 | 70.4 | 3.33 |
| 15 | 70.92 | 68.8 | 3.13 |
| 17.5 | 68.75 | 66.1 | 3.15 |
| 20 | 66.52 | 64.6 | 3.29 |

It was also observed in section 3.4.2.3 that the fitting constant *k* changed with the different inks used. Upon closer inspection on the shape of the printed lines, it is likely that this could

be related to the formation of unstable lines as mentioned earlier. An example is shown in Figure 3-12a. Some of the lines printed using a high surface tension ink is unstable and breaks into undulations with some of the inks concentrated into droplets. On the other hand, lines printed using lower surface tension inks as shown in Figure 3-12b remain stable.

This observation may be explained by prior work done by Davies, Schiaffino and Sonin who studied the stability of liquid rivulets deposited on solid surfaces.[30,31] The key result from their work showed that the lines are unstable and break up into periodic droplets when the contact angle of the liquid on the solid exceeds 90°. To verify the occurrence of this phenomenon in solvodynamic printing, the contact angles of the different inks was compared to the resultant *k* as tabulated in Table 3-12. The contact angles of the inks were measured on PEN substrates which have been ozone-treated for 3.5 mins while surrounded in hexane to mimic the same conditions for the printing. Indeed, there was a strong correlation between *k* and the contact angle of the ink. The 0% EG ink exhibited a high *k* of 6.46 with a contact angle very close to 90° while the rest of the inks had a much lower *k* of between 3 to 4 with contact angles much lower than 90°.

Although the contact angle of the 0% EG ink did not exceed 90°, it is very close to the theoretical limit of instability and small localized variation in the experimental conditions may bring the system beyond the stability limit. This is probably why not all the printed lines using the 0% EG ink were unstable. The printed lines show similar shapes as the wax beads presented in Schiaffino and Sonin's work. In the case of our printed lines, the contact line of the printed lines may be pinned by the AgNPs, which restricts the complete retraction of the contact line. This led to the formation of undulations as shown in Figure 3-12a.

Overall, the combination of effects from the contact angle $\theta$, ink flow rate $q_i$ and fitting parameter $k$ causes the observed variations in printed line width. An increase in ink surface tension $\sigma_{ia}$ causes the contact angle to increase and the ink flow rate to decrease. These two factors contribute to the observed decrease in printed line width for $65 < \sigma_{ia} < 74$ since $k$ does not vary much within this range. Beyond this range, $k$ begins to increase with $\sigma_{ia}$ as the contact angle begins to get closer to 90° which caused the lines to become less stable. The increase in $k$ dominates when $\sigma_{ia} > 74$ which leads to an increase in observed printed line width. From the results it appears that the ink with 15% EG achieves the thinnest line widths. Therefore, this ink will be used in the subsequent experiments for further optimization.

### 3.4.4 Substrate Surface Energy

The last parameter studied was the substrate surface energy. Generally, liquids can wet surfaces with higher surface energies better. Therefore, low surface energy substrates are used to achieve high resolution features. However, like the case for surface tension, substrates having too low surface energy will lead to instability in the printed lines. The effect of substrate surface energy on solvodynamic printing resolution should be quite predictable as it only affects the contact angle. Increasing the surface energy of the substrate will lead to increase in wetting of the ink and lead to poorer resolution.

Table 3-13: Measured contact angle of water droplets on substrates with varying ozone treatment time and their calculated surface energy

| Ozone treatment time (min) | Contact angle (°) | Surface energy (mN/m) |
|---|---|---|
| 2.0 | 49.9 | 54.27 |
| 2.5 | 45.9 | 56.14 |
| 3.0 | 40.0 | 59.38 |
| 3.5 | 36.6 | 61.18 |
| 4.0 | 31.1 | 63.93 |
| 4.5 | 22.0 | 67.97 |

In this study, the PEN substrate's surface energy was controlled by subjecting it to an ozone plasma treatment for different durations. The plasma treatment was necessary as the inks could not wet the untreated substrates at all. The resultant surface energies of the substrates were calculated from contact angle measurements of water droplets on each type of substrates. Table 3-13 and Figure 3-13e shows the variation of the PEN surface energy with different plasma treatment durations. Figure 3-13a-d shows a set of micrographs of the silver nanoparticle lines printed on substrates with varying substrate energy using the 15 wt% EG ink and relative flow rate of $\tilde{Q}$ = 2, which were found to be optimal in previous sections.

From Figure 3-13a, it was first observed that the sample with the lowest surface energy could not form stable silver lines due to the instability as discussed above. For the rest of the samples which could form stable lines as in Figures 3-13b-d, the printed line width increased with substrate surface energy as predicted. Figure 3-13f shows the overall variation of line widths with changing substrate energy for two sets of printed lines. Once again, the modelled data showed good match with the experimental results.

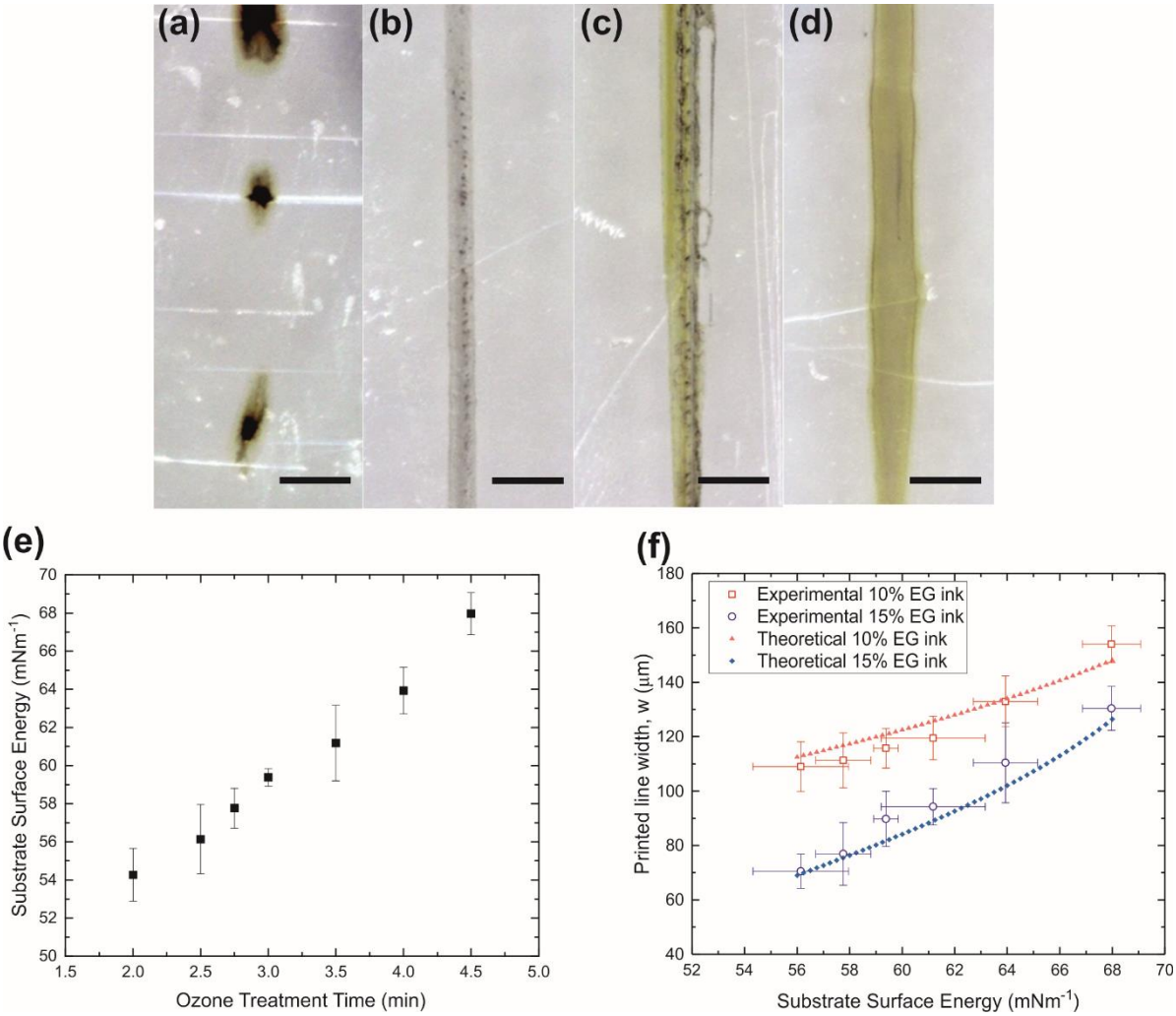



Figure 3-13: Micrographs of solvodynamic printed lines using polyethylene naphthalate substrates treated by ozone plasma for different times: (**a**) 2 min, (**b**) 2.5 min, (**c**) 3.5 min and (**d**) 4.5 min. The ink and carrier solvent flow rates were fixed at 50 µl/hr and 100 µl/hr respectively, ink consisted of silver nanoparticles with concentration of 6 mg/ml dispersed in water with 15 wt% of ethylene glycol. Substrate velocity was set at 20 $mms^{-1}$. Scale bars represent 200 µm. (**e**) Variation in substrate surface energy with the change in ozone plasma treatment time. (**f**) Variation in printed line width (*w*) of 2 sets of printed lines with change in substrate surface energy.

### 3.4.5 Overall Ink Loading

To further minimize the line widths to achieve the lowest resolution, the overall ink loading was adjusted by controlling the ink flow rate to substrate velocity ratio, $\frac{q_i}{v_s}$ as seen in the model. In this case, the ink flow rate is adjusted directly through the nominal ink flow rate setting on the syringe pump. The ratio of these parameters affects the ink loading per unit

length of the printed lines. The results are shown in Figure 3-14a. The substrate velocity was initially increased to 40 $mms^{-1}$ while keeping the nominal ink flow rate as 50 μl/hr. Thinner lines of approximately 40 μm were observed but the high substrate velocity seemed to be detrimental to the consistency of the system as the variance of the printed line widths increased dramatically. Therefore, the substrate velocity was lowered together with the nominal ink flow rate to keep the ink loading low while avoiding high substrate velocities. Eventually, an nominal ink flow rate of 20 μl/hr and substrate velocity of 22.5 $mms^{-1}$ were used. At these parameters, lines of approximately 35 μm with reasonable variance were printed. Any further decrease in the ink flow rate to substrate velocity ratio could not produce continuous lines probably due to the ink loading being insufficient. Figure 3-14c shows an SEM image of a typical printed line at these conditions. The line consists of closely packed AgNPs and the line boundaries are well-defined.

To determine a more accurate value of the attainable resolution of solvodynamic printing, a statistical approach was used. Ten line segments printed using the optimized parameters as shown in Figure 3-14b were examined. The widths were measured at points every 40 μm along the lines for 50 points per line. The distribution of the widths is then tabulated into a histogram as shown in Figure 3-14d. The average width is 35.2 μm with a standard deviation of 4.2 μm. As a statistical estimation, 90% of the printed line widths will fall within the range of 35.2 ± 7.0 μm. This is equivalent to 11.7 ± 2.3 % of the nozzle diameter.

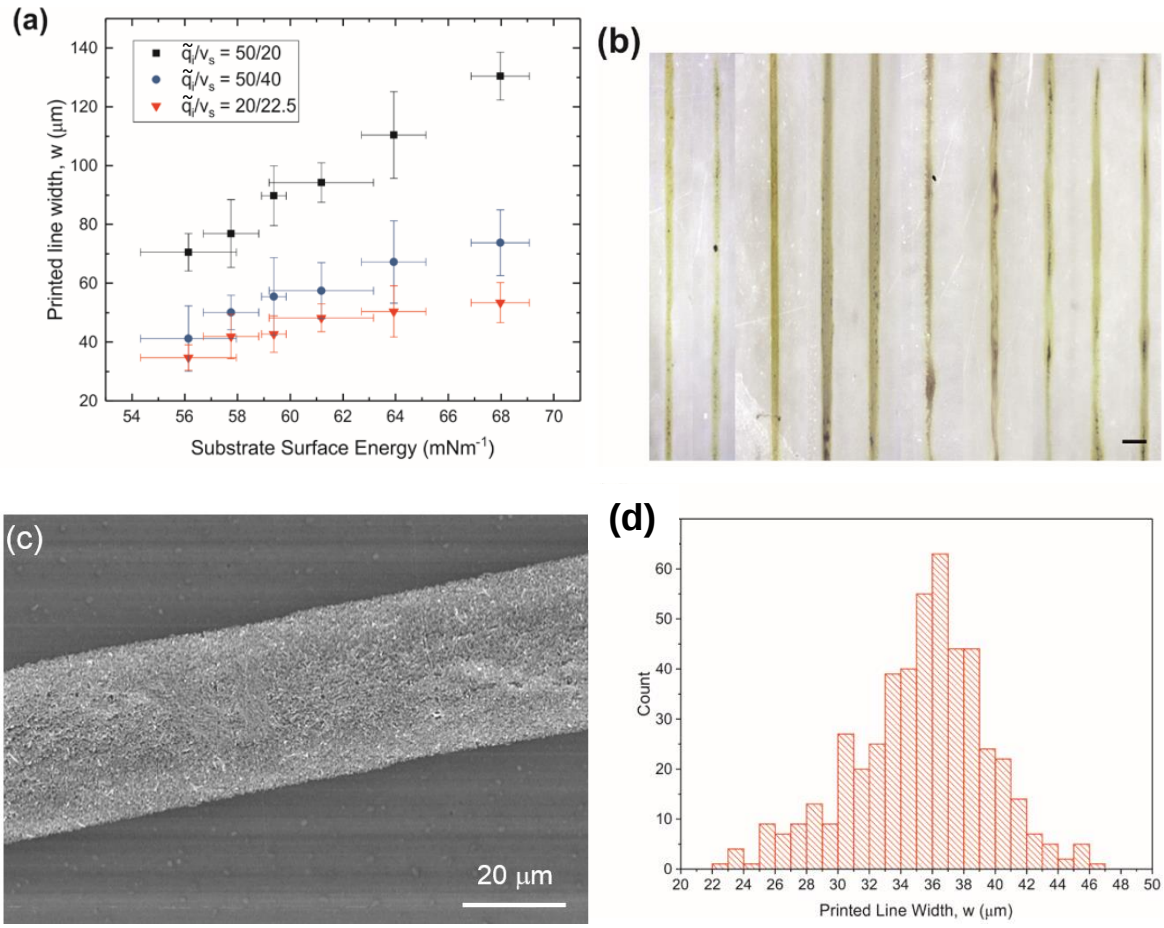



Figure 3-14: (a) Variation in printed line widths with substrate surface energy for 3 sets of lines printed with different nominal ink flow rate ($\tilde{q}_i$) to substrate velocity ($v_s$) ratios. Values of $\tilde{q}_i$ and $v_s$ are measured in μl/hr and mms$^{-1}$ respectively. The nominal carrier solvent to ink flow rate was fixed at 2 and the ink used with 15 wt% EG and 6 mg/ml silver nanoparticles. (b) Optical images of 10 printed lines at the optimized parameters. Scale bar represents 100 μm. (c) A SEM image of one of the printed lines. (d) The distribution of the line widths taken at points every 40 μm along the lengths of the 10 printed lines for 50 points per line.

## 3.5 Conclusion

In this chapter, the proof-of-concept of using solvent interactions between the ink and an additional immiscible solvent as a mean to improve printing resolution was shown. The improvement in printing resolution was primarily due to the increase in the ink contact angle with the substrate. The relation between different printing parameters and the achievable resolution was studied and a model was developed to explain the observed results. Using

this technique, lines of silver nanoparticles with widths of approximately 35.2 ± 7.0 μm were achieved using a 300 μm diameter nozzle, equivalent to 11.7 ± 2.3 % of the nozzle diameter. This result is promising and shows that there is still much potential for this technique to improve. With further downsizing of the system, even higher resolution can possibly be achieved. In addition, this technique may also be compatible with other resolution-improving techniques to further boost the achievable resolution of additive printing technology.

### 3.6 References


1. Seisyan, R. P. Nanolithography in microelectronics: A review. *Tech. Phys.* **56**, 1061–1073 (2011).
2. Qu, H. CMOS MEMS fabrication technologies and devices. *Micromachines* **7**, 1–21 (2016).
3. Jung, M. W. *et al.* Novel fabrication of flexible graphene-based chemical sensors with heaters using soft lithographic patterning method. *ACS Appl. Mater. Interfaces* **6**, 13319–13323 (2014).
4. Hölz, K. *et al.* High-Efficiency Reverse (5′→3′) Synthesis of Complex DNA Microarrays. *Sci. Rep.* **8**, 1–12 (2018).
5. Bannock, J. H. *et al.* Continuous synthesis of device-grade semiconducting polymers in droplet-based microreactors. *Adv. Funct. Mater.* **23**, 2123–2129 (2013).
6. Whitesides, G. M. The origins and the future of microfluidics. *Nature* **442**, 368–373 (2006).
7. Lee, C. Y., Chang, C. L., Wang, Y. N. & Fu, L. M. Microfluidic mixing: A review. *Int. J. Mol. Sci.* **12**, 3263–3287 (2011).
8. Boken, J., Soni, S. K. & Kumar, D. Microfluidic Synthesis of Nanoparticles and their Biosensing Applications. *Crit. Rev. Anal. Chem.* **46**, 538–561 (2016).
9. Liu, D. *et al.* A versatile and robust microfluidic platform toward high throughput synthesis of homogeneous nanoparticles with tunable properties. *Adv. Mater.* **27**, 2298–2304 (2015).
10. Oh, K. W. Multidisciplinary role of microfluidics for biomedical and diagnostic applications: Biomedical microfluidic devices. *Micromachines* **8**, 3–5 (2017).
11. Squires, T. M. & Quake, S. R. Microfluidics: Fluid physics at the nanoliter scale. *Rev. Mod. Phys.* **77**, 977–1026 (2005).
12. Ushikubo, F. Y., Birribilli, F. S., Oliveira, D. R. B. & Cunha, R. L. Y- and T-junction microfluidic devices: effect of fluids and interface properties and operating conditions. *Microfluid. Nanofluidics* **17**, 711–720 (2014).
13. Cubaud, T. & Mason, T. G. Capillary threads and viscous droplets in square microchannels. *Phys. Fluids* **20**, (2008).
14. Zhao, Y., Chen, G. & Yuan, Q. Liquid-liquid two-phase flow patterns in a rectangular microchannel. *AIChE J.* **52**, 4052–4060 (2006).
15. Pohar, A., Lakner, M. & Plazl, I. Parallel flow of immiscible liquids in a microreactor: Modeling and experimental study. *Microfluid. Nanofluidics* **12**, 307–

316 (2012).

16. Gupta, A., Murshed, S. M. S. & Kumar, R. Droplet formation and stability of flows in a microfluidic T-junction. *Appl. Phys. Lett.* **94**, 1–4 (2009).
17. Lee, G. Bin *et al.* Hydrodynamic focusing for a micromachined flow cytometer. *J. Fluids Eng. Trans. ASME* **123**, 672–679 (2001).
18. Steegmans, M. L. J., De Ruiter, J., Schroën, K. G. P. H. & Boom, R. M. A descriptive force-balance model for droplet formation at microfluidic Y-junctions. *AIChE J.* **56**, 2641–2649 (2010).
19. Liu, M., Wang, S., Wei, Z., Song, Y. & Jiang, L. Bioinspired design of a superoleophobic and low adhesive water/solid interface. *Adv. Mater.* **21**, 665–669 (2009).
20. Nguyen, H. A. D., Lee, J., Kim, C. H., Shin, K. H. & Lee, D. An approach for controlling printed line-width in high resolution roll-to-roll gravure printing. *J. Micromechanics Microengineering* **23**, (2013).
21. Young, T. An essay on the cohesion of fluids. *Philos. Trans. R. Soc. London* **95**, 65–87 (1805).
22. Sun, Y., Mayers, B., Herricks, T. & Xia, Y. Polyol synthesis of uniform silver nanowires: A plausible growth mechanism and the supporting evidence. *Nano Lett.* **3**, 955–960 (2003).
23. Lhassani, A., Tronel-Peyroz, E. & Bennes, R. Contact angles of a binary liquid mixture on a hydrophobic surface and their interpretation with Neumann's equation of state. *Colloids Surfaces A Physicochem. Eng. Asp.* **75**, 105–109 (1993).
24. Brauner, N., Rovinsky, J. & Moalem Maron, D. Determination of the interface curvature in stratified two-phase systems by energy considerations. *Int. J. Multiph. Flow* **22**, 1167–1185 (1996).
25. Choi, S., Lee, M. G. & Parka, J. K. Microfluidic parallel circuit for measurement of hydraulic resistance. *Biomicrofluidics* **4**, 1–9 (2010).
26. Kim, D., Chesler, N. C. & Beebe, D. J. A method for dynamic system characterization using hydraulic series resistance. *Lab Chip* **6**, 639–644 (2006).
27. Pasquier, S., Quintard, M. & Davit, Y. Modeling two-phase flow of immiscible fluids in porous media: Buckley-Leverett theory with explicit coupling terms. *Phys. Rev. Fluids* **2**, (2017).
28. Deegan, R. D. *et al.* Capillary flow as the cause of ring stains from dried liquid drops. *Nature* **389**, 827–829 (1997).

29. Deegan, R. D. *et al.* Contact line deposits in an evaporating drop. *Phys. Rev. E* **62**, 756–765 (2000).
30. Davis, S. H. Moving contact lines and rivulet instabilities. Part 1. The static rivulet. *J. Fluid Mech.* **98**, 225–242 (1980).
31. Schiaffino, S. & Sonin, A. A. Formation and stability of liquid and molten beads on a solid surface. *J. Fluid Mech.* **343**, 95–110 (1997).

# Chapter 4 - Ligand Exchanged Silver Nanowire for Conductivity Improvement

## 4.1 Introduction

The development of printed electronics has created the possibility of fabricating electronics devices at high throughput and low costs.[1,2] In order for this to be realized, the printed features must have sufficiently good material properties to ensure that the devices can perform well. For the printing of conductive structures, metallic nanomaterial-based inks are commonly used as they can achieve high conductivities.[3]

As reviewed in Chapter 2, AgNWs is a good candidate for forming highly conductive features. However, the main challenge is the high junction resistance between nanowires due to the presence of insulating PVP ligands. Usually, some form of post-treatment is required to improve the electrical properties of AgNW structures.[4–8] However, post-treatments may sometimes encounter the issue of volume shrinkage when the nanomaterials become sintered together. This may lead to the printed metallic structures rupturing or having weak mechanical properties.[9] The use of sinter-free inks is a convenient solution to circumvent these problems and is also beneficial to the throughput of the fabrication process.[9–11]

The aim of this chapter is to formulate a post-treatment free conductive silver nanowire ink by replacing the bulky PVP ligands on the as-synthesized nanowires with ligands that will improve the charge transport across neighbouring nanowires. The focus will be on the use of bidentate ligands which should act as linker molecules between neighbouring nanowires. This strategy has been attempted in nanoparticle films usually as a post-treatment.[12] It is reported that linkers can improve inter-particle distances and coordination.[13] In this study,

ligand exchange will be performed prior to film deposition to avoid the need for any post-treatments and also minimizes any possible chemical changes on underlying layers of materials.

In addition, it is hypothesized that the geometry of the ligand molecule is an important factor which affects their effectiveness as linkers in nanowire films. As AgNWs are typically much larger and have lower curvatures than nanoparticles, there is a possibility for multiple functional groups from the same ligand molecule to bind onto a single AgNW due to bond rotation as shown in Figure 4-1ai. This phenomenon has been reported more frequently for self-assembled monolayers on planar metallic surfaces.[14] This is an undesirable configuration for linking molecules since both functional groups are bonded to the same nanowire.

For bidentate ligands to be effective linkers, their two binding groups should be located at the terminal ends of the molecule and be linked by a rigid molecular structure to ensure that the two binding groups are oriented away from each other. Therefore, there should be some degree of carbon unsaturation in the molecules in the form of C=C double bonds or aromatic ring structures as shown in Figure 4-1aii. On the other hand, molecules without these unsaturated carbon structures are prone to bond rotations which may allow the two binding groups to interact with the same nanowire.

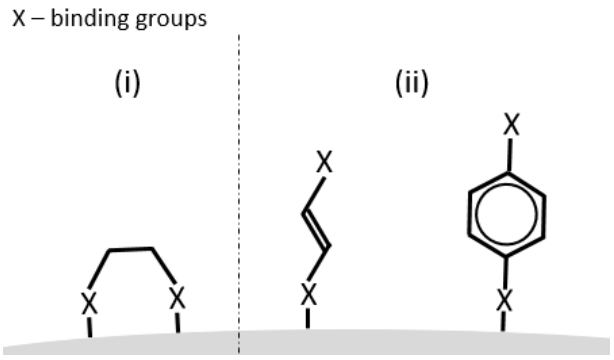



Figure 4-1: Schematics of different ways bidentate ligands can bind onto a nanowire surface: (i) both binding groups on ligand are bound to the same nanowire due to bond rotation in single bonds. (ii) unsaturated bonds in molecule allow ligand to remain rigid.

### 4.1.1 Choice of ligands

To test the hypothesis, ligands shown in Figure 4-2 were used in this part of the study. A mixture of saturated and unsaturated, monodentate and bidentate ligands were used for comparison. From this point on, we will refer to saturated ligands as flexible ligands and unsaturated ligands as rigid ligands. The use of organic acids is the primary focus in this study as they are mostly non-toxic and harmless chemicals. This may be important as these materials could eventually be used in wearable electronic devices and therefore should minimize the usage of toxic chemicals. Fumaric acid was used as the primary acid ligand as it is the smallest dicarboxylic acid with a C=C double bond. Succinic acid and crotonic acid were therefore used as the unsaturated and monodentate comparison respectively. In addition, amine ligands were also used to verify the observations from the acid ligands. Due to the lack of availability of chemicals, diamines with C=C double bonds were not accessible. Therefore, the aromatic diamine p-phenylenediamine (PDA) was used as the primary amine ligand. Aniline would be used as the monodentate comparison and 1,6-diaminohexane (DAH) would be used as the flexible diamine ligand.

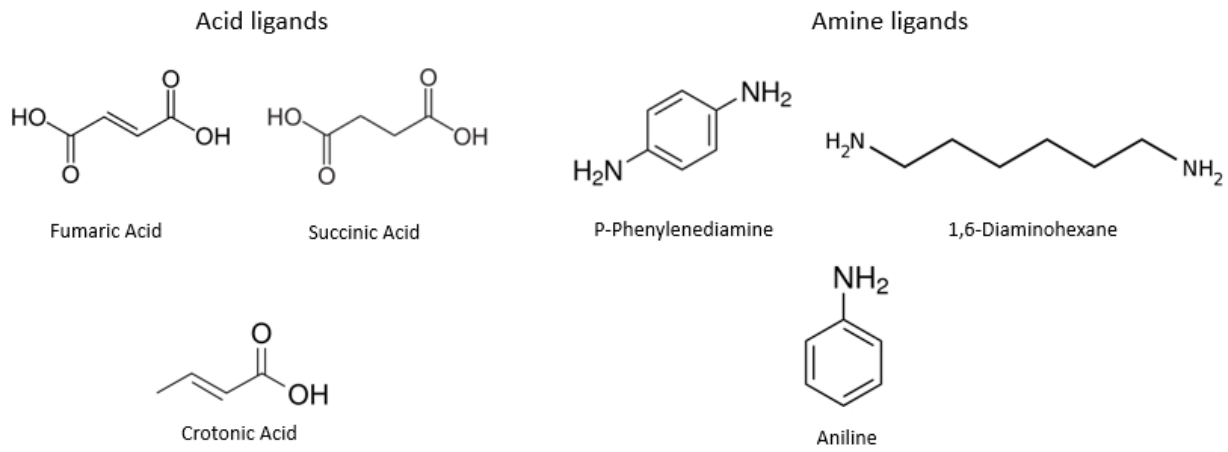



Figure 4-2: The different acid and amine ligands used in this study. A mixture of saturated (flexible), unsaturated (rigid), monodentate and bidentate ligands are used.

### 4.1.2 Ligand Exchange Reaction

In order to attach the new ligands onto the silver nanowires, a ligand exchange reaction was done to replace the existing PVP ligands. Since PVP and the new ligands are all hydrophilic compounds, single-phase ligand exchange was performed. Ligand exchange reactions generally follow a Nernst distribution with the two different ligands settling into an equilibrium between being dissolved in the solvent and being adsorbed on the nanowire surface.[15,16] The overall equilibrium depends on a multitude of factors like the ligand-AgNW, ligand-ligand and ligand-solvent interactions.[17] In general, it is difficult to achieve complete ligand exchange in single phase reactions unless the new ligand has a much stronger binding strength to the nanowire than the old ligand, which is unlikely for the ligands used in this study.[18] However, this may turn out not to be an issue as complete ligand exchange in AgNWs would not be desirable either since the stabilizing ligands are still needed to maintain colloidal stability of the AgNWs the ink.[19] Therefore, the aim is to achieve a partial ligand exchange to have a mixture of stabilizing PVP ligands and charge transport boosting small ligands on the AgNWs to achieve a compromise between stability and conductivity. Figure 4-3 shows the schematics of how the ligand exchange would lead to conductivity improvement between nanowires. Areas which undergo ligand exchange

can come into closer contact with neighbouring nanowires and improve electrical contact. The functional groups on the surface of the ligand shell can help to coordinate this linkage as they can usually form strong hydrogen bonds with each other.

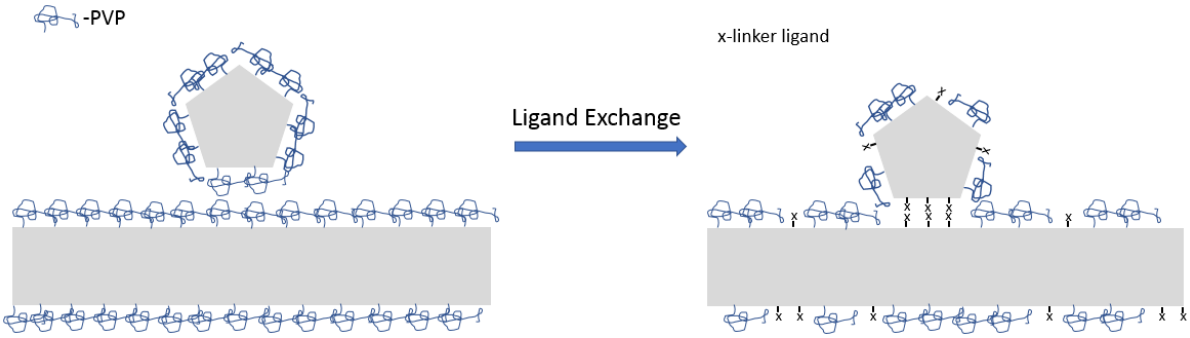



Figure 4-3: Schematic diagram showing the potential mechanism for improvement in nanowire contact after ligand exchange.

## 4.2 Materials and Methods

### 4.2.1 Materials

Silver nitrate, ethylene glycol (EG), copper (II) chloride dihydrate, polyvinylpyrrolidone with average molecular weight of 55000, fumaric acid, succinic acid, crotonic acid, p-phenylenediamine, 1,6-diaminohexane, aniline and hydrochloric acid were purchased from Sigma Aldrich.

Silver nanowires used in this study were synthesized via the polyol process.[20] In a typical synthesis, 0.1811 g of silver nitrate was dissolved in 1.5 ml of ethylene glycol. In a separate glass vial, 0.8 g of PVP was dissolved in 20 ml of ethylene glycol and heated to 150 °C with magnetic stirring. 20 µL of a 0.15 M aqueous copper (II) chloride solution was then added to the PVP solution. Once the solution was mixed homogenously, the silver nitrate solution was added and the reaction mixture was left for 1 hour. After the reaction, the nanowires were washed with methanol and subsequently centrifuged at 2500 rpm for 10 mins. This

was repeated 3 times before finally re-dispersing the nanowires into methanol to form a suspension.

### 4.2.2 Ligand Exchange of Silver Nanowire

To facilitate the ligand exchange reaction, the methanolic AgNW suspension was first diluted to 1 mg/ml and the new ligands were added into the suspension. The dilution of the AgNW suspension was to encourage the dissolution of PVP into the solvent to give the new ligands easier access onto the AgNWs. Typically, 6 ml of the diluted suspension is used for each sample. The ligands are then added to the suspension based on a specific molar ratio with respect to the silver in the suspension. This ratio is denoted by $L$. For each types of ligands, an amount corresponding to $L$ = 1, 2.5 and 5 were added to the AgNW suspensions to create suspensions with different degree of ligand exchange. Table 4-1 shows the amount of ligands added to each sample at different $L$ values. The resultant mixtures were magnetically stirred and kept overnight for 24 hours. The suspensions were then centrifuged at 2500 rpm for 10 mins. The supernatant was discarded and the remaining sediment was re-dispersed in different solvents to form suspensions for different uses. To make the printing ink, the ligand exchanged AgNWs (LE-AgNWs) were redispersed in a solution of deionized (DI) water with 15 wt% EG to create a printing ink with AgNW concentration of 6 mg/ml. Some of the LE-AgNWs were also redispersed in methanol with AgNW concentration of 1 mg/ml which will be used for making samples for FTIR and TGA. Lastly, some of the LE-AgNWs were redispersed in DI water with a concentration of 0.01 mg/ml for subsequent use for zeta potential measurements.

Table 4-1: Amount of ligands added per ml of AgNWs suspension diluted to 1 mg/ml for ligand exchange

| | Mass of ligands added for various *L* (mg) | | |
|---|---|---|---|
| Ligand | *L* = 1 | *L* = 2.5 | *L* = 5 |
| Fumaric Acid | 1.08 | 2.69 | 5.38 |
| Succinic acid | 1.09 | 2.74 | 5.47 |
| Crotonic acid | 0.80 | 2.00 | 3.99 |
| p-Phenylenediamine | 1.00 | 2.51 | 5.01 |
| 1,6-Diaminohexane | 1.08 | 2.69 | 5.39 |
| Aniline | 0.86 | 2.16 | 4.32 |

### 4.2.3 Fabrication of Silver Nanowire Film

The films were fabricated using solvodynamic printing. The properties of the ink used is shown in Table 4-2. The properties were characterized using the same techniques as in Chapter 3. Hexane was used as the carrier solvent. Glass substrates were cleaned by ultrasonicating the substrate in decon soap solution, DI water, acetone and isopropanol sequentially at 40 °C for 5 min each. The nominal ink and carrier solvent flow rates were fixed at 10 μl/min and 20 μl/min respectively. The substrate velocity was set at 5 mm/s. At these printing conditions, the printed line width is approximately 1.0 mm. A higher ink flow rate and lower substrate velocity was used here to improve the throughput of the printing. Resolution is compromised as it is less important for printing films. To improve the control of the ink printing, an additional stage is installed to the solvodynamic printer to control the substrate movement in two dimensions to print a uniform film. The stages were programmed to move the substrate below the stationary nozzle to print lines which are adjacent and in contact with each other to form a two-dimensional film. The schematic of the programmed movement is shown in Figure 4-4a. Several layers are printed to increase the amount of AgNWs on the substrate. Typically, three layers are printed for each film. The AgNW films were dried on a hotplate at 90 °C for 5 min after printing each layer. The film was dried for

an additional 10 mins after printing the last layer to ensure complete drying. Four samples were printed for each type of ligands used, as well as the control AgNWs which did not undergo any ligand exchange.

Table 4-2: Properties of aqueous silver nanowire ink used to fabricate films

| EG content (wt%) | AgNW content (mg/ml) | Viscosity (mPa·s) | Surface Tension (mN/m) | Density ($g/cm^3$) |
|---|---|---|---|---|
| 15 | 6.0 | 0.978 | 71.5 | 1.02 |

In the previous chapter, solvodynamic printing was investigated as a high resolution printing technique. In this chapter, it was used to fabricate AgNW films. The large nozzle size of the solvodynamic printer makes it well suited for printing AgNWs with reduced risk of nozzle clogging. The presence of the carrier solvent tends to make the drying occur more evenly compared to simple drop casting. An example of this effect is shown in Figure 4-4b. The solvodynamic printed film has a generally more even distribution of AgNWs. During printing, the carrier solvent appeared to be more concentrated around the edges of the film. This caused a small area around the edge of the film which appeared to have slightly lower concentration of AgNWs.

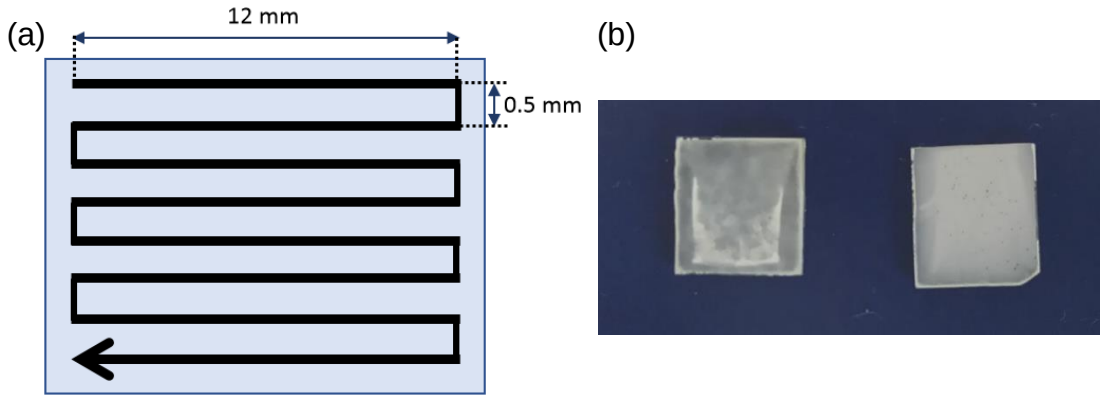



Figure 4-4: (a) Schematic of the programmed stage movement for printing AgNW film on a glass substrate. The arrow represents the movement of the printer nozzle relative to the substrate achieved by the movement of the X-Y translational stage. (b) Comparison between a drop casted (left) and solvodynamic printed (right) silver nanowire film.

### 4.2.4 Characterization

#### 4.2.4.1 Structure of Ligand Shell on Silver Nanowires

The characterization can be divided into two main groups. The first involved the characterization of the ligand shell of the LE-AgNWs. The identity, quantity and the configuration of the ligands on the AgNWs were characterized.

The identities of the ligands present on the nanowires were characterized by Fourier Transform Infrared Spectroscopy (FTIR). Each ligand molecule has a fingerprint FTIR spectra, and by comparing the spectra with the LE-AgNW spectra, the presence of the different ligands on the LE-AgNWs can be verified. Attenuated Total Reflectance Fourier Transform Infrared Spectroscopy (Varian Excalibur FTS 3500 FT-IR Spectrometer) was performed on LE-AgNW films for wavenumbers between 500 and 4000 $cm^{-1}$. The films were made by drop casting 0.1 ml of 1 mg/ml methanolic LE-AgNW suspension on a piece of 1.3 cm x 1.3 cm glass substrate. The corresponding methanolic solutions of the pure ligands were also drop casted on glass slides and characterized for comparison. Each sample was characterized 4 times to ensure that the characteristic peaks detected in the sample are consistent in all measurements.

FTIR is effective in identifying the presence of molecules within the samples but does not give much quantitative data. Therefore, thermogravimetric analysis (TGA) (Perkin Elmer TG/DTA 6300) was done. TGA can provide information on the relative amounts of different organic components within the sample. For each measurement, approximately 10 mg of dry AgNWs were used. The AgNWs were prepared by drop casting the AgNW suspension onto a microscope slide and letting it dry in ambient conditions. A lid was placed on top of the drying sample to minimize impurities falling into the suspension. After the AgNWs have

completely dried, they were scraped off the microscope slide with a spatula and collected. This was repeated until approximately 10 mg of dried AgNWs have been collected for each type of AgNWs. The samples were placed in a crucible into the TGA and heated at 10 °C/min till 550 °C under nitrogen environment. From the TGA results, we can verify the occurrence of the ligand exchange by monitoring the relative amounts of PVP in the samples and the occurrence of new mass loss events at different temperatures.

Lastly, the configuration of the acid and amine ligands on the nanowires were deduced using zeta potential measurements. The zeta potential of a nanomaterial suspension is an indication of the polarity and magnitude of surface charges on nanomaterials.[21] Since nanomaterials are usually covered by ligands, its surface charge is largely determined by the types and density of ligands which make up the exterior of the ligand shell.[22] One reason why acid and amine ligands were used in this study was that they could generate charged groups like $COO^-$ and $NH_3^+$ on the surface of the ligand shell which could then be detected as a change in zeta potential. Therefore, the zeta potential here is effectively an indication of the density of unbound acid or amine groups at the surface of the AgNWs which is available for linking to occur. A higher magnitude in zeta potential indicates more potential linking sites on the AgNWs.

The zeta potential of the AgNW suspensions were characterized using Malvern Zetasizer Nano ZS. The LE-AgNWs were diluted to 0.01 mg/ml in DI water. To obtain an accurate gauge of the density of unbound acid and amine groups on the LE-AgNWs, the carboxylic acids and amines should be largely ionized at the pH of the solvent. By default, the use of deionied water as the solvent makes the pH approximately 7. The degree of ionisation of the ligands then depends on their pKa, which are listed in Table 4-3. The acid ligands have

pKas of approximately 3.03-4.82. This means that at pH 7, at least 99% of all the carboxylic acid groups will be ionized for all three ligands. On the other hand, the amine ligands have a wider spread of pKa values. PDA has the lowest at 7.82 while the others have much higher pKas. This could be an issue as only about 87% of PDA ligands will be ionised at pH 7 while more than 99% of the other three ligands would be ionised. To make the comparison more accurate, the pH for the amine LE-AgNWs were adjusted to approximately pH 5 by the addition of diluted hydrochloric acid to make the $H^+$ concentration $10^{-5}$ M. The solutions were loaded into a folded capillary cell using a 1 ml syringe. There should be no bubbles in the cell and the solution should be in contact with the electrodes at the top of the cell. 5 zeta potential measurements were performed on each samples and the average zeta potential value is obtained.

Table 4-3: pKas of the various acids and amine ligands used in the ligand exchange.

| Ligand | pKa |
|---|---|
| Crotonic Acid | 4.82 |
| Succinic Acid | 4.21 |
| Fumaric Acid | 3.03 |
| p-Phenylenediamine | 7.83 |
| Aniline | 9.30 |
| 1,6-Diaminohexane | 10.51 |

#### 4.2.4.2 Macroscopic Properties of Silver Nanowire Films

The previous set of characterizations allowed us to understand the structure of the ligands on the LE-AgNWs. Since the cross-linking at the molecular level is not directly observable, the overall macroscopic properties of the printed AgNW films were characterized and linked to the corresponding ligand structures. Firstly, the electrical property of the films was characterized by measuring their sheet resistances using a 4-point probe (Jandel cylindrical probe) with applied currents in the range between 0.1 to 5 μA. 10 measurements were taken

at random locations on each film to obtain a representative average sheet resistance. The resulting morphologies of the LE-AgNW films were characterized using scanning electron microscopy (SEM) (JEOL JSM-840F SEM). Lastly, the sintering temperatures of the AgNW films were also characterized. Since sintering involves the fusing of the nanowire junctions, any changes in the junction structures due to ligands will have a direct impact on the thermodynamics of the process and consequently the temperature at which sintering can occur. This was done by heating different AgNW films on a hotplate at different temperatures for 20 mins each at different temperatures and measuring the sheet resistances of each film after the treatment.

## 4.3 Results and Discussion

The results related to the ligand exchange reactions using different ligands will first be discussed before relating them to the macroscopic properties of the AgNW films. For the ligand exchange reaction, the ligand to Ag molar ratio used is denoted as $L$. As a start, $L$ = 5 was used during the ligand exchange. Other values of $L$ would be used in the later sections to draw the relation between the extent of ligands exchanged and the final electrical properties of the AgNW films.

### 4.3.1 Fourier Transform Infrared Spectroscopy

FTIR was done on the nanowires to verify if the ligand exchange had occurred. In these spectra, the key observations made were whether matching peaks in the pure ligand spectra were also observed in the LE-AgNW spectra. In addition, slight shifts in wavenumbers may occur due to the bonding of the ligands onto the AgNWs which changes the bond stereochemistry and the resultant vibration energetics of the bonds.

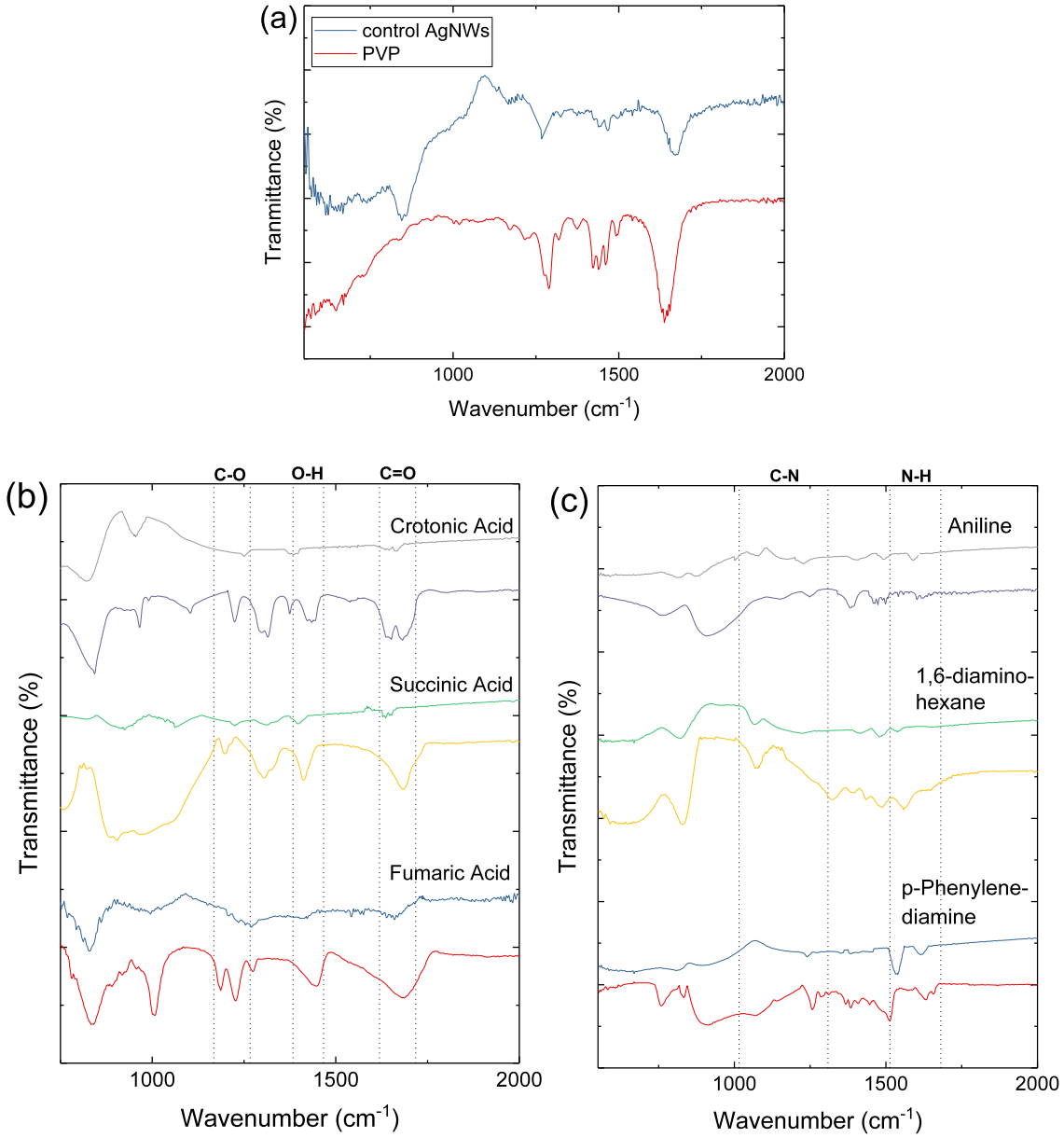



Figure 4-5: FTIR spectra of: (a) PVP and control AgNWs, (b) acid ligands and their corresponding LE-AgNWs. In each pair of spectra, the one below is the spectrum of the pure ligand and the one on top is the spectra of the LE-AgNWs. (c) Corresponding spectra of amine ligands and their LE-AgNWs. Dotted lines show regions containing characteristic peaks corresponding to certain bonds present in the sample.

Figure 4-5a shows the FTIR spectra of PVP and the control AgNW sample. Similar peaks were observed in the two spectra, showing the presence of PVP in the control AgNW sample. Another observation was that the C-N stretch and C=O stretch vibrational modes had their wavenumbers shifted from 1290 and 1637 $cm^{-1}$ to 1267 and 1670 $cm^{-1}$ respectively. The

shifts in the peaks were likely to be due to the bonding between the amide group in the PVP molecule with the surface of the silver.[23]

Figure 4-5b shows the FTIR spectra for the acid ligands with their respective LE-AgNWs. The LE-AgNWs spectra generally showed some similar peaks that were present in the spectra of the pure ligands which suggests the presence of the new ligands in the LE-AgNW samples. The main peaks to look out for are those which correspond to particular functional groups in the acid and amine ligands as highlighted in the figures. Table 4-4 lists some of the important distinguishing FTIR peaks observed that corresponded to the functional groups present in the ligands. Peaks corresponding to the C-O stretch, C=O stretch and O-H bend modes were observed in the spectra of all the acid LE samples, showing the presence of carboxylic groups. $=CH_2$ bending modes could also be observed in the fumaric acid and crotonic acid which gives further evidence that the ligands were successfully exchanged onto the AgNWs. Upon further comparison, it was found that the C-O and C=O stretch peaks were slightly shifted in all the acid LE-AgNW samples compared to the spectra of the pure ligands. This gives evidence that the ligands were binding to the AgNWs through the carboxylic acid group. The C-O peaks were consistently shifted to higher wavenumbers while the C=O peaks were shifted to lower wavenumbers. Overall, the peak separation between these two vibrational modes was more than 200 $cm^{-1}$. This meant that the acid ligands were binding to the silver surface via the monodentate mode, whereby the oxygen on the C-O bond was bonded to one single silver atom.[24]

Table 4-4: Peak positions of defining functional groups in acid ligands and their corresponding LE-AgNWs

| Ligand | IR peaks from pure ligand ($cm^{-1}$) | IR peaks from ligand exchanged nanowires ($cm^{-1}$) | Corresponding vibrational mode |
|---|---|---|---|
| Fumaric Acid | 1006 | 995 | =C-H bend |
| | 1240 | 1266 | C-O stretch |
| | 1440 | 1409 | O-H bend |
| | 1683 | 1657 | C=O stretch |
| Succinic Acid | 1197 | 1226 | C-O stretch |
| | 1413 | 1397 | O-H bend |
| | 1685 | 1631 | C=O stretch |
| Crotonic Acid | 966 | 947 | =C-H bend |
| | 1220 | 1252 | C-O stretch |
| | 1425 | 1382 | O-H bend |
| | 1679 | 1646 | C=O stretch |

Table 4-5: Peak positions of defining functional groups in amine ligands and their corresponding LE-AgNWs

| Ligand | IR peaks from pure ligand ($cm^{-1}$) | IR peaks from ligand exchanged nanowires ($cm^{-1}$) | Corresponding vibrational mode |
|---|---|---|---|
| 1,6-Diaminohexane | 1078 | 1087 | C-N stretch |
| | 1558 | 1525 | N-H bend |
| p-Phenylenediamine | 1261 | 1238 | C-N stretch |
| | 1638 | 1614 | N-H bend |
| Aniline | 1249 | 1230 | C-N stretch |
| | 1602 | 1588 | N-H bend |

The corresponding data for the amine ligands is presented in Figure 4-5c and Table 4-5. In this case, the presence of C-N stretch and N-H bend vibrational peaks in the FTIR spectra showed the successful exchange of the amine ligands. The series of peaks within the region of 1400 to 1600 $cm^{-1}$ in the aniline and PDA sample corresponded to the vibrational modes from the benzene ring from the ligand as well. For the amine LE-AgNWs, the peak shifts were observed in both the C-N stretch and N-H bend peaks. In all samples, both the C-N stretch and N-H bend peaks were observed to decrease in wavenumber. These shifts could indicate that the bonding of the ligands to the AgNWs through the amine group. In the case for amine ligands, it is established in literature that each amine group can only bond to one single silver atom.[25]

### 4.3.2 Thermogravimetric Analysis

The FTIR results do show the presence of the new ligands in the LE-AgNWs. However, it is not clear if the new ligands actually replaced some of the pre-existing PVP or simply bound onto the existing PVP ligand shell. In order to distinguish between the two scenarios, as well as to obtain some quantification of the degree of ligand exchange, TGA was done on the different LE-AgNW samples. As different ligands generally decomposed at different temperatures, the weight loss observed in the TGA at different temperatures would confirm that a different ligand was present. The relative loss in mass at different temperatures can also provide some information on the relative amounts of different ligands that may be present in the samples.

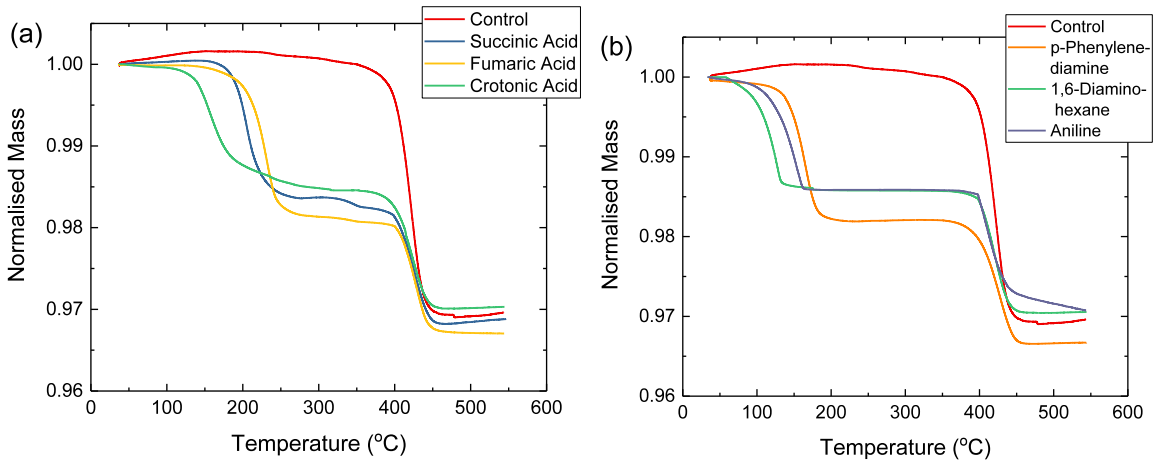



Figure 4-6: Normalised TGA curves for (a) acid ligand-exchanged AgNWs and (b) amine ligand-exchanged AgNWs.

Table 4-6: Decomposition temperatures, molar ratios of new ligands and PVP to silver in the different LE-AgNWs

| Sample | Decomposition Temperature (°C) | Molar ratio | |
|---|---|---|---|
| | | New ligand:Ag | PVP:Ag |
| Control | 425 | - | 0.0311 |
| Fumaric Acid | 233 | 0.0178 | 0.0143 |
| Succinic Acid | 206 | 0.0143 | 0.0147 |
| Crotonic Acid | 161 | 0.0187 | 0.0142 |
| p-Phenylenediamine | 171 | 0.0164 | 0.0147 |
| Aniline | 131 | 0.0159 | 0.0143 |
| 1,6-Diaminohexane | 159 | 0.0120 | 0.0149 |

Figure 4-6a and b shows the TGA results for the acid and amine ligands respectively. The TGA curve for the control sample showed a single mass loss of 3.1 % at 425 °C, corresponding to the decomposition of PVP on the AgNWs. These values are consistent with those reported in previous studies on PVP capped AgNWs.[26] For all the other LE-AgNW samples, an additional mass loss was observed at a lower temperature. This additional mass loss showed the presence of the new ligands within each sample. The mass loss occurred at a different temperature for each sample as each ligand would have its own decomposition temperature based on the type of structures present. In general, the decomposition of the new ligands occurred at lower temperatures than PVP which makes sense as they are smaller organic molecules compared to PVP. The amount of mass loss corresponding to the new ligands were also different in different samples. At the same time, the mass loss due to PVP was still observed, but the amount of mass loss was decreased.

From the data, the relative molar ratios between the ligands and silver were calculated and tabulated in Table 4-6. For PVP, the relative molecular mass of each individual monomer unit was used to give a better comparison as each monomer unit corresponds to one binding

unit on the silver. By comparing the molar ratio of PVP to silver in each of the samples, it is clear that the amount of PVP present in the AgNW did decrease after the ligand exchange reaction. This gives solid evidence to show the occurrence of the ligand exchange instead of the simple addition of ligands onto the PVP.

Comparing between the results for the acid ligands, it can be seen that the amount of crotonic and fumaric acid present in the LE-AgNWs were similar while there is less succinic acid being exchanged onto the nanowires. This observation is consistent with the proposed schematics in Figure 4-1. Each crotonic acid molecule can only bind to one silver atom due to its monodentate nature. At the same time, fumaric acid despite being bidentate, was effectively monodentate to a single nanowire due to its rigid structure. Therefore, similar amounts of crotonic acid and fumaric acid were exchanged onto the nanowires. As for succinic acid, their flexible nature due to bond rotation of the C-C bonds allowed them to behave as both monodentate and bidentate ligands on a single nanowire depending on factors like availability of binding sites and their localized concentration in the solution. Since some of the succinic acid molecules can take up two binding sites on the silver surface, fewer molecules were exchanged onto the AgNWs as observed.

A similar observation can also be made with the amine ligands. Aniline is monodentate as it only has a single amine group. PDA is a rigid ligand due to the benzene ring which makes it impossible for both amine groups to bind on the same nanowire. DAH is the only molecule with rotatable bonds which allows it to be both monodentate and bidentate. Once again, the amount of aniline and PDA on the LE-AgNWs are similar while the amount of DAH is comparatively less. From these results, it can be foreseen that succinic acid and DAH will be less effective linker ligands than the rigid bidentate ligands as the ligands which have

both of their functional groups bound to the same nanowire will not be able to participate in the linking interaction. Further verification of this concept will be done in the subsequent section.

### 4.3.3 Zeta Potential Measurements

In this study, the zeta potential measures the density of unbound linking groups on the surface of the AgNWs. Following the conjecture in the TGA results, the rigid bidentate ligands should have the highest zeta potential since each ligand creates one free charged groups on the surface of the ligand shell around the nanowire while the other ligand will have a smaller effect. In this section, AgNW samples which had undergone ligand exchange at lower ligand to Ag ratio of $L$ = 1 and $L$ = 3 to produce samples with different degrees of ligand exchange were also analysed.

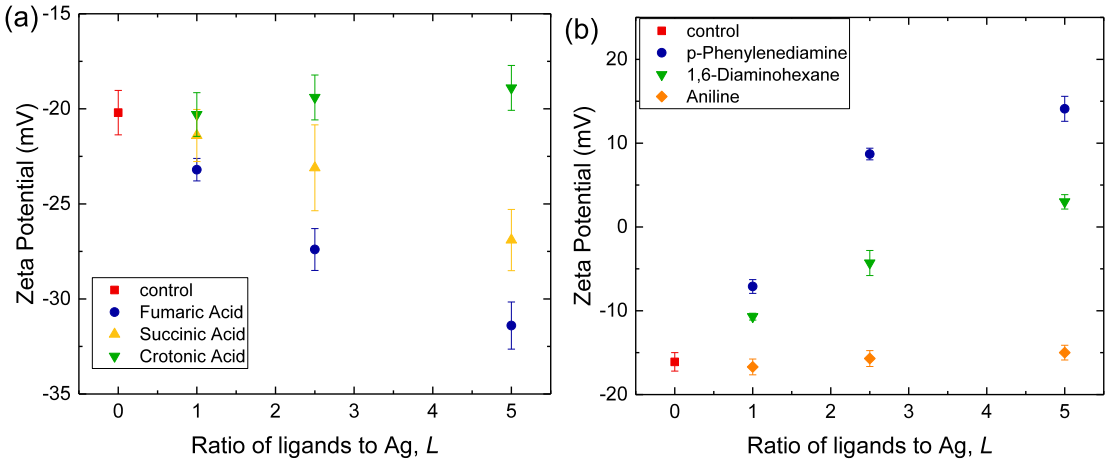



Figure 4-7: Variation of zeta potential of AgNWs when subjected to different degrees of ligand exchange using (a) acid ligands and (b) amine ligands.

Figure 4-7a and b shows the measured zeta potentials of the different samples for the acid and amine ligands respectively. The results that the control AgNW sample with pure PVP ligands showed a zeta potential of -20.1 mV at pH 7. The LE-AgNW using $L$ = 5 corresponds to the samples previously analysed by TGA. The fumaric sample had the

strongest negative zeta potential, followed by succinic acid and crotonic acid. This is consistent with the initial hypothesis. Figure 4-8 illustrates simplified schematics of the configuration of the new ligands on the nanowire surface given the observed results. Crotonic acid which is represented in Figure 4-8a has their only carboxylic acid group bound to the nanowire. Therefore, it does not create any additional unbound charged groups on the nanowire surface. In fact, the zeta potential became slightly more positive, likely due to the removal of the elecron-rich amide groups present in PVP. Both succinic and fumaric acid, represented by Figures 4-8b and c have a secondary carboxylic acid group which can form charged carboxylate groups on the nanowire surface, causing their zeta potential to be more negative than the control AgNW.

The LE-AgNWs with fumaric acid showed a more negative zeta potential of -32.0 mV compared to -26.7 mV in the succinic acid sample. This can either be explained by the hypothesised flexible and rigid nature of the ligands or simply due to having fewer succinic acid ligands on the AgNWs. From the TGA results for $L$ = 5, the relative amount of fumaric acid to succinic acid in their respective LE-AgNW samples was 0.0178:0.0143, which reduces to 1:0.80.

The two different scenario can be distinguished by considering the mathematical relation between zeta potential and the effective surface charge density, $\sigma_{eff}$ as described by the Gouy-Chapman equation:[27]

$$\sigma_{eff} = \sqrt{8cN_a\varepsilon_r\varepsilon_0 k_b T}\sinh\left(\frac{q\xi}{k_b T}\right) \quad (4\text{-}1)$$

where $c$ is the ionic concentration in the solution, $N_a$ is the Avogrado's constant, $\varepsilon_r$ is the dielectric constant of the solution, $\varepsilon_0$ is the permittivity of vacuum, $k_b$ is the Boltzmann's

constant, $T$ is the temperature of the system, $q$ is the electronic charge and $\xi$ is the zeta potential. Since the surface charge density varies linearly with the density of charged groups on the the nanowire surface, Equation 4-1 can be used with experimental results of the fumaric acid sample to extrapolate the zeta potential of samples with varying amounts of rigid ligands. Scaling down the experimentally obtained $\sigma_{eff}$ for the fumaric acid sample by 0.8 gave a zeta potential of -29.7 mV. This is still more negative compared to the -26.7 mV observed in the actual succinic acid sample. Therefore, it seems that the lower charge in the succinic acid LE-AgNWs was not just due to having fewer ligands but likely to be due to the flexible nature as hypothesized and illustrated in Figure 4-8 b and c.

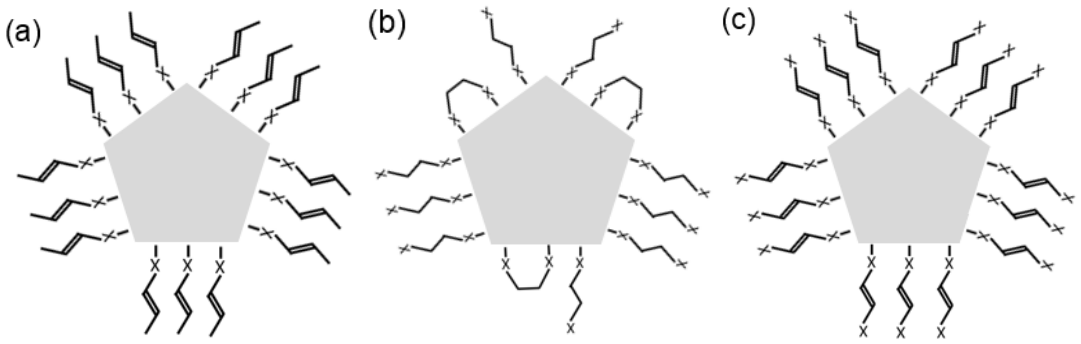



Figure 4-8: Simplified schematics of arrangement of new ligands on nanowires without consideration of PVP for: (a) monodentate ligands, (b) bidentate flexible ligands and (c) bidentate rigid ligands.

The results from the amine ligands showed a similar observation. The zeta potential of the control AgNW sample at pH 5 is -16.2 mV. The lower magnitude was most likely caused by the presence of additional ions in the solution used to adjust the pH which reduced the magnitude of zeta potentials.[28] For the LE-AgNWs, all samples aside from the aniline had a much more positive zeta potentials due to the presence of unbound positively charged $NH_3^+$ groups. The observed charge in PDA was much higher than that in DAH, which is a similar observation compared to the acid ligands. In this case, the ratio of PDA to DAH in

their respective sampels is 1:0.73. Using equation 4-1 again, scaling down $\sigma_{eff}$ in the PDA sample by 0.73 yielded a zeta potential of 5.87 mV. This is once again higher than the observed zeta potential of 3.2 mV in the DAH sample. These results support the hypothesis that the geometry of the ligand plays an important role in how the ligands can be attached to the nanowires.

Comparing samples with different *L*, the trend observed is that the there is less change in zeta potential for samples which used a lower concentration of ligands during the ligand exchange reaction. This confirms that samples undergoing ligand exchange with a lower ligand concentration have a lower extent of ligands exchanged. This will be useful when the electrical properties of the films made with different LE-AgNWs are studied in the next section.

### 4.3.4 Electrical Properties of Ligand Exchanged Nanowire Films

In this section, the effect of the different ligands on the overall electrical properties of the AgNW films is studied. In particular, the relation between the density of linking groups on the nanowires and the resultant electrical conductivity is of interest.

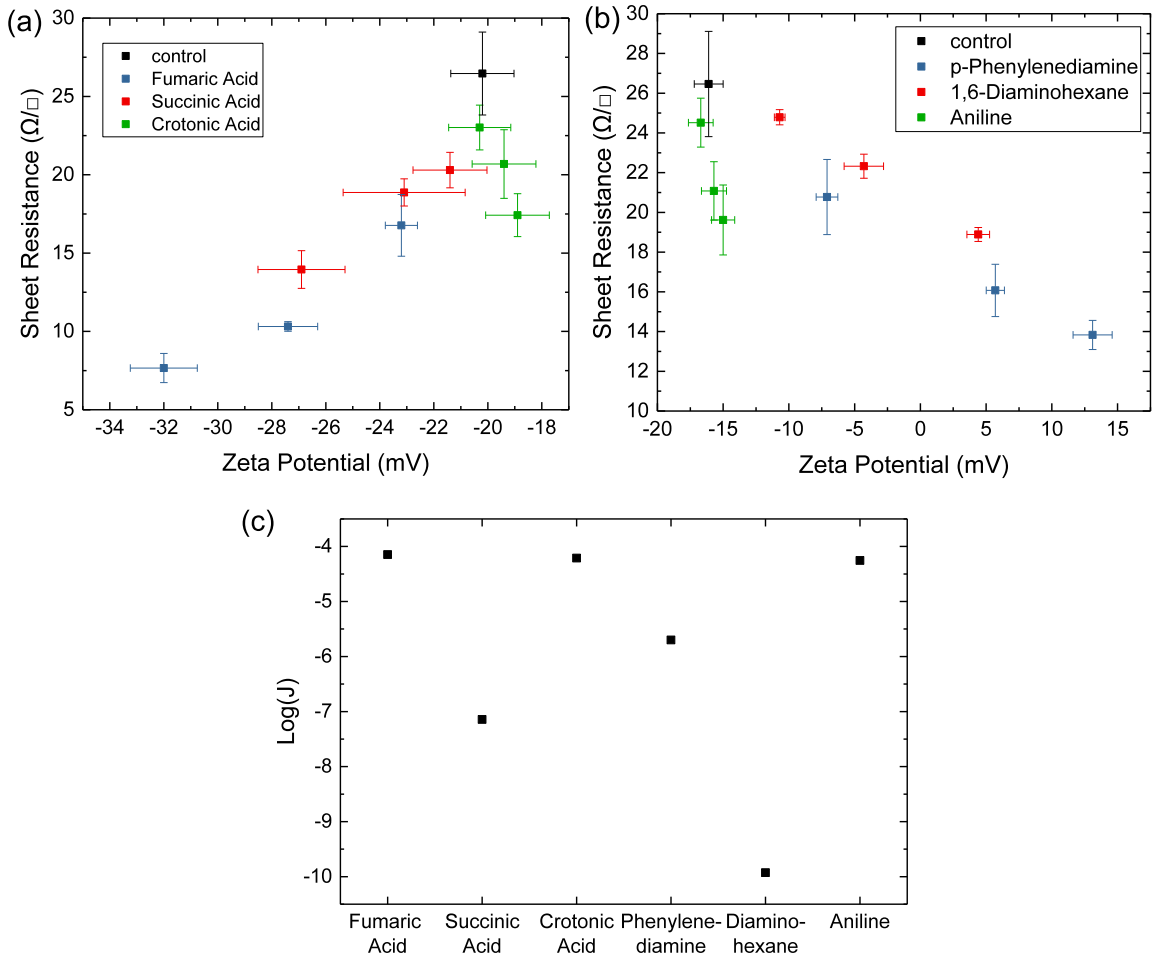



Figure 4-9: Variation in sheet resistances of AgNW films with zeta potential using different types of ligands for (a) acid ligands and (b) amine ligands. (c) Plot of calculated log of tunneling current density, *J* at the metal-ligand-metal junction for the different ligands.

Figure 4-9a and b shows the variation of sheet resistances of the AgNW films with their zeta potentials for acid and amine ligands respectively. As a baseline comparison, the films made using the control AgNWs achieved a sheet resistance of 26.5 Ω/□. Conversely, all films made using acid or amine LE-AgNWs exhibited a lower sheet resistance than the control sample. In general, the monodentate ligands showed higher sheet resistances than the bidentate ligands. This shows that bidentate ligands are more effective in improving conductivity of AgNW films. This observation is likely to be due to the lack of linking ability in monodentate ligands. For the acid bidentate ligands, samples with a more negative

zeta potential showed a greater degree of conductivity improvement. The equivalent observation can be made from the amine ligand samples whereby the more positive zeta potential corresponded to a higher conductivity. This directly shows evidence that a higher density of unbound linking groups present had a positive effect on conductivity. Therefore, the linking groups must play an important part in the conduction within the films. Since the nanowire concentrations were fixed for all the samples, and the conduction within individual AgNWs should be unaffected, it is likely that the linking groups are improving the junction resistance in the films as hypothesized. This also explains why rigid ligands perform better, since they can generally attain zeta potentials with higher magnitude, corresponding to a higher density of linking groups on the AgNWs.

To gain further insights in this observation, the charge transport through the junction across the different ligand molecules were quantified. Both tunneling and electron hopping mechanisms can occur in these metal-molecule-metal junctions. However, in this case, tunneling should be the dominant charge transport mechanism due to the small distances involved in the ligand molecules.[29] In such structures, the presence of the ligand molecule between the two metals acts as an energy barrier for charges. The theoretical tunneling current density, *J* can be expressed by the following equation:

$$J = \frac{q^2 V}{h^2} \frac{\sqrt{2mE_b}}{w_b} e^{-\frac{4\pi}{h} w_b \sqrt{2mE_b}} \tag{4-2}$$

where $q$ is electron charge, $V$ is applied voltage, $h$ is Planck's constant, $m$ is mass of an electron, $w_b$ is the width of the barrier and $E_b$ is the magnitude of the energy barrier. The width of the barrier was approximated as the separation between the crosslinked AgNWs which is roughly equivalent to the length of two ligand molecules. The applied voltage was based on the range of voltages applied by the four-point-probe onto each sample. According

to literature, the energy barrier magnitude can be approximated by the relative difference between the lowest unoccupied molecular orbital (LUMO) of the molecule and the fermi energy ($E_f$) of the metal.[30] It was reported that the LUMO-$E_f$ gap tended to be reduced when the molecule was coordinated with the metal surface.[31] However, this can only be calculated accurately using density functional theory which is not in the scope of this thesis. Therefore, the raw values of isolated LUMO energy values were used as an approximation. The LUMO energy values of the ligands were obtained from a semi-empirical quantum chemistry software called Molecular Orbital Package (MOPAC). This software combines ab-intio calculations and known experimental parameters to perform energy optimization calculations on a large range of organic molecules to predict their properties.[32,33] The values of $w_b$ and $E_b$ obtained from MOPAC are tabulated in Table 4-7. Using equation 4-2, the tunneling current in each of the metal-ligand-metal junctions were calculated. The results are tabulated in Figure 4-9c.

Table 4-7: Parameters used in the estimation of tunneling current density in each sample

| Ligand | Energy Barrier (eV) | Ligand Length (Å) | Tunneling Current Density ($\mu A/m^2$) |
|---|---|---|---|
| Fumaric Acid | 3.07 | 5.68 | 71.0 |
| Succinic Acid | 5.16 | 6.08 | 0.0719 |
| Crotonic Acid | 4.11 | 5.25 | 61.6 |
| p-Phenylenediamine | 4.28 | 5.99 | 0.667 |
| 1,6-Diaminohexane | 6.83 | 6.62 | 0.000118 |
| Aniline | 5.03 | 4.88 | 16.8 |

The calculations showed that fumaric acid, crotonic acid and aniline junctions formed the most conductive tunneling currents, followed by PDA, succinic acid and DAH. From Table 4-7, it can be inferred that crotonic acid and aniline had high tunneling currents due to their shorter ligand lengths. As for fumaric acid, its exceptionally high tunnel current was due to

its lower LUMO energy level which reduced the tunneling energy barrier. These findings are largely consistent with the measured sheet resistances. Although crotonic acid and aniline junctions should be highly conductive, the lack of linking groups made the metal-ligand-metal junction difficult to form. Therefore, there may not be many of such high conductance junctions in the actual films. This explains why the monodentate LE-AgNWs films have relatively higher sheet resistances compared to the other ligands despite their high tunneling currents. On the other hand, the bidentate ligands can form better cross-links to form the metal-ligand-metal junction.

The calculated tunneling currents are also consistent with the observed trend in sheet resistances between fumaric acid and succinic acid. It can be seen that even for samples with similar zeta potentials, fumaric acid samples still showed a lower sheet resistance than the succinic acid samples. This is consistent with the fact that fumaric acid forms more conductive junctions so that even when the density of linking groups are the same, the fumaric acid LE-AgNW films are still more conductive. The same comparison can be made between the PDA and DAH samples.

Overall, the lowest sheet resistance observed was 7.66 Ω/□, from films made by fumaric acid LE-AgNWs using $L$ = 5 during the ligand exchange. This corresponds to a reduction in sheet resistance by approximately 70%. This is a good result as such a large conductivity improvement can be achieved without the use of post-treatments.

### 4.3.5 Film Morphology

To further investigate the changes in electrical properties of the nanowire films, the morphology of the different AgNW films were examined using SEM to check if there were

any features which may lead to the improvements in conductivity. Figure 4-10 shows 3 sets of morphologies observed in different samples. Figure 4-10 a and b show a sample of the control AgNW, c and d show a sample of PDA LE-AgNW, e and f show a sample of fumaric acid LE-AgNW.

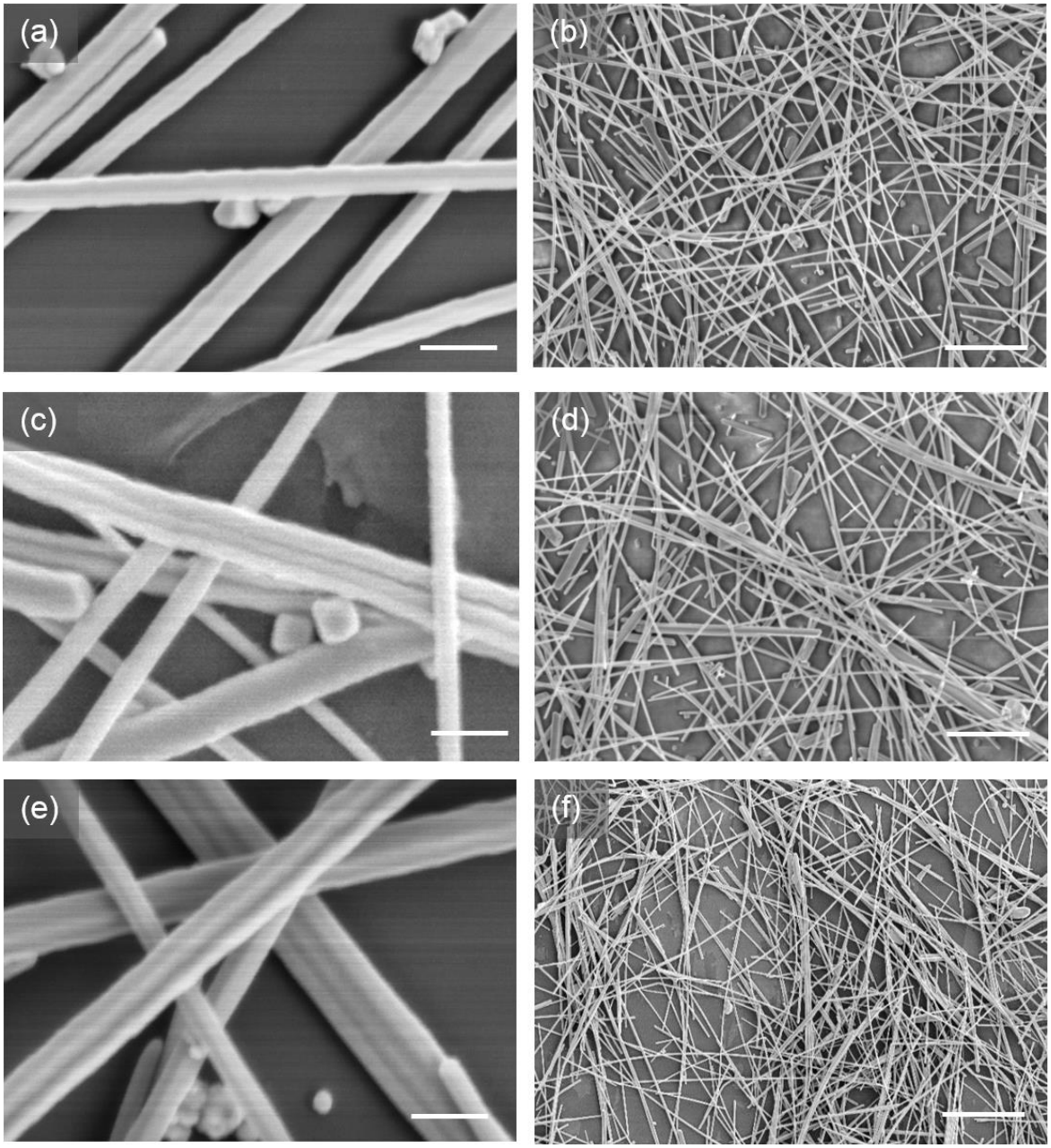



Figure 4-10: (a) and (b) High and low magnification SEM images of control AgNWs. (c) and (d) High and low magnification SEM images of PDA LE-AgNWs. (e) and (f) High and low magnification SEM images of fumaric acid LE-AgNWs. Scale bars are equivalent to 200 nm on high magnification images and 10 μm on low magnification images.

When comparing the high magnification images between the control AgNW and the two LE-AgNW samples, the occurrence of AgNW bundles were observed in the LE-AgNW films as exemplified in Figure 4-10c and e. In the control AgNW samples, the nanowires were generally better dispersed. On the other hand, it was common to find several nanowires adhering to each other side-on in the PDA and fumaric acid LE-AgNWs. The appearance of these bundled AgNW also resembled those obtained by Hui et. al. using chemical sintering.[4]

Figure 4-10b, d and f show lower magnification images of the different films made by the control, PDA and fumaric acid AgNWs. On a macroscopic scale, most of the nanowires were relatively dispersed in the control sample films. In contrast, the occurrence of these bundled AgNWs in the LE-AgNW samples form larger and longer conducting structures within the film. In Figure 4-10d, a large bundle can be observed aligning diagonally from the bottom right of the image towards the upper left part of the image. A few smaller bundles can also be seen in the upper right and bottom left area of the image. In Figure 4-10f, a large cluster containing several bundles were observed.

The occurrence of these bundled AgNW structures could be explained by the proposed ligand exchange schematics. Nanowires which have ligand exchange occurring largely along their lengths will be attracted and linked to other similar nanowires, causing them to adhere side-on. The formation of such bundled nanowires can contribute to the improvement in conductivity of the network. The junction resistances between nanowires within a bundle are greatly lowered due to their much larger area of contact. Therefore, these structures basically behave electrically as long micro-sized wires in the film. It is well known that longer wires in a percolative network are beneficial to the overall conductivity of the film

as the conduction pathways involve fewer junctions which minimizes the total contribution of junction resistance in the total resistance of the film.[34] Therefore, these large bundled AgNW structures should contribute to the reduction the sheet resistivity of the films.

### 4.3.6 Sintering Temperature

Another possible way to gain some insights into the contact at nanowire junctions is through the sintering temperature of the nanowire films. During sintering, the ligands around the nanowire partially decompose and the nanowire junctions fuse, causing a decrease in junction resistance.[35] It has been reported that the ligands present affect the sintering temperature since they directly alter the structure of nanowire junctions.[19] The presence of ligands between the nanowires at the contact junctions presents a barrier for sintering to occur. Larger ligands and denser ligand shells required more energy to remove and tend to increase the distance between the nanowires. Therefore, sintering will only occur at higher temperatures. If there are indeed linking occurring at the nanowire junctions, sintering should be able to occur at lower temperatures due to the presence of more volatile ligands and the closer nanowire separation at the junction.

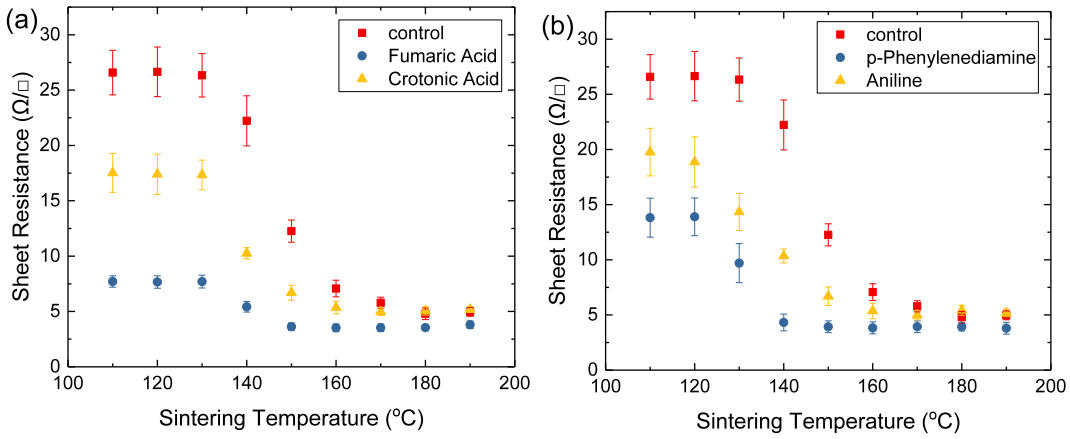



Figure 4-11: Variation in sheet resistance of AgNW films with (a) acid and (b) amine ligands when different sintering temperatures were used. Sintering times were fixed at 20 mins.

Table 4-8: Comparison of ligand decomposition and critical sintering temperatures for different LE-AgNW samples

| Sample | Ligand Decomposition Temperature (°C) | Critical Sintering Temperature (°C) |
|---|---|---|
| Control | 425 | 180 |
| Fumaric Acid | 233 | 150 |
| Crotonic Acid | 206 | 170 |
| p-Phenylenediamine | 171 | 140 |
| Aniline | 130 | 160 |

We performed sintering on the printed AgNW films via thermal annealing on a hotplate. The annealing time was fixed at 20 mins and different temperatures from 110 to 190 °C were used. The sheet resistances of the different samples were measured after the annealing and plotted in Figure 4-11. In general, higher sintering temperatures produced films with lower sheet resistances up to a certain critical temperature after which no further decrease in sheet resistance is observed as all the nanowire junctions in the film are completely fused together and sintering is complete. This critical temperature will be referred to as the critical sintering temperature. For this section, only the monodentate and bidentate rigid ligands were compared as the samples had similar ligand-PVP compositions as shown from the TGA results. This eliminates one of the determining factors of the sintering temperature and can elucidate the effect of the additional binding group in the bidentate ligand.

Table 4-8 shows the comparison of critical sintering temperatures for the different LE-AgNWs. For the control nanowire sample, the complete sintering only occurred at high temperatures of 180 °C due to the presence of the PVP ligands. Both monodentate ligands, crotonic acid and aniline had decreased critical sintering temperatures of 170 °C and 160 °C respectively due to having more volatile ligands replacing the PVP on the nanowires. The bidentate ligands showed further reductions in critical sintering temperature of 150 °C for

fumaric acid and 140 °C for the PDA sample. This is interesting as they achieved a lower critical sintering temperature despite their relatively higher decomposition temperatures as found from the TGA results. This observation complements our previous results and conjectures. The monodentate ligands should theoretically be able to form nanowire junctions with smaller nanowire separations and with more volatile ligands. However, without the coordination of the secondary binding groups, such junctions did not form easily. On the other hand, the bidentate ligands had better coordination with their secondary binding groups, leading to nanowire junctions with better contact and thus lowering the sintering temperature.

### 4.4 Conclusion

In this chapter, a conductive sinter-free AgNW ink was made via the partial ligand exchange of PVP with smaller bidentate ligands. The ligands acted as linking molecules between neighbouring nanowires and improved electrical contact between them. Therefore, the overall sheet resistance of the films was decreased. It was shown that the geometry of the molecules played an important role in the linkage of nanowires. Rigid ligands with terminal binding groups were the most effective linkers as they could maximize the number of unbound binding groups on the ligand shell to coordinate the formation of the high conductance nanowire junctions. Among all the ligands that were used, fumaric acid showed the best performance for conductivity improvement. Films made using fumaric acid ligand exchanged nanowires achieved sheet resistances of approximately 7.66 Ω/□ which is 30% of the sheet resistance of the non-ligand exchanged AgNW film. The improvement in conductivity is likely to be a combination of having closer inter-nanowire separation and matching electronic structure between the metal and ligand at the junction, and also the morphological changes in the nanowire films.

**4.5 References**


1. Kamyshny, A. & Magdassi, S. Conductive nanomaterials for 2D and 3D printed flexible electronics. *Chem. Soc. Rev.* **48**, 1712–1740 (2019).
2. Wu, W. Inorganic nanomaterials for printed electronics: A review. *Nanoscale* **9**, 7342–7372 (2017).
3. Kamyshny, A. & Magdassi, S. Conductive nanomaterials for printed electronics. *Small* **10**, 3515–3535 (2014).
4. Hui, Z. *et al.* Chemical sintering of direct-written silver nanowire flexible electrodes under room temperature. *Nanotechnology* **28**, (2017).
5. Li, J. *et al.* A flexible plasma-treated silver-nanowire electrode for organic light-emitting devices. *Sci. Rep.* **7**, 1–9 (2017).
6. Perelaer, J. *et al.* Roll-to-roll compatible sintering of inkjet printed features by photonic and microwave exposure: From non-conductive ink to 40% bulk silver conductivity in less than 15 seconds. *Adv. Mater.* **24**, 2620–2625 (2012).
7. Spechler, J. A., Nagamatsu, K. A., Sturm, J. C. & Arnold, C. B. Improved efficiency of hybrid organic photovoltaics by pulsed laser sintering of silver nanowire network transparent electrode. *ACS Appl. Mater. Interfaces* **7**, 10556–10562 (2015).
8. Allen, M. L. *et al.* Electrical sintering of nanoparticle structures. *Nanotechnology* **19**, (2008).
9. Reiser, B., González-García, L., Kanelidis, I., Maurer, J. H. M. & Kraus, T. Gold nanorods with conjugated polymer ligands: Sintering-free conductive inks for printed electronics. *Chem. Sci.* **7**, 4190–4196 (2016).
10. Wang, J. *et al.* Silver nanowire electrodes: Conductivity improvement without post-treatment and application in capacitive pressure sensors. *Nano-Micro Lett.* **7**, 51–58 (2014).
11. Grouchko, M., Kamyshny, A., Mihailescu, C. F., Anghel, D. F. & Magdassi, S. Conductive inks with a 'built-in' mechanism that enables sintering at room temperature. *ACS Nano* **5**, 3354–3359 (2011).
12. Olichwer, N., Leib, E. W., Halfar, A. H., Petrov, A. & Vossmeyer, T. Cross-linked gold nanoparticles on polyethylene: Resistive responses to tensile strain and vapors. *ACS Appl. Mater. Interfaces* **4**, 6151–6161 (2012).
13. Kanelidis, I. & Kraus, T. The role of ligands in coinage-metal nanoparticles for electronics. *Beilstein J. Nanotechnol.* **8**, 2625–2639 (2017).
14. Zhang, X. *et al.* Conformation-Dependent Coordination of Carboxylic Acids with Fe 3 O 4 Nanoparticles Studied by ATR-FTIR Spectral Deconvolution. *Langmuir* **35**, 5770–5778 (2019).
15. Salvatore, G. A. *et al.* Wafer-scale design of lightweight and transparent electronics that wraps around hairs. *Nat. Commun.* **5**, 2982 (2014).

16. Kluenker, M., Mondeshki, M., Nawaz Tahir, M. & Tremel, W. Monitoring Thiol-Ligand Exchange on Au Nanoparticle Surfaces. *Langmuir* **34**, 1700–1710 (2018).
17. Dinkel, R., Braunschweig, B. & Peukert, W. Fast and slow ligand exchange at the surface of colloidal gold nanoparticles. *J. Phys. Chem. C* **120**, 1673–1682 (2016).
18. Zhou, S. *et al.* Enabling Complete Ligand Exchange on the Surface of Gold Nanocrystals through the Deposition and Then Etching of Silver. *J. Am. Chem. Soc.* **140**, 11898–11901 (2018).
19. Kister, T., Maurer, J. H. M., González-García, L. & Kraus, T. Ligand-Dependent Nanoparticle Assembly and Its Impact on the Printing of Transparent Electrodes. *ACS Appl. Mater. Interfaces* **10**, 6079–6083 (2018).
20. Sun, Y., Mayers, B., Herricks, T. & Xia, Y. Polyol synthesis of uniform silver nanowires: A plausible growth mechanism and the supporting evidence. *Nano Lett.* **3**, 955–960 (2003).
21. Ge, Z. & Wang, Y. Estimation of Nanodiamond Surface Charge Density from Zeta Potential and Molecular Dynamics Simulations. *J. Phys. Chem. B* **121**, 3394–3402 (2017).
22. Lee, S. H. & Jun, B. H. Silver nanoparticles: Synthesis and application for nanomedicine. *Int. J. Mol. Sci.* **20**, (2019).
23. Mdluli, P. S. *et al.* Selective adsorption of PVP on the surface of silver nanoparticles: A molecular dynamics study. *J. Mol. Struct.* **1004**, 131–137 (2011).
24. Uznanski, P., Zakrzewska, J., Favier, F., Kazmierski, S. & Bryszewska, E. Synthesis and characterization of silver nanoparticles from (bis)alkylamine silver carboxylate precursors. *J. Nanoparticle Res.* **19**, (2017).
25. Liu, P., Qin, R., Fu, G. & Zheng, N. Surface Coordination Chemistry of Metal Nanomaterials. *J. Am. Chem. Soc.* **139**, 2122–2131 (2017).
26. Gao, Y. *et al.* Evidence for the monolayer assembly of poly(vinylpyrrolidone) on the surfaces of silver nanowires. *J. Phys. Chem. B* **108**, 12877–12881 (2004).
27. Ge, Z. & Wang, Y. Estimation of Nanodiamond Surface Charge Density from Zeta Potential and Molecular Dynamics Simulations. *J. Phys. Chem. B* **121**, 3394–3402 (2017).
28. Lowry, G. V. *et al.* Guidance to improve the scientific value of zeta-potential measurements in nanoEHS. *Environ. Sci. Nano* **3**, 953–965 (2016).
29. McCreery, R. L. Molecular electronic junctions. *Chem. Mater.* **16**, 4477–4496 (2004).
30. Zabet-Khosousi, A. & Dhirani, A. A. Charge transport in nanoparticle assemblies. *Chem. Rev.* **108**, 4072–4124 (2008).
31. Stadler, R. & Jacobsen, K. W. Fermi level alignment in molecular nanojunctions and its relation to charge transfer. *Phys. Rev. B* **74**, 161405 (2006).
32. James J. P. Stewart. MOPAC: A semiempirical molecular orbital program. *J. Comput. Aided. Mol. Des.* **4**, 1–103 (1990).
33. Melo, M. C. R. *et al.* NAMD goes quantum: An integrative suite for hybrid simulations.

*Nat. Methods* **15**, 351–354 (2018).

34. Bergin, S. M. *et al.* The effect of nanowire length and diameter on the properties of transparent, conducting nanowire films. *Nanoscale* **4**, 1996–2004 (2012).
35. Selzer, F. *et al.* Electrical limit of silver nanowire electrodes: Direct measurement of the nanowire junction resistance. *Appl. Phys. Lett.* **108**, (2016).

# Chapter 5 - Solvodynamic Printed Silver Nanowire-Ethylene-co-Vinyl Acetate Composite Films as Highly Sensitive Piezoresistive Pressure Sensors

## 5.1 Introduction

In recent years, there has been an increasing amount of research in the area of smart materials, which includes materials for high performance sensors and actuators.[1] In particular, pressure sensing is one important area due to its diverse range of applications from low pressure acoustic sensors, touch screens, medical sensors, to high pressure impact sensing.[2–5] More recently, the development of flexible and wearable electronics has created a need for a new generation of flexible sensors in applications such as health monitoring and e-skin for robotics.[6,7] These applications involve the detection of much lower pressures, which require pressure sensors with much higher sensitivities than what is commercially available. Flexible pressure sensors also have advantages over traditional pressure sensors as they are less bulky and their flexibility allows them to be applied on irregular surfaces. Furthermore, flexible sensors are cheaper to fabricate due to their compatibility with solution processing and roll-to-roll processes.

As reviewed in Chapter 2, piezoresistive sensors have the advantages of high sensitivity, ease of fabrication and simple device setup.[8] A common type of piezoresistive flexible pressure sensor uses elastic composites with conductive fillers. Any pressure applied on the film alters the contact or bulk resistance within the material, leading to change in resistance of the entire structure.[9] Microstructure patterning on the films are often done to achieve higher sensitivities.

In terms of the elastic matrix material, polydimethylsiloxane (PDMS) and polyurethane (PU) are among the two most commonly used materials due to their high elasticity and large elongation.[10,11] However, the main drawback of these materials is their low surface energies which hinders their processability and application in devices.[12] An alternative elastic matrix material that could be used is ethylene-vinyl acetate (EVA). EVA is a copolymer between ethylene and vinyl acetate (VA) monomers. It is an interesting material as its properties vary greatly with VA content. At low VA content, EVA behaves like low density polyethylene with increased flexibility and softness due to the presence of the VA monomers. As the VA content increases to above 30%, it begins to behave like an elastomer. In terms of processing, EVA can be melt or solution processed. Due to the presence of both hydrophobic ethylene and hydrophilic VA groups, it is compatible with a wide range of polymers to create multilayer structured devices. These properties make EVA suitable for use as the elastic matrix for a piezoresistive composite film.[13,14]

Among the different types of conductive fillers[15–19], the use of AgNWs is a promising option as they have outstanding electrical properties, allowing them to form highly conductive networks. As a result, the pressure sensing composite film can achieve very high conductivities which in turn reduces the power consumption of the pressure sensing device.[20] In addition, AgNWs are mechanically robust and highly suited for application in flexible and stretchable devices.[21] Despite these advantages, AgNWs have found limited application in pressure sensors but are more widely used as strain sensors.

In this chapter, a fully solution-processed piezoresistive pressure sensor based on a composite film with AgNWs embedded in an EVA matrix is presented. Unlike most of the reported piezoresistive flexible pressure sensors that utilize compressive strains, it is

hypothesized that by making use of pressure-induced tensile strains, higher sensitivities can be achieved. This concept will be explored in this chapter using the composite films. Furthermore, the performance of the film can be tuned by the composition of AgNWs and EVA which determines the electrical and mechanical properties of the film respectively. The films will be fabricated using solvodynamic printing.[22] The ability to be fully solution processed is an added advantage as it means that these films can be produced cheaply at high throughput. Solvodynamic printing, as an additive printing technique is suitable to fabricate these composite films as it is effective in producing both unpatterned and patterned films as shown in the previous chapters.

### 5.1.1 Pressure Sensor Schematics

Fundamentally, the composite film should function as a pressure sensor based on the percolation network of the AgNWs within the EVA matrix. Any applied pressure on the film can alter the arrangement and relative density of the AgNWs and therefore changes the resistivity of the film. By varying the pressure sensor setup, externally applied pressure can be converted into either compressive or tensile strains as shown by the schematics in Figure 5-1. The first mode as shown in Figure 5-1a is the compressive mode, whereby the film is placed on a supporting surface. When a pressure is applied onto the film, the film becomes compressed and the nanowires in the film should be pushed closer towards each other, resulting in a decrease in film resistance. The second possible mode as shown in Figure 5-1b is the tensile mode, whereby the film is suspended at 2 corners or edges of the film without any supporting surfaces directly below the film much like the configuration of a traditional silicon piezoresistive pressure sensor.[23] When a pressure is applied, the film stretches downwards and elongates. In this mode, the nanowires in the film should be pulled further apart, causing an increase in film resistance.

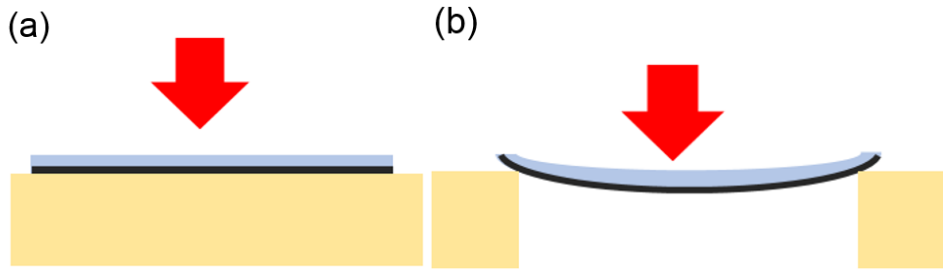



Figure 5-1: Schematics of: (a) compressive pressure sensing mode, (b) tensile pressure sensing mode.

## 5.2 Materials and Methods

### 5.2.1 Materials

Silver nitrate, ethylene glycol, copper (II) chloride, polyvinylpyrrolidone with average molecular weight of 55000 and poly(ethylene-co-vinyl acetate) with 40 wt% vinyl acetate were purchased from Sigma Aldrich.

Silver nanowires used in this study were synthesized via the polyol process[24]. In a typical synthesis, 0.1811 g of silver nitrate was dissolved in 1.5 ml of ethylene glycol. In a separate glass vial, 0.8 g of PVP was dissolved in 20 ml of ethylene glycol and heated to 150 °C with magnetic stirring. 20 µL of a 0.15 M aqueous copper (II) chloride solution was then added to the PVP solution. Once the solution was mixed homogenously, the silver nitrate solution was added and the reaction mixture was left for 1 hour. After the reaction, the nanowires were washed with methanol and subsequently centrifuged at 2500 rpm for 10 min. The washing cycle was repeated 3 times before redispersing the nanowires in methanol to make up a suspension with AgNW concentration of 1 mg/ml for ligand exchange.

During the ligand exchange, approximately 5.38 mg of fumaric acid was added for every milliliter of AgNW solution, which makes a molar ratio of 5:1 between fumaric acid and silver. The mixture was magnetically stirred and left overnight for 24 hours. The

suspensions were then centrifuged at 2500 rpm for 10 mins. The supernatant was discarded and the AgNWs were redispersed into a water-ethylene glycol mixture with 15 wt% ethylene glycol to produce the final AgNW printing ink. The concentration of AgNW in the ink was fixed at 6 mg/ml. An EVA solution was also preprared by dissolving it in toluene to make up a solution with concentration of 14 wt%.

### 5.2.2 Fabrication of Composite Film

A 2.6 cm by 2.6 cm piece of glass substrate was cut and cleaned. The cleaning was done by ultrasonicating the substrate in decon soap solution, DI water, acetone and isopropanol sequentially at 40 °C for 5 min each. The AgNW ink was solvodynamically printed onto the glass substrate using hexane as carrier solvent. Two types of films were printed, unpatterned and patterned films.

The unpatterned films were printed in a similar way as in Chapter 4, with the print covering the entire glass substrate. The nominal ink and carrier solvent flow rates were fixed at 10 μl/min and 20 μl/min respectively. The substrate velocity was set at 5 mm/s. Each layer of printing deposited approximately 0.025 mg/cm$^2$ of AgNWs. Films with varying overall AgNW loading ranging between 0.1 to 0.25 mg/cm$^2$ were printed by printing 4 to 10 layers of AgNWs. A drying step was performed at 90 °C for 5 mins between each layer and a final drying step was done after the last layer for 10 mins at 90 °C.

The patterned films were printed following the grid design as shown in Figure 5-2. The grid has 4 by 4 grid lines with varying grid width denoted by $t_{grid}$. To print the grid, one set of four grid lines were first printed. The substrate was then rotated 90° and the other 4 grid lines were printed to complete the grid. Three grids with $t_{grid}$ of 1.6 mm, 2.0 mm and 3.0

mm were printed. The nominal ink and carrier solvent flow rates were lowered to 200 µl/hr and 400 µl/hr respectively. The substrate velocity was increased to 20 mm/s. These settings were done to improve the printing resolution for the patterning.

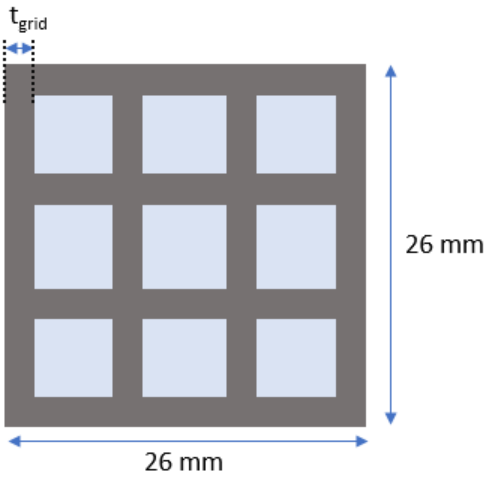



Figure 5-2: Design of the patterned films. $t_{grid}$ represents the grid line width. Grids with $t_{grid}$ of 0.16 mm, 0.2 mm and 0.3 mm were printed.

After printing the AgNW films, the EVA solution was drop casted on top of the AgNW film and left to dry. Once the EVA had completely dried, the film was peeled off the glass substrate using a pair of tweezers. Films with different EVA thicknesses were made and the corresponding volume of EVA solution required for each type of film is listed in Table 5-1. Generally, the EVA solution could not be deposited all at once as it would overflow. The deposition was done 1 ml at a time with approximately 20 mins drying time in between each deposition.

Table 5-1: Volume of EVA solution required for making films with different EVA thicknesses

| EVA film thickness (mm) | Volume of EVA solution drop casted (ml) |
|---|---|
| 0.30 | 2.0 |
| 0.35 | 2.5 |
| 0.40 | 3.0 |

### 5.2.3 Characterization of Film Properties

The dimensions of AgNWs, surface morphology and cross section of the AgNW-EVA composite films were characterized using scanning electron microscopy (JEOL JSM-840F SEM) at 5 kV accelerating voltage and approximately 9 mm working distance. The thicknesses of the AgNW films on glass substrates were characterized by surface profilometry (Veeco DekTak 6M stylus profiler) which uses a 12.5 μm radius diamond tip stylus. The measurement settings were 3 mg stylus force, scan length 2 mm with a resolution of 0.167 μm. The sheet resistances of all films were characterized by a 4-point probe (Jandel cylindrical probe) with applied currents in the range between 0.1 to 5 μA. 10 measurements were taken at random locations on each film to obtain a representative average sheet resistance.

### 5.2.4 Electromechanical Measurements of Pressure Sensor

All electromechanical measurements were done using a LCR meter (Agilent E4890A). A LabVIEW programme was made to control and record the values detected by the LCR meter. The setup used in the compressive and tensile mode were slightly different as shown in Figure 5-3. In the compressive mode, the film was placed onto a petri dish. Two strips of copper tapes were adhered to the corners of the AgNW-EVA film on the conductive side. The copper tapes were then connected to the LCR meter using crocodile clips. The length of contact between the copper tape and the composite film was fixed at 0.3 mm for each side. Two pieces of regular tape were then used to secure the AgNW-EVA film and copper tape against the petri dish to keep the film fixed. During characterization, the LabVIEW programme was initiated and the resistance of the film were recorded until the programme was manually turned off. Objects were placed manually onto the film while the programme was running. The first object placed on the film was always a 2.0 cm by 2.6 cm glass slide.

The purpose of the glass slide was to control the area which the weight of the subsequent objects acted on the film and to ensure the pressure experienced by the AgNW-EVA film was uniform throughout the area of the glass slide. The glass slide must be carefully positioned such that it does not lie directly above the copper tape-composite film interface to minimize any change in contact resistance between the copper tape and the AgNW-EVA film during the measurement, and therefore ensuring that the change in resistance measured only arises from the AgNW-EVA film itself. Subsequently, one-pound coins were stacked onto the glass slide manually to apply different pressures on the film. The coins could be stacked and removed one by one or be taped into a stack to be placed and remove together to create larger changes in pressure. Up to seven one-pound coins were used. The mass of the glass slide and coins were measured by a weighing balance and was found to be 0.766 ± 0.002g and 8.793 ± 0.04 g respectively. These values together with the area of the glass slide were used to evaluate the pressure applied onto the film. The resultant pressure exerted on the films inclusive of the glass slide are tabulated in Table 5-2.

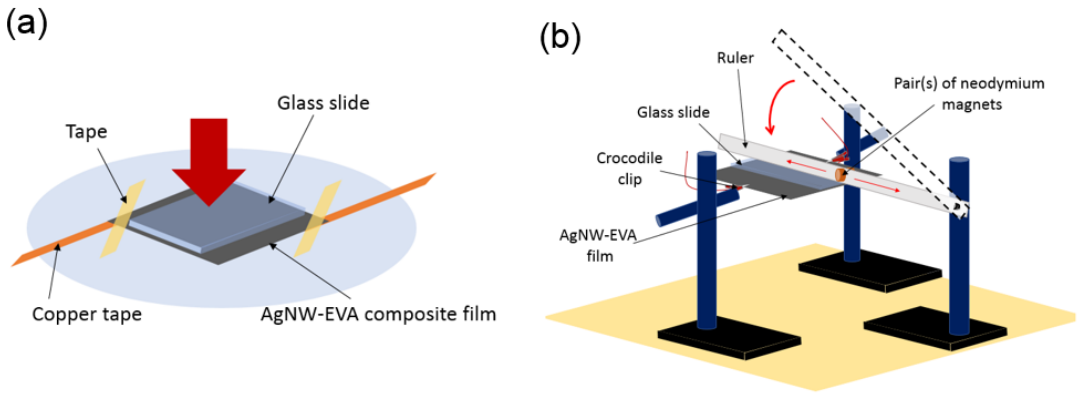



Figure 5-3: Schematics of pressure sensor setup for (a) compressive mode and (b) tensile mode.

Table 5-2: Pressure applied on AgNW composite film by stacking one-pound coins on a glass slide for compressive mode pressure sensing

| No. of one-pound coins | Pressure (Pa) |
|---|---|
| 0 | 1.47 |
| 1 | 18.4 |
| 2 | 35.3 |
| 3 | 52.2 |
| 4 | 69.1 |
| 5 | 86.0 |
| 6 | 103 |
| 7 | 120 |

In the tensile mode, the film was clamped directly at opposite edges using crocodile clips which were held up using retort stands. The clamps on both sides were adjusted to be at the same height to ensure that the film was horizontal. The separation between the clamps were also adjusted to ensure that there was no initial strain on the film. A modified loading system, as shown in Figure 5-3b, was used for the tensile mode compared to the compressive mode as the size of the one-pound coins were too large and tended to get caught on the crocodile clips, therefore affecting the actual force exerted on the films. In this setup, the size of the glass slide was reduced to 1.2 cm by 2.6 cm to keep clear of the crocodile clips. Forces were applied on the film using a lever system. A hole was drilled near one end of a plastic ruler and the ruler was fixed to a vertical metallic fixture using a screw through the hole. This point acted as the fulcrum for the ruler to rotate freely around. The structure was positioned some distance away from the film such that the free end of the ruler can rest horizontally on the film's surface and apply a downward force and pressure. The contact point between the ruler and the film was approximately 17.5 cm away from the fulcrum. Pairs of small round neodymium magnets were attached on the sides of the ruler to act as weights. The force exerted on the film can then be controlled by varying the number of

magnets on the ruler, as well as their positions relative to the fulcrum of the ruler. The mass of a neodymium magnet and the plastic ruler were 10.43 mg and 7.749 mg respectively. The range of pressures applied using this method is tabulated in Table 5-3.

Table 5-3: Pressure applied on AgNW composite film by attaching different number of neodynium magnets on plastic ruler at various distance from the fulcrum for tensile mode pressure sensing

| No. of magnets | Distance of magnet from fulcrum (cm) | Moments generated (mNm) | Force exerted on glass (mN) | Pressure on film (Pa) |
|---|---|---|---|---|
| 2 | 0 | 0.736 | 4.21 | 12.9 |
| 2 | 5.5 | 1.88 | 10.8 | 33.1 |
| 2 | 9.5 | 2.72 | 15.5 | 47.8 |
| 2 | 13.5 | 3.55 | 20.3 | 62.5 |
| 2 | 17.5 | 4.39 | 25.1 | 77.1 |
| 4 | 10.5 | 5.12 | 29.2 | 90.0 |
| 4 | 12.5 | 5.95 | 34.0 | 105 |
| 4 | 14.5 | 6.79 | 38.8 | 119 |
| 4 | 16.5 | 7.62 | 43.5 | 134 |
| 6 | 12.5 | 8.56 | 48.9 | 150 |
| 6 | 14.5 | 9.81 | 56.1 | 172 |
| 6 | 16.5 | 11.1 | 63.2 | 194 |
| 6 | 18.5 | 12.3 | 70.4 | 217 |
| 8 | 17.5 | 15.3 | 83.4 | 257 |

Additional tensile strain measurements were also done on the films to study the resistance response to tensile strain. The film was clamped at two opposite ends. One of the clamps were attached to a retort stand while the other end was left hanging vertically. Crocodile clips were clipped onto the two opposite ends of the film and connected to the LCR meter to monitor its resistance. During measurement, hook weights ranging from 50 g to 450 g were hung onto the clamp on the free end which causes the film to stretch. The length of the film was then measured using vernier calipers.

Pulse measurements were also performed to test the application of the pressure sensor. For these measurements, a AgNW-EVA composite films was placed against the subject's neck. A small piece of cling film was placed between the subject's skin and the AgNW-EVA film to avoid direct contact of the film. Two strips of copper tapes were taped onto two opposite corners of the AgNW-EVA composite film. Two pieces of tapes were then taped onto the corners with the copper tapes to secure the AgNW-EVA film against the subject's neck. The film should not be overstretched or too slack to ensure accurate measurement. After the film was secured, crocodile clips were attached to the ends of the two copper strips and electrically connected to the LCR meter. During the measurement, the LabVIEW programme was started and the resistance of the film was monitored for approximately one minute. This was repeated at least 3 times for each type of film used to check for repeatability.

During all electromechanical measurements, the "R-X" measurement mode, which monitors both the resistance and reactance of the sample, was selected on the LCR meter. The frequency of the input voltage was typically set at 500 Hz and measurement time setting was set as medium, resulting in a time resolution of ~100 ms. For response time measurements, a higher frequency of 100000 Hz and measurement time was set as short to achieve a higher time resolution of ~5 ms per measurement. It was verified that the change in frequency did not affect the measured resistance values so that measurements done at different AC frequencies were consistent with each other. At least five measurements were made on each film and the average resistance response at each applied pressure was obtained.

## 5.3 Results and Discussion

### 5.3.1 General AgNW-EVA Film Properties

Figure 5-4a shows an image of the silver nanowires used in this study. They had average lengths of approximately 20 μm and diameters of 80 nm. It was noted that the high aspect ratio of the nanowires was important in the film forming process as a similar procedure using AgNPs could not form composite films in the same way. The gaps created in between the AgNW network allows for the EVA to fill up and surround the AgNWs, anchoring the AgNWs strongly in the EVA matrix. When the film was peeled off, the AgNWs remained in the EVA matrix. When AgNPs were used instead, they were not embedded in the matrix as strongly. As a result, when the film was peeled, all of the AgNPs remained on the glass substrate and a composite film did not form.

Figure 5-4b shows a photograph of an AgNW-EVA composite film. The film was quite thin, approximately 350 μm thick and very flexible. The thinness and flexibility of the film allow it to be easily applied onto different surface and devices. As the AgNWs and EVA were deposited sequentially, the composite film formed two distinct layers. The layer in contact with the glass is the conductive layer as it had a high concentration of AgNWs. Consequently, the region above had little to no AgNWs and is non-conductive. The surface of the conductive side was very smooth as it was formed against the glass substrate. Figure 5-4c shows an SEM image of surface of the conductive side. The embedding was observed clearly as AgNWs can be seen at different depths from the surface and aligned in random directions. Figure 5-4d shows the cross-section of the entire composite film and the inset is a high magnification image of the conductive layer. The thickness of the conductive layer was found to be approximately 10 to 15 μm thick depending on the nanowire loading during the deposition step.

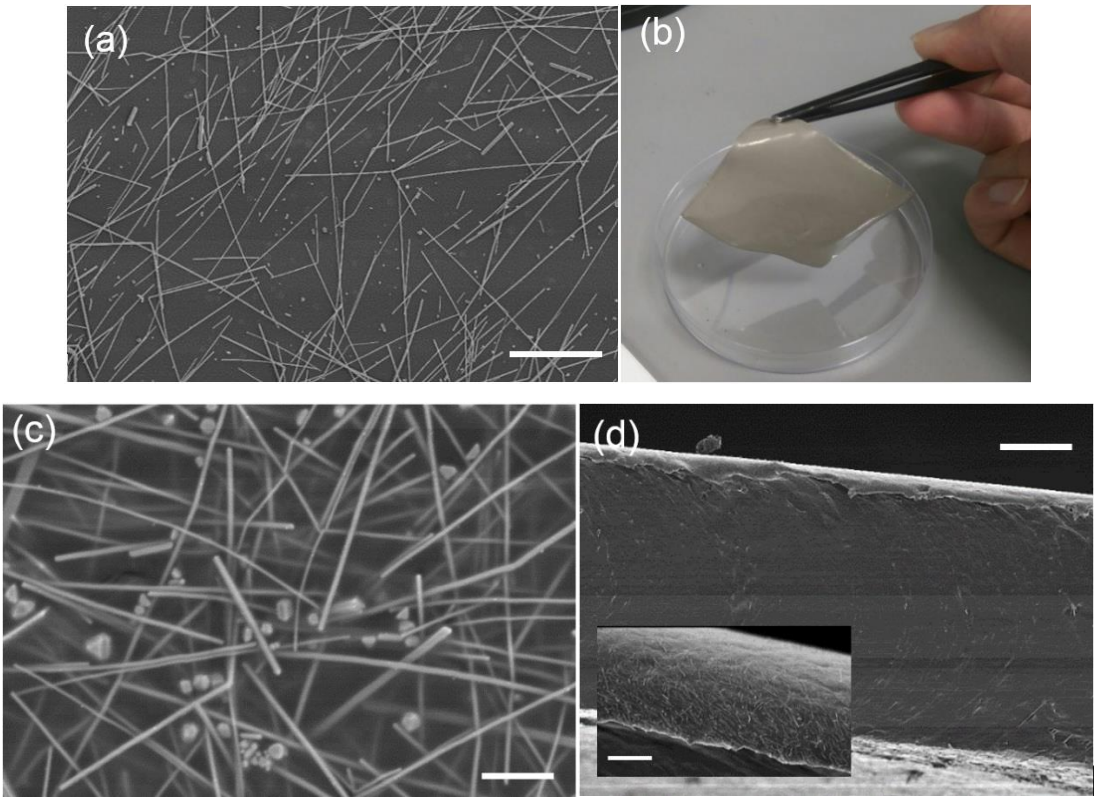



Figure 5-4: (a) SEM image of silver nanowires (AgNWs) used in this study. The scale bar represents 10 μm. (b) Photograph of an AgNW-EVA composite film. (c) SEM image of the surface morphology of the conductive side of the film. The scale bar represents 1 μm. (d) SEM image of the cross section of the composite film. The scale bar represents 100 μm. The inset is a high magnification image of the conductive layer. The scale bar represents 5 μm.

### 5.3.2 Electrical Properties of Composite Films

Since the pressure sensing properties are based on the variation in resistance, it would be useful for us to understand the film's electrical properties. Different films were fabricated by varying the concentration of AgNWs used in the initial deposition step. Their sheet resistances and conductivities were then characterized. Figure 5-5a shows the variation in sheet resistance of the films with nanowire concentration. As expected in a percolative conductor, the sheet resistance of the composite film decreased with an increase in nanowire concentration as more conductive pathways are created for the conduction. It was also observed that the sheet resistance of the AgNW network increased drastically, by up to 20 times after the addition of EVA. This was attributed to the EVA moving in between the

AgNWs when it was deposited. The thickness of the pure AgNW film before the deposition of EVA was only between 0.65 and 1.4 μm and increased to 10 to 20 μm after the EVA was added. This is shown in Figure 5-5b. The presence of the EVA disrupted the percolation of the existing AgNWs and reduced the conductivity of the network.

As the conductive layer is quite thick, this portion of the film should behave as a three-dimension percolation solid. According to percolation theory, the conductivity of a 3D percolation network can be described empirically by the power law:[25]

$$\sigma = \sigma_0(\phi - \phi_0)^t \tag{5-1}$$

where $\sigma$ is the conductivity of the network, $\sigma_o$ is a system dependent pre-exponential factor that depends on the resistivity of the fillers and their contact resistance,[26] $\phi$ is the conductive filler volume fraction, $\phi_o$ is the percolation threshold and *t* is the critical exponent. From the review in Chapter 2, the critical exponent for the case of 3D AgNW percolating structures should be fixed at a value of $t$ = 2 for any value of $\phi$ as long as the system is junction resistance dominated, although some degree of deviation would also be possible due to tunneling currents in the film.[27,28] The value of the percolation threshold, $\phi_o$, was estimated based on the work by Garboczi et. al. They showed that the percolation threshold varies with the aspect ratio of the filler as follows:[29]

$$\phi_0 = 0.6\frac{D}{L} \tag{5-2}$$

where *D* and *L* are the filler diameter and length respectively. Given, the dimensions of the nanowires used in the films, $\phi_o$ was approximated to be 0.16 %.

Using equations 5-1 and 5-2, the theoretical conductivities were calculated and fitted with the experimental results as shown in Figure 5-5c. Overall, the sample conductivities follow the power law with $t$ = 2.475. The slight deviation from the universal value of t = 2 suggests that there may be some degree of tunneling involved in the conductive network.[30,31] The empirical relation here will be used in the subsequent sections when the pressure response of the films are studied.

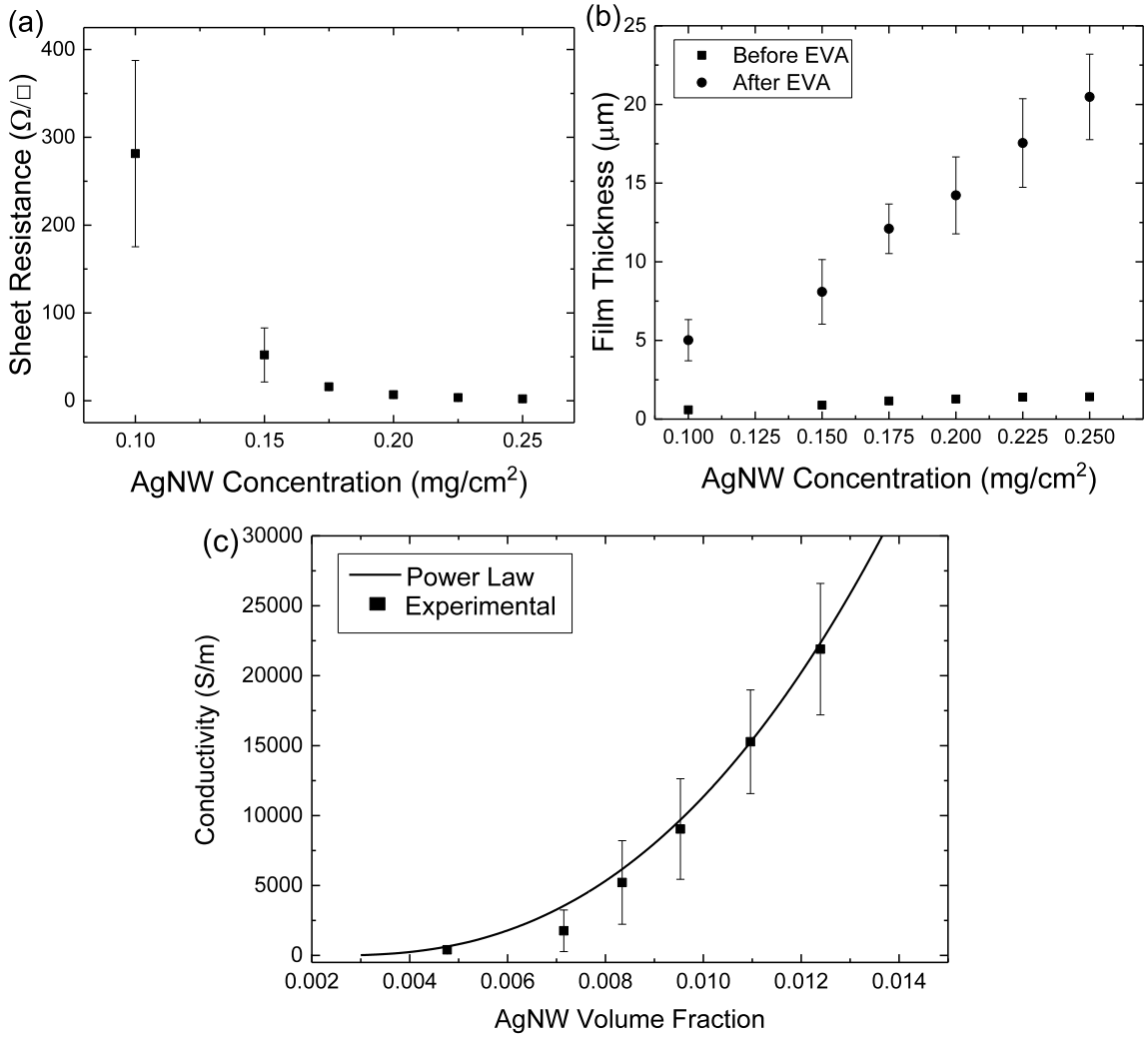



Figure 5-5: (a) Sheet resistance, (b) thickness of the conductive layer and (c) conductivity of the AgNW-EVA composite films with different AgNW loading.

### 5.3.3 Electromechanical Response to Pressure

As mentioned previously, the pressure sensing of the films can occur in the compressive and tensile mode. In this section, the pressure sensing properties of the films will be demonstrated. The effect of the AgNW and EVA loading on the film sensing performance will also be explored with focus on maximizing sensitivity. In addition, the detection limit and response time will also be characterized.

#### 5.3.3.1 Compression Mode Pressure Sensor

The compression mode pressure sensor was fabricated using a 2.6 cm by 2.6 cm film. Different weights were placed on the film while the film's resistance was recorded. Figure 5-6a shows the electrical response of the film when 2 one-pound coins, equivalent to 35.3 Pa was placed and removed repeatedly on the film. As expected, the resistance of the film decreased when the weight is placed on the film. The film also showed good consistency as the resistance values with and without the weight was repeatable. The measurements were then repeated for different weights placed onto the film and for different films made with different AgNW concentrations. The results are tabulated in Figure 5-6b. All of the samples, aside from the one with 0.15 mg/cm$^2$ AgNW, managed to generate an observable electrical response from an applied pressure of 1.47 Pa, showing that the films had a very low detection limit.

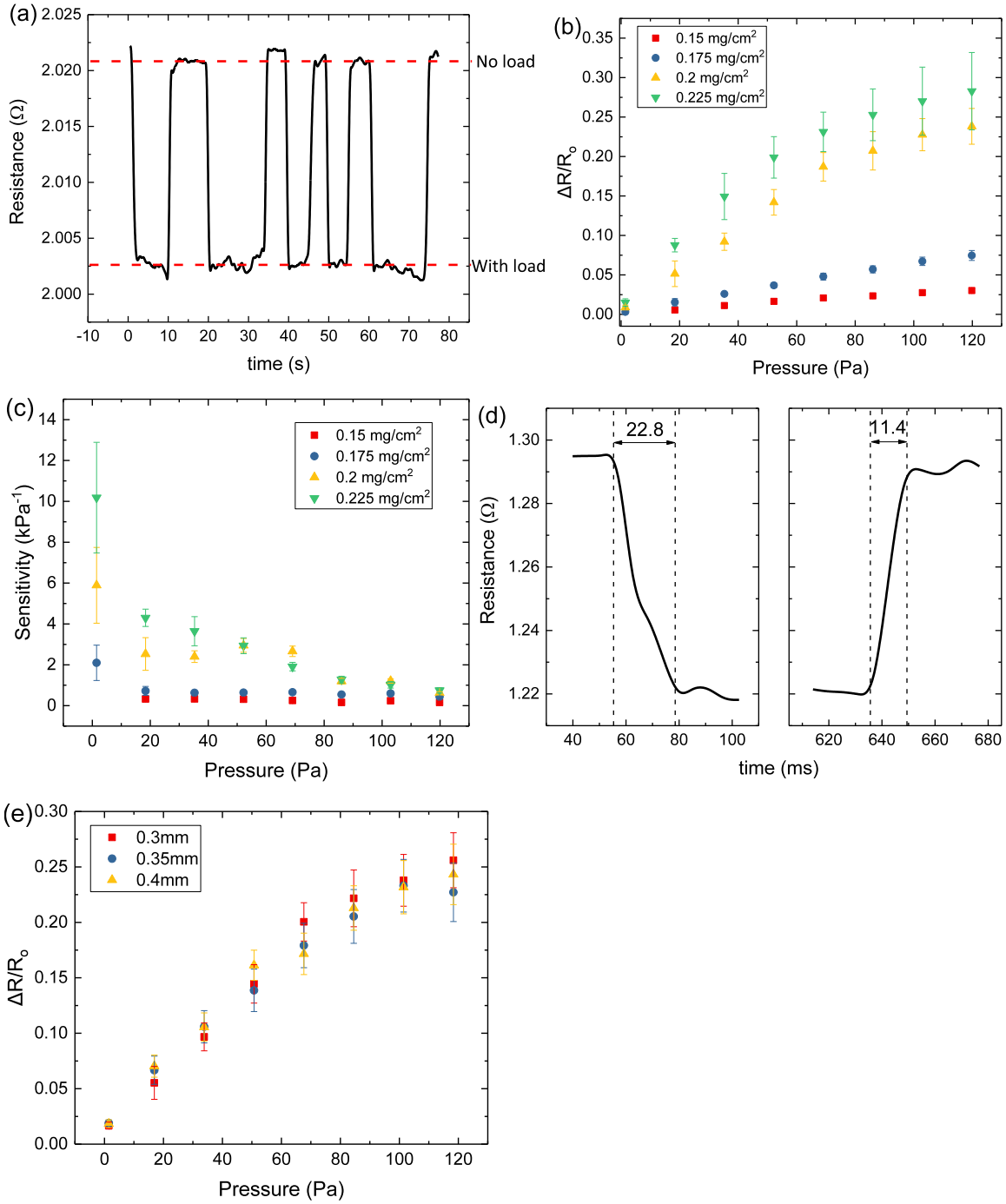



Figure 5-6: (a) The electrical response of an AgNW-EVA film fabricated with AgNW concentration of 0.15 mg/cm$^2$ when a pressure of 33.8 Pa was applied repeatedly. (b) The variation of change in resistance of the films with applied pressure for several films made with different AgNW concentrations. (c) The variation of pressure sensing sensitivities of films with different AgNW loading at different applied pressures. (d) The response time of the composite film during loading (left) and unloading (right). (e) Electromechanical response of AgNW-EVA composite films with varying EVA thicknesses.

From the plot, the sensitivity of the pressure sensor can be evaluated. The sensitivity of pressure sensor is defined as follows:[17]

$$S = \frac{\Delta R/R_0}{\delta P} \tag{5-3}$$

where $R_o$ is the original resistance of the film without any applied pressure and $\Delta R$ is the change in film resistance when the pressure applied changes by a small amount $\delta P$. Therefore, the sensitivity can be estimated by the slope of the curves in Figure 5-6b. The resultant sensitivities for each sample at different loadings are shown in Figure 5-6c. For all samples, the sensitivity typically decreases with increase in applied pressure. This can be explained by understanding the pressure sensing mechanism. As previously mentioned, an applied pressure pushes the nanowires in the film closer together and new conductive pathways are formed, leading to the decrease in resistance. As more pressure is applied, the potential number of additional connections possible diminishes and therefore the resistance changes at a decreasing rate. Eventually, there comes to a point whereby the possible connections among the nanowires are maximized and no further decrease in resistance will occur. This high initial sensitivity is probably the reason for the low detection limit displayed by the films.

When comparing between films with different nanowire concentration, it was observed that the maximum sensitivity increased with nanowire concentration from 0.328 $kPa^{-1}$ in the 0.15 $mg/cm^2$ film to a maximum of 10.2 $kPa^{-1}$ in the 0.225 $mg/cm^2$ film. This is an interesting observation. Based on percolation theory, a film with higher nanowire concentration should experience less change in resistivity given the same change in the filler concentration due to the mathematical nature of the power law. Therefore, the observation suggests that the compression mode sensor does not work purely based on percolation. A more likely mechanism involved is the decrease in the contact resistance between

neighbouring nanowires, $R_c$ which can be mathematically described by equation 5-4 below.[19]

$$R_c = \frac{\rho^2 \eta \pi H}{4F} \tag{5-4}$$

where $\rho$ is the electrical resistivity, $\eta$ is an empirical coefficient, $H$ is the hardness of the material and $F$ is the applied load. Therefore, the applied load can reduce the contact resistance of the nanowire network. In a film with a denser network of nanowires, more nanowire junctions existing per unit area and the decrease in contact resistance produces a larger effect in the overall resistance of the film. Another possible explanation is that pushing the nanowires closer to each other can also activate more electron tunneling pathways between neighouring nanowires and contribute to the increase in conductivity. Mathematically, this would be represented by an increase in $t$ in the power law with increasing nanowire density.

The response time of the films were also characterized by increasing the frequency of the input voltage, attaining a maximum time resolution of 5.7 ms. Figure 5-6d shows a typical pressure response of the film. It can be seen that the compression motion took about 22 ms to complete while the relaxation step was quicker at 11 ms. This was consistently observed in subsequent waveforms as well. This makes sense as the compression step should encounter a larger resistance in motion as the nanowires have to move closer towards each other in an already dense mesh, whereas the relaxation step involves the nanowires moving away from each other into a less obstructed space. Overall, the response time of 10-25 ms is considered quite fast and can be used to detect common sources of pressure in daily life.

The EVA loading was subsequently varied during the fabrication step to create films with the same nanowire density but with different EVA thicknesses ranging from 0.3 to 0.5 mm.

The same electromechanical testing was performed on these films and their electrical responses are shown in Figure 5-6e. From the results, no significant differences in terms of sensitivities were observed when the amount of EVA changed. This observation can be explained by considering the structure of the film. As explained in the previous section, the film consists of a thick non-conductive EVA layer stacked onto a much thinner conductive composite layer. When a compressive stress is applied in the normal direction of the film, the 2 different layers should theoretically experience the same stress as described by the Ruess' iso-stress model for composite materials.[32] A change in EVA loading only alters the thickness of the non-conductive EVA layer and does not change the conductive layer. Therefore, the electromechanical response of the films should not be affected by the EVA loading in this range.

#### 5.3.3.2 Tensile Mode Pressure Sensor

The tensile mode pressure sensor was set up using the same films in the compressive mode pressure sensor but with the films suspended in air while being fixed on opposite sides. Figure 5-7a shows the typical pressure response of the film when a pressure of 62.5 Pa was applied on the film repeatedly. Once again, the expected response of an increase in resistance was observed. The measured change in resistance was stable and repeatable.

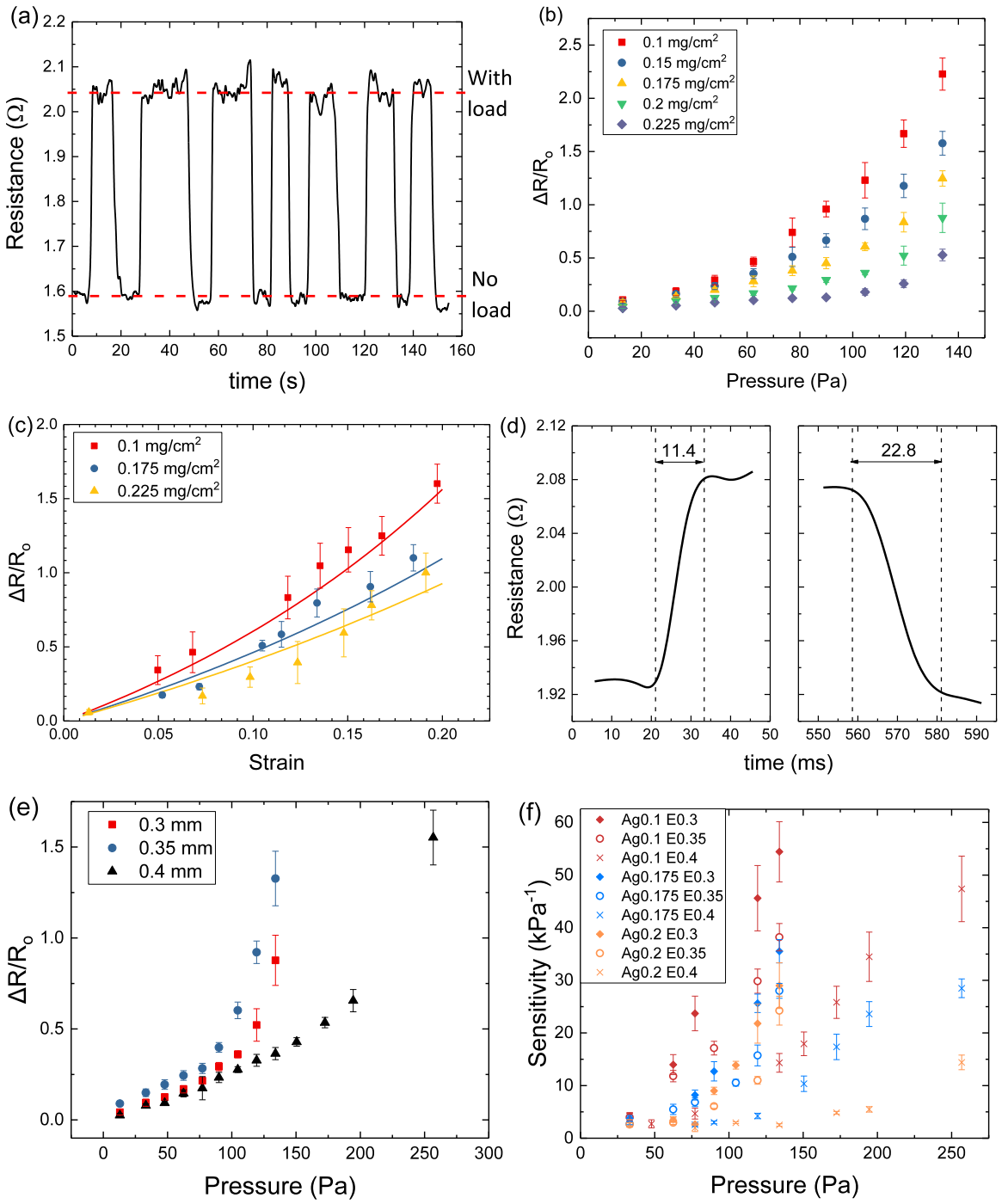



Figure 5-7: (a) The electrical response of an AgNW-EVA film fabricated with AgNW concentration of 0.2 mg/cm$^2$ when a pressure of 62.5 Pa was applied repeatedly. (b) The variation of change in resistance of the films with applied pressure for several films made with different AgNW concentrations. (c) The electrical response of the different AgNW-EVA composite films with different nanowire concentrations as strain gauges under uniaxial tensile stress. The lines represent modelled results based on the power law and the circles are the experimentally observed results. (d) The response time of the composite film during loading (left) and unloading (right). (e) The electrical response of the AgNW-EVA film with varying EVA thicknesses with AgNW concentration fixed at 0.175 mg/cm$^2$. (f) The variation in pressure sensing sensitivity when the AgNW concentration and

EVA film thickness is varied. Each sample is labelled by its AgNW loading followed by EVA thickness.

Figure 5-7b shows the pressure response of the different films under different applied pressures. The detection limit of the tensile mode sensor was found to be around 10 Pa which still lies in the low-pressure regime. In this mode, the opposite trends in sensitivity compared to the compressive mode was observed. The sensitivity of the composite films increased with increasing applied pressure. This is because when the films are stretched, the percolation network is pulled apart and the effective nanowire density decreases. As the nanowire density decreases towards the critical percolative density, the rate of change in resistance will increase drastically as the film structure gradually changes from the conductive state to the non-conductive state. Therefore, the changes in resistance will always be larger at higher applied pressure as the film is stretched more. For the same reason, the sensitivity of the film increases with the decrease in nanowire concentration in the film. Films with a lower concentration of nanowires are always closer to the critical percolation limit compared to films with higher nanowire concentration. Consequently, any applied pressure on the low concentration films will cause a larger change in resistance. From the results, the maximum sensitivity increases from 18.3 $kPa^{-1}$ in the 0.25 $mg/cm^2$ sample to 38.2 $kPa^{-1}$ in the 0.1 $mg/cm^2$ sample.

The working principle of the pressure sensor in tensile mode is strongly related to the strain experienced by the composite film. Therefore, the mechanism of the pressure sensor can be verified by studying its performance as a strain gauge. This was done by measuring the film's resistance while applying varying tensile strains on the film. Figure 5-7c shows the performance of the film as a strain gauge. The response characteristics matches with the performance of the pressure sensor. The sensitivity increased with increasing strain and

decreasing nanowire loading, achieving a maximum gauge factor of approximately 13.3. The power law in equation 5-1 was used to model the change in resistance of the film assuming that the increase in total volume of the conductive layer is proportional to the strain on the film. The modelled results are fitted with the experimental results in Figure 5-7c. A good match between the experimental and theoretical results is observed, verifying the role of strain in affecting the percolation of the AgNW and the changes in resistance.

Figure 5-7d shows a typical response time of the pressure sensor in this mode. Once again, the response times of approximately 11 and 22 ms were observed. In this case, the loading step had a response time of 11 ms while the unloading step had a slower response time of 22 ms. This is consistent with the response times observed in the compressive mode as the loading step involves nanowires moving away from each other into space in the EVA matrix while the unloading step involves the nanowires moving back towards each other.

The films with varying EVA loading were tested in the tensile mode. Figure 5-7e shows the response of samples made with nanowire concentration of 0.175 mg/cm$^2$ sample with varying EVA thicknesses. From the results, it can be seen that the thickness of the EVA affects the pressure sensor in two ways. The first observation is that sensitivity of the pressure sensor decreases with the increase in film thickness as the change in resistance observed is lower at each applied pressure. The second observation is that the dynamic sensing range of the pressure sensor increases with EVA thickness. In addition, the pressure range which produces a linear electrical response is also found to increase when the EVA thickness is increased. This makes the films more suited for measuring larger pressure ranges. Similar trends were also observed in the other samples. The overall pressure sensing sensitivities of each type of sample at different applied pressures are tabulated in Figure 5-

7f. The sensitivities of the films always decrease with increasing EVA thickness for films with the same nanowire concentration and their dynamic range is always higher as well. These observations can be explained by considering the effect of film thickness on the strain experienced by the film. According to thin plate theory, the flexural rigidity, *D* of a rectangular thin plate can be expressed as:[33]

$$D = \frac{Et^3}{12(1-v^2)} \tag{5-5}$$

where *E*, *t* and *v* are the Young's modulus, thickness and Poisson ratio of the film respectively.

Therefore, as the thickness of the AgNW composite film increases, its flexural rigidity increases and smaller strains are induced under the same stress. Since the resistance of the film is mainly related to the induced strain, a thicker film will experience a smaller change in resistance under the same stress and hence the resulting sensitivity is reduced. On the other hand, as the thicker film is more rigid, the film can stay within the functional pressure sensing resistance range under a larger range of stress, resulting in a larger dynamic range. Therefore, the properties of the pressure sensor are highly tunable based on the requirements of the pressure sensing application. Thicker films can be used for applications which may experience larger pressure ranges and thinner films will be more suited for measuring weaker pressure signals with more limited pressure range. The highest sensitivity observed was up to 54.4 $kPa^{-1}$ in the thin EVA sample with 0.1 $mg/cm^2$ nanowire concentration.

5.3.3.3 Patterned Pressure Sensors

So far, it is established that the sensitivity of the pressure sensor can be tuned by varying the AgNW and EVA composition in the unpatterned films. As previous mentioned, the sensitivity of flexible pressure sensors can often be further boosted by patterning the films.

In this section, a strategy reported by Martinez et al. is adopted in the AgNW-EVA pressure sensors.[34] In their work, they created a grid pattern by etching an AgNW film using photolithography to increase their strain sensing capabilities. They found that thinner AgNW tracks are more responsive towards tensile strain applied on the film. This was attributed to the overall reduction in number of percolation contacts within the AgNW tracks. When the tracks were stretched, a more significant decrease in the number of contacts occur, resulting in a larger change in resistance. Since the pressure sensor works based on induced strain, the same concept can be adapted to improve the tensile mode pressure sensing capabilities. However, instead of using photolithography, the patterning abilities of solvodynamic printing will be used. The resolution attainable in printing is generally inferior to photolithography but in this particular application, the resolution is not too important.

Figures 5-8a to c show the photos of three solvodynamic printed patterned AgNW-EVA composite films. Square grid patterns with 4 by 4 tracks was fabricated with track widths of approximately 1.6, 2.0 and 3.0 mm. The nanowire concentration in the printed region was fixed at 0.15 mg/cm$^2$ so that a comparison can be made with the corresponding unpatterned film. The patterned films were put under the same electromechanical testing in the previous section under the tensile mode. Figure 5-8d shows the response of the three different films under an applied pressure of 33.1 Pa. Indeed, an increase in electrical response was observed when the grid lines were thinner as reported by Martinez's study. Compared to the unpatterned film, the maximum sensitivity of the patterned film with grid line widths of 1.6 mm increased from 27.3 kPa$^{-1}$ to 67.3 kPa$^{-1}$.

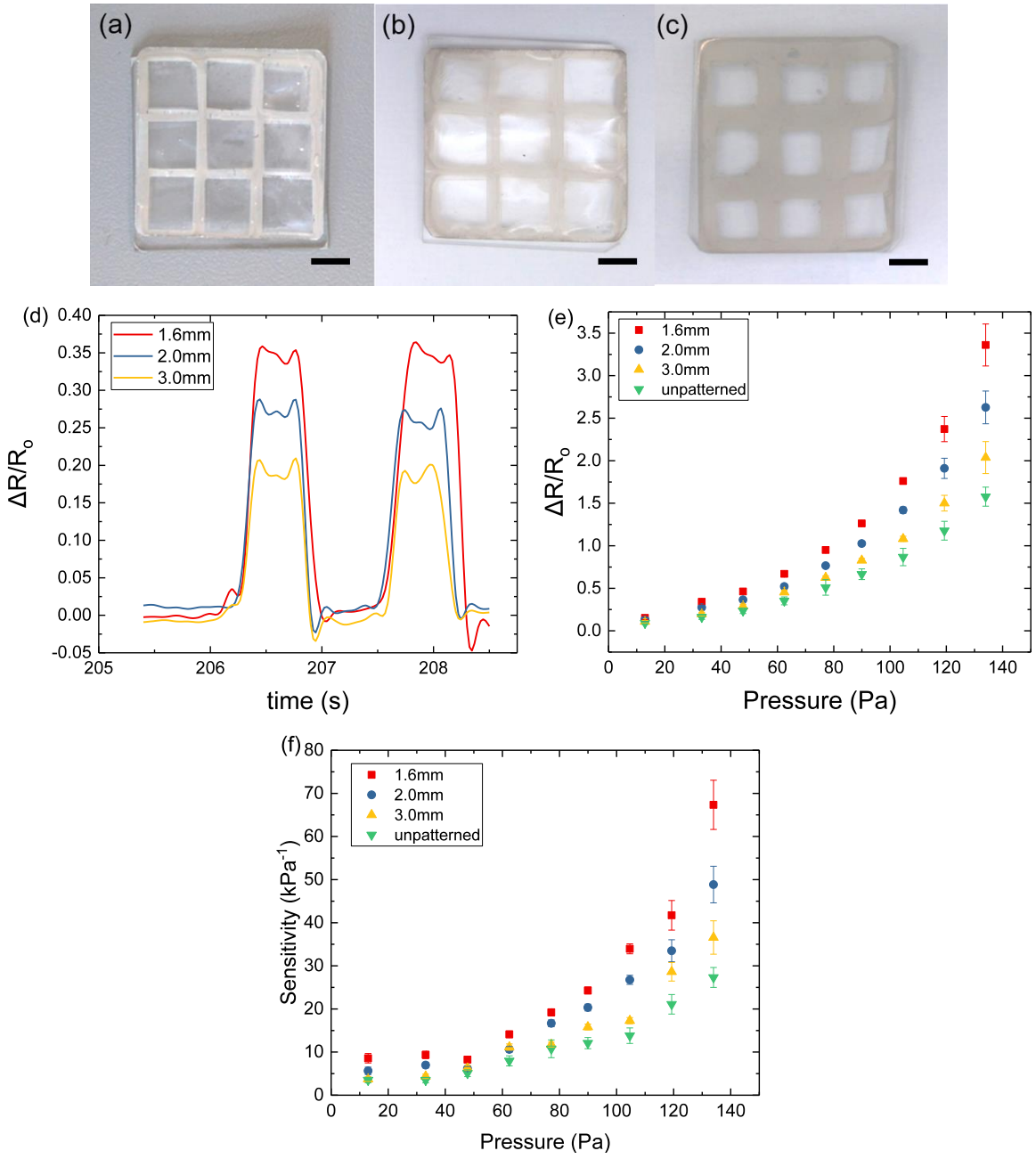



Figure 5-8: Photographs of grid-patterned AgNW-EVA composite films. The grid line widths are approximately: (a) 1.6 mm, (b) 2.0 mm and (c) 3.0 mm. The AgNW concentration of the films are fixed at 0.15 mg/cm$^2$ and the EVA thickness is 35 μm. Scale bar represents 5 mm. (d) The electromechanical response of patterned films with different grid line widths when a pressure of 33.1 Pa is applied on the films. (e) The variation of change in resistance of the films with applied pressure for several patterned films made with different grid line widths. (f) The variation of pressure sensing sensitivities of films with different AgNW loading at different applied pressures.

### 5.3.4 Application in Pulse Sensing

To demonstrate the functionality of the AgNW-EVA composite film as a pressure sensor, it was used as a pulse monitoring device to make use of its flexible and wearable properties. A piece of unpatterned pressure sensing film with AgNW concentration of 0.175 mg/cm$^2$ and EVA thickness of 0.35 μm was attached on the neck of a volunteer to detect the carotid pulse as shown in Figure 5-9a. In this configuration, the AgNW-EVA composite film works in the tensile mode. Therefore, the pressure exerted by the pulse on the film will be detected as an increase in resistance.

Figure 5-9b shows the measured response of the pulse. A clear waveform of the pulse was detected with good repeatability. The frequency of the detected signal matches the typical frequency of a pulse which is slightly above 1 Hz. In addition, the pressure sensor is sufficiently sensitive to detect the two pressure peaks within each pulse, which matches the carotid pulse waveform. The first and higher peak is caused by the forward wave of blood flow created by the contraction of the left ventricle while the second and lower peak is caused by the reflected wave when the blood flow encounters impedance mismatches when flowing into different arteries or capillaries.[35] The detection of these individual peaks is useful as their relative strengths and rhythms can be used to diagnose certain cardiac conditions.

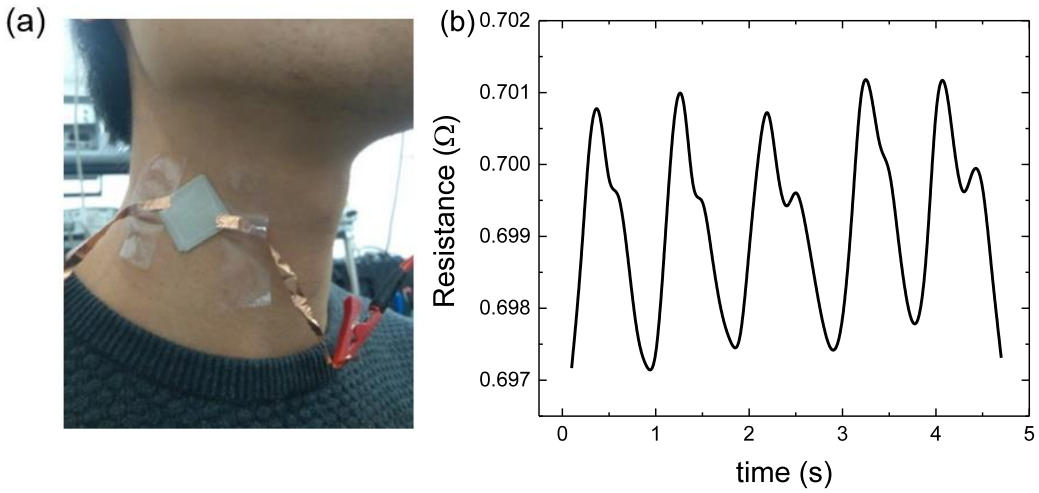



Figure 5-9: (a) Photograph of the setup of pulse monitoring using the AgNW-EVA film. (b) Measured response of carotid pulse.

## 5.4 Conclusion

In conclusion, a simple and cost-effective way to fabricate thin elastic conductive films using silver nanowires as fillers and EVA as the matrix was reported. The films displayed piezoresistivity and could be used as a flexible piezoresistive pressure sensor. The films showed high conductivity which can reduce the power consumption of the final pressure sensing device. Pressure sensing was possible in two configurations, compressive and tensile. This makes the film quite flexible in the ways it can be applied. The performance of the pressure sensors was also highly tunable by adjusting the nanowire and EVA loading in the film. The compressive and tensile modes achieved high sensitivities of 10.2 ± 3.2 $kPa^{-1}$ and 67.3 ± 5.9 $kPa^{-1}$ respectively. Both modes showed a low detection limit of 1.47 Pa for the compressive mode and 12.9 ± 0.37 Pa for the tensile mode. Fast response times of 11-22 ± 2.9 ms were observed in both modes. In general, the tensile mode achieved higher sensitivities as hypothesized. The performance in compressive mode was largely limited by the limited degree of compression possible. By patterning the AgNWs into grids, the sensitivity of the tensile mode sensor was boosted to 67.3 $kPa^{-1}$. The overall performance of these composite films is very competitive with some of the recently reported flexible

pressure sensors in literature as well as commercially available ones. The sensing capabilities of the films were also demonstrated as a pulse monitoring device which worked reasonably well.

## 5.5 References


1. Yu, X. *et al.* Graphene-based smart materials. *Nat. Rev. Mater.* **2**, 1–14 (2017).
2. Zang, Y., Zhang, F., Di, C. A. & Zhu, D. Advances of flexible pressure sensors toward artificial intelligence and health care applications. *Mater. Horizons* **2**, 140–156 (2015).
3. Lang, C., Fang, J., Shao, H., Ding, X. & Lin, T. High-sensitivity acoustic sensors from nanofibre webs. *Nat. Commun.* **7**, 1–7 (2016).
4. Salvatore, G. A. *et al.* Wafer-scale design of lightweight and transparent electronics that wraps around hairs. *Nat. Commun.* **5**, 2982 (2014).
5. Zhang, G. D., Zhao, Y. L., Zhao, Y., Wang, X. C. & Wei, X. Y. Research of a novel ultra-high pressure sensor with high-temperature resistance. *Micromachines* **9**, (2017).
6. Hammock, M. L., Chortos, A., Tee, B. C. K., Tok, J. B. H. & Bao, Z. 25th anniversary article: The evolution of electronic skin (E-Skin): A brief history, design considerations, and recent progress. *Adv. Mater.* **25**, 5997–6038 (2013).
7. Ha, M., Lim, S. & Ko, H. Wearable and flexible sensors for user-interactive health-monitoring devices. *J. Mater. Chem. B* **6**, 4043–4064 (2018).
8. Almassri, A. M. *et al.* Pressure Sensor: State of the Art, Design, and Application for Robotic Hand. *J. Sensors* **2015**, 1–12 (2015).
9. Bangera, A. E. & Kulkarni, S. M. Modeling and Analysis of Pressure Sensor with Single Walled Carbon Nanotubes for Piezoresistive Transduction. *Procedia Mater. Sci.* **5**, 640–647 (2014).
10. Schwartz, G. *et al.* Flexible polymer transistors with high pressure sensitivity for application in electronic skin and health monitoring. *Nat. Commun.* **4**, 1858–1859 (2013).
11. Muthukumar, N., Thilagavathi, G. & Kannaian, T. Polyaniline-coated polyurethane foam for pressure sensor applications. *High Perform. Polym.* **28**, 368–375 (2016).
12. Ko, Y., Kim, D., Kwon, G. & You, J. High-Performance Resistive Pressure Sensor Based on Elastic Composite Hydrogel of Silver Nanowires and Poly(ethylene glycol). *Micromachines* **9**, 438 (2018).
13. George, J. J. & Bhowmick, A. K. Fabrication and properties of ethylene vinyl acetate-carbon nanofiber nanocomposites. *Nanoscale Res. Lett.* **3**, 508–515 (2008).
14. Schneider, C., Langer, R., Loveday, D. & Hair, D. Applications of ethylene vinyl acetate copolymers (EVA) in drug delivery systems. *J. Control. Release* **262**, 284–

295 (2017).

15. Cheng, W. *et al.* A wearable and highly sensitive pressure sensor with ultrathin gold nanowires. *Nat. Commun.* **5**, 1–8 (2014).
16. Zhang, W., Liu, Q. & Chen, P. Flexible Strain Sensor Based on Carbon Black/Silver Nanoparticles Composite for Human Motion Detection. *Materials (Basel).* **11**, 1836 (2018).
17. Lou, C. *et al.* A graphene-based flexible pressure sensor with applications to plantar pressure measurement and gait analysis. *Materials (Basel).* **10**, (2017).
18. Song, Y. *et al.* A highly sensitive flexible strain sensor based on the contact resistance change of carbon nanotube bundles. *Nanotechnology* **27**, (2016).
19. Pan, L. *et al.* An ultra-sensitive resistive pressure sensor based on hollow-sphere microstructure induced elasticity in conducting polymer film. *Nat. Commun.* **5**, 1–8 (2014).
20. Boland, C. S., Khan, U., Benameur, H. & Coleman, J. N. Surface coatings of silver nanowires lead to effective, high conductivity, high-strain, ultrathin sensors. *Nanoscale* **9**, 18507–18515 (2017).
21. Kang, H. S. *et al.* Silver nanowire networks embedded in a cure-controlled optical adhesive film for a transparent and highly conductive electrode. *J. Mater. Chem. C* **4**, 9834–9840 (2016).
22. Liu, W. C. & Watt, A. A. R. Solvodynamic Printing As A High Resolution Printing Method. *Sci. Rep.* **9**, 10766 (2019).
23. Kumar, S. S. & Pant, B. D. Design principles and considerations for the 'ideal' silicon piezoresistive pressure sensor: A focused review. *Microsyst. Technol.* **20**, 1213–1247 (2014).
24. Coskun, S., Aksoy, B. & Unalan, H. E. Polyol synthesis of silver nanowires: An extensive parametric study. *Cryst. Growth Des.* **11**, 4963–4969 (2011).
25. Mutiso, R. M. & Winey, K. I. Electrical properties of polymer nanocomposites containing rod-like nanofillers. *Prog. Polym. Sci.* **40**, 63–84 (2015).
26. Foygel, M., Morris, R. D., Anez, D., French, S. & Sobolev, V. L. Theoretical and computational studies of carbon nanotube composites and suspensions: Electrical and thermal conductivity. *Phys. Rev. B - Condens. Matter Mater. Phys.* **71**, 1–8 (2005).
27. Žeželj, M. & Stanković, I. From percolating to dense random stick networks: Conductivity model investigation. *Phys. Rev. B* **86**, 134202 (2012).

28. Li, J. & Östling, M. Conductivity scaling in supercritical percolation of nanoparticles-not a power law. *Nanoscale* **7**, 3424–3428 (2015).
29. Garboczi, E. J., Snyder, K. A., Douglas, J. F. & Thorpe, M. F. Geometrical percolation threshold of overlapping ellipsoids. *Phys. Rev. E* **52**, 819–828 (1995).
30. Johner, N., Grimaldi, C., Balberg, I. & Ryser, P. Transport exponent in a three-dimensional continuum tunneling-percolation model. *Phys. Rev. B - Condens. Matter Mater. Phys.* **77**, 1–11 (2008).
31. Grimaldi, C. & Balberg, I. Tunneling and nonuniversality in continuum percolation systems. *Phys. Rev. Lett.* **96**, 15–18 (2006).
32. Reuss, A. Berechnung der Fließgrenze von Mischkristallen auf Grund der Plastizitätsbedingung für Einkristalle . *ZAMM - Zeitschrift für Angew. Math. und Mech.* **9**, 49–58 (1929).
33. Wygant, I. O., Kupnik, M. & Khuri-Yakub, B. T. Analytically calculating membrane displacement and the equivalent circuit model of a circular CMUT cell. *Proc. - IEEE Ultrason. Symp.* 2111–2114 (2008). doi:10.1109/ULTSYM.2008.0522
34. Martinez, V. *et al.* Stretchable Silver Nanowire-Elastomer Composite Microelectrodes with Tailored Electrical Properties. *ACS Appl. Mater. Interfaces* **7**, 13467–13475 (2015).
35. Leitão, C. *et al.* Feasibility studies of Bragg probe for noninvasive carotid pulse waveform assessment. *J. Biomed. Opt.* **18**, 017006 (2013).

# Chapter 6 – Conclusion and Future Work

## 6.1 Conclusion of Thesis Findings

This thesis has presented work targeting various aspects of the use and application of non-contact printing techniques in fabricating flexible electronic devices. The focus was primarily on using AgNWs as a conductive nanomaterial for fabricating highly conductive structures for pressure sensing applications.

In Chapter 3, the use of solvent-solvent interactions as a way to minimize the ink footprint dispensed from the nozzle and control the degree of ink spreading on the substrate was explored. The technique which we call "Solvodynamic printing" incorporates an additional carrier solvent that is immiscible with the ink into the ink delivery system. This was an interesting idea to explore as a simple addition made to the printing process could potentially target both factors simultaneously to improve printing resolution. The presence of the carrier solvent within the ink delivery system focused the ink stream into a smaller stream when it exited the nozzle. At the same time, the presence of the carrier solvent around the deposited ink increased the contact angle of the ink which led to improvements in printing resolution.

Using the prototype solvodynamic printer, the proof-of-concept of solvodynamic printing was shown by printing AgNP inks. The effect of several key printing parameters such as the ink stream width, ink surface tension, substrate surface energy and overall ink loading were studied. From the results, a semi-empirical model was developed which could predict the achievable resolution accurately. Using the optimized parameters from the study, silver lines with widths of $35.2 \pm 7.0$ μm were printed from a nozzle with diameter of 300 μm. This resolution is still inferior to that achievable by inkjet printing but it is noted that the results

are still promising given that the printed features are only about 11.7 ± 2.3 % of the nozzle size, which is a sizeable reduction. In addition, the large nozzle size of our printer meant that larger AgNWs could be printed. This is beneficial for printing highly conductive structures.

In Chapter 4, the focus was on improving the electrical conductivity of printed AgNW films. In particular, the aim was to create an AgNW ink that could produce highly conductive features without the need for any post-treatment. Since the conductivity of AgNW films are largely limited by their junction resistances, the strategy of altering the surface ligands on the AgNWs was adopted to improve the resultant junction resistances. More specifically, rigid bidentate ligands were used to link two AgNWs together in closer proximity to improve charge transport across the nanowire junctions in the films.

The ligand exchange process and the structure of the resultant AgNWs were studied using FTIR, TGA and zeta potential measurements. These results were then related to the final film sheet resistances. The results showed that the use of bidentate ligands did improve the overall film conductivities more effectively than monodentate non-linking ligands. The rigid properties in ligands were found to improve the linking effectiveness of the ligands to produce high conductance nanowire junctions and also change the film morphology which contributes to improving the overall conductivity of the printed films. The best results were obtained using fumaric acid as ligands which successfully reduced the AgNW film sheet resistance by approximately 70% from 26.5 to 7.66 Ω/□. The findings in this chapter may also be useful in other solution processable nanomaterials as well.

Chapter 5 made use of the findings from Chapters 3 and 4 to fabricate highly conductive elastic composite films with AgNW fillers embedded in an EVA matrix. The films could be used as piezoresistive pressure sensors. The aim was to achieve a highly conductive and sensitive pressure sensor by making use of pressure-induced tensile strains. A methodology was also chosen such that the sensor can be fully solution-processed using solvodynamic printing.

The electromechanical response of the films to both pressure-induced compressive and tensile strains were studied and compared. The two different modes showed contrasting results. For pressure sensing in the compressive mode, the film achieved a maximum sensitivity of $10.2 \pm 3.2$ $kPa^{-1}$ at low pressures and decreased steadily with increasing pressure. Therefore, a lower detection limit of 1.5 Pa was achieved. On the other hand, the tensile sensing mode showed higher sensitivity at increased pressures. The maximum sensitivity achieved was 54.4 $kPa^{-1}$ with a detection limit of 13 Pa in unpatterned films. For the tensile mode, the sensitivity can be boosted by patterning the AgNW film into grids. As a result, an increased sensitivity of $67.3 \pm 5.9$ $kPa^{-1}$ was achieved. The films also had fast response times of about 11-22 ms. Overall, the film was very easy to fabricate and still showed good performance compared to many reported flexible pressure sensors. The pressure sensing nature of the films were successfully demonstrated in a pulse sensing application as well.

## 6.2 Future Work

Although progress have been made in this thesis, there is still much more to explore in the area of non-contact printing for flexible electronics.

Firstly, the technique of solvodynamic printing is only in its nascent stage and has much room for growth in further improving the achievable printing resolution. The use of microfluidics in solvodynamic printing has much more depth to be explored. Solvodynamic printing should be able to achieve a huge boost in resolution with the use of the droplet formation regime instead of the parallel flow regime. Other applications using microfluidics have been able to generate pico- to femto-litre range droplets.[1,2] If ink droplets of such dimension could be generated by microfluidics technology, printed features on par with EHD printing could potentially be possible. In addition, a deeper understanding in the drying behaviour of the ink and carrier system should be studied. Currently, the printed features seemed to be generally thicker in the middle compared to at the edges due to the carrier solvent tending to accumulate at the sides of the printed features. Perhaps by tuning the combination of carrier solvent and ink solvent, the drying mechanism can be controlled to produce more uniform printed features which would be beneficial for the resultant electronic device.[3] This could be further extended to using an appropriate carrier solvent to control the drying behavior of the ink that may cause resolution improvements by accelerating flows towards the edges or the centre of the printed feature as reviewed in Chapter 2.[4,5]

As for the ligand exchange for AgNWs, additional studies can be done to gain a deeper understanding of the ligand exchange process in terms of its kinetics and mechanism. With this additional knowledge, the effectiveness of ligand exchange reactions can be improved for more effective functionalization of AgNWs. In addition, theoretical studies that can

elucidate the charge transport process at the nanowire junction using density field theory simulations should be done. This will then give us more information about what ligands can form better junctions and further improve the junction resistances. An interesting type of ligands that can also be used are highly conjugated ligands.[6,7] This type of ligands have been used to form molecular junctions between metals and present an additional conduction pathway through electron hopping through the conjugated π-network which may improve charge transport at nanowire junctions. In addition, since electron-hopping is temperature dependent, the resultant films could potentially be used as a temperature sensor.[8–10]

As for the composite film pressure sensors, the next step is to downsize the sensor area so that an array of sensors can be built to move towards a pressure sensor with spatial resolution sensing.[11] In addition, it will also be important to understand how the electromechanical response is affected by temperature for accurate pressure sensing under different environments.[12]

For the compressive mode, several studies can be done to improve the performance of the sensor. A different device configuration of having two of the AgNW-EVA films placed face to face can be used to potentially increase the sensitivity as larger changes in contact resistance would be possible. Another strategy that can be attempted is to make the AgNWs become better dispersed within the entire EVA matrix. This can be done in conjunction with the ligand exchange studies by replacing the hydrophilic ligands with hydrophobic ones.[13,14] With well-dispersed AgNWs throughout the film, the performance of the compression mode pressure sensor using AgNW-EVA composite films could potentially be improved as changes in film resistance can occur over a larger range of compression strains.

For the tensile mode, numerical studies can to be done to relate the applied pressure to the tensile strain experienced by the film. Such studies will involve the application of membrane theory or thin plate theory to understand the mechanical response of films under flexural stress with different conditions depending on the number of fixed corners or edges on the film.[15–17] This information would be important for device design and downsizing sensor size.

## 6.3 References


1. Kaminski, T. S., Scheler, O. & Garstecki, P. Droplet microfluidics for microbiology: Techniques, applications and challenges. *Lab Chip* **16**, 2168–2187 (2016).
2. Leman, M., Abouakil, F., Griffiths, A. D. & Tabeling, P. Droplet-based microfluidics at the femtolitre scale. *Lab Chip* **15**, 753–765 (2015).
3. Mampallil, D. & Eral, H. B. A review on suppression and utilization of the coffee-ring effect. *Adv. Colloid Interface Sci.* **252**, 38–54 (2018).
4. Kuang, M. *et al.* Inkjet Printing Patterned Photonic Crystal Domes for Wide Viewing-Angle Displays by Controlling the Sliding Three Phase Contact Line. *Adv. Opt. Mater.* **2**, 34–38 (2014).
5. Zhang, Z. *et al.* Controlled inkjetting of a conductive pattern of silver nanoparticles based on the coffee-ring effect. *Adv. Mater.* **25**, 6714–6718 (2013).
6. Chen, W. *et al.* Highly conducting π-conjugated molecular junctions covalently bonded to gold electrodes. *J. Am. Chem. Soc.* **133**, 17160–17163 (2011).
7. Chen, W. *et al.* Aromaticity decreases single-molecule junction conductance. *J. Am. Chem. Soc.* **136**, 918–920 (2014).
8. Wuelfing, W. P. & Murray, R. W. Electron hopping through films of arenethiolate monolayer-protected gold clusters. *J. Phys. Chem. B* **106**, 3139–3145 (2002).
9. Jo, H. S. *et al.* Wearable transparent thermal sensors and heaters based on metal-plated fibers and nanowires. *Nanoscale* **10**, 19825–19834 (2018).
10. Gong, S., Zhu, Z. H. & Li, Z. Electron tunnelling and hopping effects on the temperature coefficient of resistance of carbon nanotube/polymer nanocomposites. *Phys. Chem. Chem. Phys.* **19**, 5113–5120 (2017).
11. Li, J., Bao, R., Tao, J., Peng, Y. & Pan, C. Recent progress in flexible pressure sensor arrays: From design to applications. *J. Mater. Chem. C* **6**, 11878–11892 (2018).
12. Yao, Z. *et al.* Passive resistor temperature compensation for a high-temperature piezoresistive pressure sensor. *Sensors (Switzerland)* **16**, (2016).
13. Choi, S. *et al.* Stretchable Heater Using Ligand-Exchanged Silver Nanowire Nanocomposite for Wearable Articular Thermotherapy. *ACS Nano* **9**, 6626–6633 (2015).
14. Jurewicz, I. *et al.* Functionalization of Silver Nanowire Transparent Electrodes with Self-Assembled 2-Dimensional Tectomer Nanosheets. *ACS Appl. Nano Mater.* **1**, 3903–3912 (2018).
15. Srivastava, A. & Hui, C. Y. Large deformation contact mechanics of long rectangular membranes. I. Adhesionless contact. *Proc. R. Soc. A Math. Phys. Eng. Sci.* **469**, (2013).
16. Lee, C. C., Huang, P. C. & Wang, K. S. Flexural capability of patterned transparent conductive substrate by performing electrical measurements and stress simulations. *Materials (Basel).* **9**, (2016).

17. Peng, B., Pugno, N. & Espinosa, H. D. An analysis of the membrane deflection experiment used in the investigation of mechanical properties of freestanding submicron thin films. *Int. J. Solids Struct.* **43**, 3292–3305 (2006).